2007-01-10

Wavelength Conversion Using Reconfigurable Photonic Crystal MEMS/NEMS Structures

Kahraman Daglar Akdemir
Worcester Polytechnic Institute

Wavelength Conversion Using Reconfigurable Photonic Crystal MEMS/NEMS Structures

by

Kahraman Daglar Akdemir

A Thesis
Submitted to the Faculty
of the
WORCESTER POLYTECHNIC INSTITUTE
in partial fulfillment of the requirements for the
Degree of Master of Science
in
Electrical and Computer Engineering
by

Fall 2006

APPROVED:

Professor Brian King, Major Advisor

Professor David Cyganski

Professor Reinhold Ludwig

Abstract

Globally increasing levels of bandwidth and capacity requirements force the optical communications industry to produce new products that are faster, more powerful, and more efficient. In particular, optical-electronic-optical (O-E-O) conversions in Wavelength Division Multiplexing (WDM) mechanisms prevent higher data transfer speeds and create a serious bottleneck for optical communications. These O-E-O transitions are mostly encountered in the Wavelength converters of WDMs, and as a result, all-optical wavelength conversion methods have become extremely important. The main discussion in this thesis will concentrate on a specific all-optical wavelength conversion mechanism. In this mechanism, photonic crystal structures are integrated with moving MEMS/NEMS structures to create a state-of-the-art all-optical wavelength converter prototype. A wavelength conversion of 20% is achieved using this structure.

Since the interaction of light with moving MEMS/NEMS structures plays an important role in the proposed wavelength conversion mechanism, modeling and simulation of electromagnetic waves becomes a very crucial step in the design process. Consequently, a subsection of this thesis will focus on a proposed enhancement to the finite-difference time-domain (FDTD) to model moving structures more efficiently and more realistically. This technique is named "Linear Dielectric Interpolation" and will be applied to more realistically and efficiently model the proposed photonic crystal MEMS/NEMS wavelength conversion mechanism.

Acknowledgements

First, I would like to give my sincerest thanks to my advisor, Prof. Brian King. I learn a lot from you, and not only academically. I will never forget your family's sincerity and hospitality.

Next, I would like to thank Prof. Reinhold Ludwig and Prof. David Cyganski. I am honored that you accepted to review my work and thesis.

Also, I would like to thank my best friends Erdinc Ozturk, Ismail Onur Filiz, Emrah Deniz, Emrah Durulan and Volkan Kurt for always being there for me. I miss you guys, except Erdinc because you are my roommate already :)

I want to thank my family, but I want to do it in my own language: "Annem Aytan Akdemir, babam Mehmet Akdemir, ve canimdan cok sevdigim cadi kardesim Burcu Caglar Akdemir'e her zaman yanimda olduklari ve beni destekledikleri icin tesekkur ederim. Sizleri hep cok ozluyorum. Umarim hayatiniz boyunca hep cok mutlu olursunuz, cunku ben mutlu olmak icin hep sizden guc aliyorum.."

Finally, I would like to thank my best friend for everything.. Tesekkurler guzel gozlu kuzum..

Kahraman Daglar Akdemir [11.12.2006]

Contents

List of Figures

Chapter 1

Introduction

In his famous talk "There's Plenty of Room at the Bottom", Feynman asked the following question: "Why cannot we write the entire 24 volumes of the Encyclopedia Britannica on the head of a pin?". He also discussed the issue of miniaturizing computers and asked "Why can't we make them very small?" While answering these questions back in 1959, he formed the basis and roots of nanotechnology which he imagined would be manipulating and controlling things on a small scale [18]. Similarly, in his paper "Cramming more components onto integrated circuits", Moore predicted that number of transistors on an integrated circuit (IC) would double every 18 months. In this paper, which was written back in 1965, he said that "Integrated electronics will make electronic techniques more generally available throughout all of society, performing many functions that presently are done inadequately by other techniques or not done at all." [40]

When we look at the advancements in nanotechnology today, we should agree that Feynman and Moore made very precise predications almost fourty years ago. Every year, the overall interest in nanotechnology research and development is increasing rapidly. Consequently, various types of nanotechnological applications are being produced in various fields. Some of these applications are prototypes existing in present research and will need more time to become commercially available. An important portion of these products, on the other hand, have already become commercially available and are being used in various applications.

First of all, the most important implication of nanotechnology is observed in the electronic IC domain. Electronic IC technology and fabrication methods associated with it have been the driving force and the locomotive of nanotechnology. The advancements in fabrication technology (clean rooms, various fabrications methods, and complicated machines capable to implement these methods) increased the rate of development in manipulation and control on very small scales. This in turn provided more reliable, more efficient, faster, and cheaper components in the electronics domain. Minimum feature sizes less than 50 nm are becoming more common for the transistors used in ICs. Very efficient and powerful microprocessors (even with multicore and multithreading technologies to increase the parallelism in instruction execution) have been developed. Also, memories with very high data storage capacity and very low latencies have been produced. This miniaturization and performance increase in IC technology also enables the miniaturization of very popular products such as cellular phones, laptop computers, mp3 players, camcorders, digital cameras, etc.

Another area in which the nanotechnology creates the basis for is transducers. Transducers are the mechanisms which convert one type of energy to another. Using Micro/Nano-Electro-Mechanical-Systems (MEMS/NEMS), which are maturing rapidly as a result of the available IC fabrication technology, various types of novel transducers are produced. Very briefly, MEMS/NEMS is the technology used to create moving parts in micro/nano scale. They can be used either to sense specific characteristics in the environment or to manipulate (and respond to) the specific parts of the environment using actuation and motion.

There are two main classes of the transducers: 1) sensors and 2) actuators. Today, various types of sensors, which are used to observe and analyze different characteristics in the environment, are commercially available in industry. Maybe the most common commercial entity that utilizes these sensors is the cars. Pressure sensors for measuring the tire pressure, accelerometers for activating the air bags, chemical sensors for measuring and adjusting the exhaust gas ratios for environmental purposes are just a few examples of the wide variety of sensors found in today's cars. The gyroscopes used in air navigation and game console joysticks are other examples of MEMS/NEMS sensors. A second class of transducers is the actuators which are used to manipulate the surrounding environment. Maybe the most popular and commercially available product in this category is the optical MEMS/NEMS

micromirror arrays used in today's projectors. Microengines, micromotors, gear trains in micron sizes are some of the other examples. One important nanotechnological area, which is enabled as a result of the advancement in MEMS/NEMS technology, is medicine. Lab-on-a-chip devices for diagnostic purposes and complicated drug-delivery systems on the order of biological molecules and structures provide very efficient and good results.

Nanophotonics (optics in nanoscale) is another domain which is a direct beneficiary of nanotechnology. Being able to manipulate light at the chip level can lead to very revolutionary results and applications. Consequently, one can find very interesting nanophotonics research topics in the literature. Photonic crystals are the first example of popular nanophotonic structures. When handled appropriately, these structures can lead to various applications such as on-chip bending waveguides, microcavity lasers, wavelength converters, etc. Another very interesting topic is slowing light for optical storage. If the amplitude and phase information associated with an input beam could be stored, optical memories that can be used in optical computing could be built. Another possible application of nanophotonics is quantum computing which provides very fast and parallel instruction execution on the atomic level using the laws of quantum physics.

The nanotechnological advancements inevitably affected the optical communications domain too. In recent years, by means of the Wavelength Division Multiplexing (WDM) and erbium-doped-fiber-amplifiers (EDFAs), optical communication technology gained a lot of importance. In these systems, the data is encoded using amplitude modulation, and is carried over different channels with different optical carrier frequencies. Optical crossconnect stations in WDM systems connect the data coming from a specific source to a specific destination using wavelength converters. Modern optical communication systems can transfer up to 160 separate signals simultaneously, each of which can provide a data rate of 10 Gbit/s. Consequently, theoretical total capacity of a single fiber is 1.6 Tbit/s. However, optical-electronic-optical(O-E-O) transitions in the optical crossconnects of WDM mechanisms put a severe limit on the optical communication data rates and creates a serious bottleneck. Wavelength converter segments of WDMs suffer the most from these O-E-O transitions and as a result all-optical wavelength conversion methods have become exteremely important.

Ultimately, the main discussion in this thesis will concentrate on a specific all-optical

wavelength conversion mechanism. In this mechanism, photonic crystal structures are integrated with moving MEMS/NEMS structures to create a state-of-the-art all-optical wavelength converter prototype.

Since the interaction of light with moving MEMS/NEMS structures plays an important role in the proposed wavelength conversion mechanism, modeling and simulation of electromagnetic waves becomes a very crucial step in the design process. One of the most popular and powerful simulation mechanisms to model electromagnetic waves is the finite-difference time-domain (FDTD) method. In FDTD, Maxwell's equations are numerically solved in time domain by discretizing time and space. Even though the FDTD technique is a very powerful method, it has some serious limitations when the simulated structure includes motion. Consequently, a subsection of this thesis will focus on a proposed enhancement to the FDTD to model moving structures more efficiently and more realistically. This technique is named "Linear Dielectric Interpolation" and will be applied to more realistically and efficiently model the proposed photonic crystal MEMS/NEMS wavelength conversion mechanism.

Chapter 2

Linear Dielectric Interpolation Method for FDTD

With the increasing interest and advancements in the nanophotonics domain, applications which manipulate light in the micro/nano scale have become very popular in both industry and academia. Before these analytically designed devices are fabricated though, they need to be simulated and modeled using computers to reduce the cost of development.

Finite-difference time-domain (FDTD) is one of the most popular and powerful simulation methods that models these types of nanophotonics structures very accurately. However, when the modeled structure includes the interaction of light with moving nanoscale structures, the FDTD simulations suffer from the generation of non-physical and spurious frequency content. Consequently, in this section of this thesis, an enhancement to the regular FDTD will be proposed. First of all, a brief description of FDTD and its applications will be provided. Next, the efficiency and accuracy of FDTD to model motion will be analyzed. In the third part of this section, the proposed "Linear Dielectric Interpolation Method" will be described in detail. Finally, in the last part of this section, the results and test case performance associated with this method will be presented.

2.1 Brief Description and Applications of FDTD

The interaction of electric and magnetic fields with arbitrary and complex structures can not be solved analytically except for the simplest of cases. In order to solve the general case, numerical methods must be employed. The realm of computational electrodynamics focuses on solving problems of this type. One of the most flexible and powerful numerical solvers is the finite-difference time-domain (FDTD) technique first suggested by Yee in 1966 [75]. By sampling the unknown electric and magnetic field on a spatial grid and then approximating a direct time-domain solution of the differential form of Maxwell's equations, FDTD is able to accurately solve for the unknown field quantities. Similarly, the time derivatives can be approximated by sampling in time, producing the spatial and temporal field distributions of arbitrary structures.

The computational rules for FDTD can be easily described. Basically, Maxwell's equations are discretized and represented using central difference equations in FDTD. As can be observed in the following differential form of Maxwell's equations (assuming that there are no electric or magnetic current sources in the domain, but there may be lossy materials), the behavior of electric field (E) in time depends on the change of the magnetic field (H) across space. This phenomenon leads to the basic FDTD time stepping mechanism which states that the new value of the electric field at any point in space depends on 1) the previous electric field value at that point (temporal) and 2) magnetic field values at the neighboring points of that point (spatial). Similarly, the magnetic field in time depends on the change of the electric field across space, and new value of the magnetic field at any point in space depends on 1) the previous magnetic field value at that point (temporal) and 2) electric field values at the neighboring points of that point (spatial). When this idea is iterated in time, the basic FDTD scheme emerges. Ultimately, at each time step the field quantities at all spatial grid points are updated using only the neighboring field values in space and time.

$$\nabla \cdot D(\overrightarrow{r}, t) = \rho(\overrightarrow{r}) \tag{2.1}$$

$$\nabla \cdot B(\overrightarrow{r}, t) = 0 \tag{2.2}$$

$$\nabla \times E(\overrightarrow{r},t) = -\frac{\partial B(\overrightarrow{r},t)}{\partial t} - M(\overrightarrow{r}) \quad (2.3)$$

$$\nabla \times H(\overrightarrow{r},t) = \frac{\partial D(\overrightarrow{r},t)}{\partial t} + J(\overrightarrow{r}) \quad (2.4)$$

The FDTD algorithm can be applied in 1D, 2D, and 3D using the same idea explained previously. In many dimensions, calculating the curl operation indicated in above Maxwell's equations may become very complicated. However, Yee suggested a lattice structure in which electric and magnetic field values in discrete space are positioned with a half grid distance between them [75]. This is called a Yee lattice, and in this mechanism each electric field component in the space is positioned between two magnetic field components, and vice versa. The Yee lattice in a cubic form for 3D case is indicated in Fig. 2.1. The i, j, and k variable indicated in the figure are the index values of the discretized space in x, y, and z directions, respectively. This lattice structure has become a very crucial part of most FDTD simulations and provides very good results.

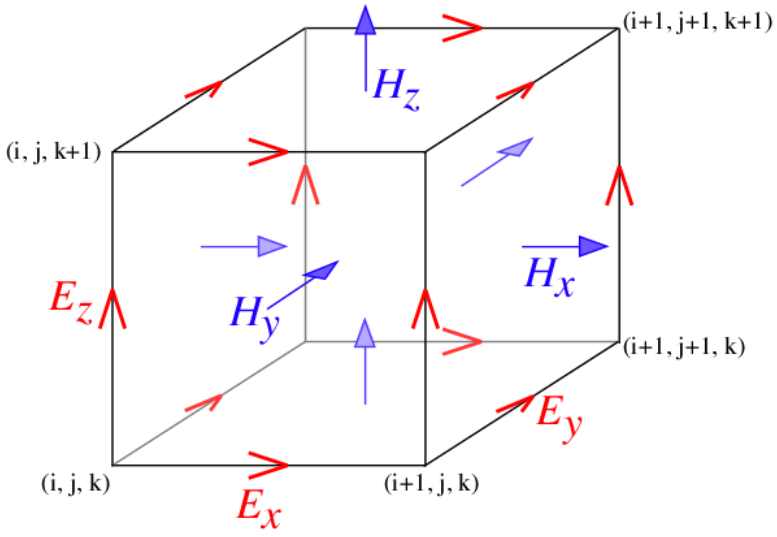

Figure 2.1: Illustration of a standard Yee lattice used for FDTD, in which different field components use different locations in a grid. Visualized as a cubic voxel, the electric field components correspond to the edges of the cube, and the magnetic field components to the faces [71].

The material properties which are included in Maxwell's equations are also used in FDTD simulations. In the computational domain of FDTD simulations, the geometry of the structure and material properties are defined by setting the values for permeability,

permitivity, and conductivity at each grid point of the discretized space. These predefined coupling constants between the grid points effectively encode the local material properties (e.g., the complex-valued material dielectric constant). In addition, boundary conditions such as the tangential electric and magnetic fields at a material interface can be directly enforced.

When these procedures are applied to the Maxwell's equations, we produce the following FDTD approximations for the electric and magnetic fields [65]. Equations 2.5 through 2.7 are for the 2D transverse magnetic (TM) polarized case. Consequently calculations are necessary for only E_z, H_x and H_y are shown in these equations. The i and j parameters are the index values associated with the cubic Yee lattice which is indicated in Fig. 2.1, but in this case just a 2D cross sectional slice of it is used (imagine taking a 2D slice of the 3D Yee lattice shown in this figure, and this slice will only include the H_x, H_y, and E_z field components). n is the time step for the FDTD simulation. The material properties in the computational domain are implemented in the simulation using the C_a, C_b, D_a, and D_b coefficients which are indicated in equations 2.8 to 2.11. As can be observed in these equations, these coefficients are functions of the permitivity, permeability, and the conductance of the discretized space. FDTD estimation equations for 1D fields and coefficients are also indicated in equations 2.12 to 2.17. In all of these equations, the subscripts indicate the coordinates in the discretized space map, and the superscripts represent the time step value in the discretized time. More information and details of this notation can be found in [65].

$$\begin{aligned} E_z\,|^{n+1/2}_{i-1/2,j+1/2} \;=\; & C_{a,E_z}\,|_{i-1/2,j+1/2}\; E_z\,|^{n-1/2}_{i-1/2,j+1/2} + \\ & + C_{b,E_z}\,|_{i-1/2,j+1/2} \cdot \Big(H_y\,|^{n}_{i,j+1/2} - H_y\,|^{n}_{i-1,j+1/2} \Big) + \\ & + C_{b,E_z}\,|_{i-1/2,j+1/2} \cdot \Big(H_x\,|^{n}_{i-1/2,j} - H_x\,|^{n}_{i-1/2,j+1} \Big) \end{aligned} \tag{2.5}$$

$$\begin{aligned} H_x\,|^{n+1}_{i-1/2,j+1} \;=\; & D_{a,H_x}\,|_{i-1/2,j+1/2}\; H_x\,|^{n}_{i-1/2,j+1} + \\ & + D_{b,H_x}\,|_{i-1/2,j+1} \cdot \Big(E_z\,|^{n+1/2}_{i-1/2,j+1/2} - E_z\,|^{n+1/2}_{i-1/2,j+3/2} \Big) \end{aligned} \tag{2.6}$$

$$H_y\mid_{i,j+1/2}^{n+1} = D_{a,H_y}\mid_{i,j+1/2} H_y\mid_{i,j+1/2}^{n} + \\ +D_{b,H_y}\mid_{i,j+1/2}\cdot\left(E_z\mid_{i+1/2,j+1/2}^{n+1/2} - E_z\mid_{i-1/2,j+1/2}^{n+1/2}\right) \tag{2.7}$$

where

$$C_a\mid_{i,j} = \frac{\left(1-\frac{\sigma_{i,j}\Delta t}{2\epsilon_{i,j}}\right)}{\left(1+\frac{\sigma_{i,j}\Delta t}{2\epsilon_{i,j}}\right)} \tag{2.8}$$

$$C_b\mid_{i,j} = \frac{\left(\frac{\Delta t}{\epsilon_{i,j}\Delta space}\right)}{\left(1+\frac{\sigma_{i,j}\Delta t}{2\epsilon_{i,j}}\right)} \tag{2.9}$$

$$D_a\mid_{i,j} = \frac{\left(1-\frac{\sigma^*_{i,j}\Delta t}{2\mu_{i,j}}\right)}{\left(1+\frac{\sigma^*_{i,j}\Delta t}{2\mu_{i,j}}\right)} \tag{2.10}$$

$$D_b\mid_{i,j} = \frac{\left(\frac{\Delta t}{\mu_{i,j}\Delta space}\right)}{\left(1-\frac{\sigma^*_{i,j}\Delta t}{2\mu_{i,j}}\right)} \tag{2.11}$$

$$E_z\mid_{i-1/2}^{n+1/2} = C_{a,E_z}\mid_{i-1/2} E_z\mid_{i-1/2}^{n-1/2} + \\ +C_{b,E_z}\mid_{i-1/2}\cdot\left(H_y\mid_{i}^{n} - H_y\mid_{i-1}^{n}\right) \tag{2.12}$$

$$H_y\mid_{i}^{n+1} = D_{a,H_y}\mid_{i} H_y\mid_{i}^{n} + \\ +D_{b,H_y}\mid_{i}\cdot\left(E_z\mid_{i+1/2}^{n+1/2} - E_z\mid_{i-1/2}^{n+1/2}\right) \tag{2.13}$$

$$C_a\mid_{i} = \frac{\left(1-\frac{\sigma_i\Delta t}{2\epsilon_i}\right)}{\left(1+\frac{\sigma_i\Delta t}{2\epsilon_i}\right)} \tag{2.14}$$

$$C_b\mid_{i} = \frac{\left(\frac{\Delta t}{\epsilon_i\Delta space}\right)}{\left(1+\frac{\sigma_i\Delta t}{2\epsilon_i}\right)} \tag{2.15}$$

$$D_a \mid_i = \frac{\left(1 - \frac{\sigma_i^* \Delta t}{2\mu_i}\right)}{\left(1 + \frac{\sigma_i^* \Delta t}{2\mu_i}\right)} \tag{2.16}$$

$$D_b \mid_i = \frac{\left(\frac{\Delta t}{\mu_i \Delta space}\right)}{\left(1 - \frac{\sigma_i^* \Delta t}{2\mu_i}\right)} \tag{2.17}$$

Boundary conditions due to the edge of the computational grid are solved in a number of ways. Absorbing boundary conditions (ABCs) are used to allow propagating energy to exit the computational cell without causing a spurious reflection that would degrade the quality of the simulation [42]. In 1994, Berenger developed the perfectly-matched-layer (PML) boundary condition that effectively made the computational boundary appear as a perfectly-matched medium for plane waves of arbitrary frequency, direction, and polarization [6]. Regardless of the shape and spectrum of a propagating waveform, it would be absorbed with potentially a negligible (-80 dB) reflection. PML provides orders of magnitude lower reflections at the boundaries of the computational domain when compared to other ABCs.

As all modeling techniques, FDTD has its advantages and limitations too. The first strength of the FDTD method is that it is very easy to understand and implement in software. Also, because it is a time domain solver, response of the system to many different frequencies can be simulated in a single run. In addition, maybe the biggest advantage of this method is its flexibility in creating various structures in the computational domain. As mentioned before, this can be done by assigning specific values for material properties in each cell of the main FDTD lattice. Finally, in this technique the electric and magnetic fields are computed directly so there is no need for any type of post processing to get the field values.

Next, we mention some the weaknesses of the FDTD. The first disadvantage of this mechanism is the spatial discretization. The spatial discretization of the structure must be sufficient enough for correct and precise simulations. This in turn may lead to very large computational domains and very long simulation times. Another disadvantage of this method is that the far field extensions are hard to implement. In other words, the field values at some distance are hard to find without any post-processing of the resulting simulation data. Finally, the most relevant disadvantage of the FDTD technique to this

thesis is its failure to correctly model moving structures and motion. Because time and space are discretized, the continuous nature of the motion in moving structures cannot be accurately represented in this method. Consequently, when the interaction between moving structures and electromagnetic waves is modeled using this technique, non-physical and artificial results may be observed.

Another important issue that needs to be discussed concerning the FDTD method is the algorithm's stability. Since the FDTD works on a discrete domain and approximates Maxwell's equations by discretizing time and space, a typically negligible amount of approximation error occurs in the simulations. If a certain relation between the time and space steps of the simulations is not met, this negligible error can grow exponentially causing instabilities and unexpected results. This relation is indicated in the following equation and is known as the Courant stability criterion. In this equation, c_{max} is the maximum wave speed in the solution space, Δt is time step, and $\Delta x, \Delta y$, Δz are the space discretizations. A more detailed analysis of the derivation of this relation is provided in [64].

$$c_{max} \times \Delta t \leq \left[\frac{1}{(\Delta x)^2} + \frac{1}{(\Delta y)^2} + \frac{1}{(\Delta z)^2}\right]^{-1/2} \tag{2.18}$$

In addition to the stability issue, numerical dispersion in FDTD simulations also needs to be addressed to get accurate results. Modeling and simulating Maxwell's time-dependent curl equations using FDTD causes numerical dispersion in the simulations. Basically, depending on the modal wavelength, propagation direction, and lattice discretization, the phase velocity of the numerical modes in the main FDTD lattice can vary. This leads to nonphysical artifacts such as pulse distortion, artificial anisotropy, and pseudorefraction in the simulations [63]. To solve this issue, the space discretizations, $\Delta x, \Delta y$, and Δz, must be a small fraction (a common rule of thumb is $\frac{1}{10}$) of either the minimum wavelength or minimum feature size in the model [58, 33, 41].

FDTD has been successfully applied to a wide variety of applications. For example, it has been used extensively in military contexts such as ground-penetrating radar, land mine detection, radar guidance, and electromagnetic pulse shielding [59, 60]. Commercial companies use FDTD to improve and test antenna designs, and determine the effect of parasitic capacitances on high-speed circuit boards. It is also used extensively in the optical

community to design high-frequency optical communication devices, optical filters, and optical switches. Academic research groups are also actively using FDTD techniques to investigate novel nanoscale optical devices.

2.2 FDTD and Moving Structures

Finite-difference time-domain (FDTD) simulations can fail to accurately model the Doppler shift associated with moving structures. In this section, we propose a simple linear interpolation method that significantly improves the accuracy of the simulation. This improvement is necessary for precise design of optical MEMS/NEMS structures.

Modeling and simulation demands high accuracy at reasonable computational complexity and plays an important role in the design process of optical MEMS/NEMS structures. When the modeled structure is static, material properties in the FDTD calculation grid are constant, and electric/magnetic fields in the structure are approximated very precisely. However, when there are continuously moving structures in the FDTD model (which is the case for optical MEMS/NEMS devices), the material properties in the FDTD calculation grid change continuously as the MEMS/NEMS structures move and the coefficients have to be updated. However, since the time and space are discretized in FDTD solutions, the full continuous nature of the movement cannot be accurately reflected in the calculation of the parameters. This results in instantaneous "pseudo" jumps in material properties. Ultimately, non-physical spurious frequency content is generated which leads to erroneous results.

Because modeling is a very crucial step for the realization of optical MEMS/NEMS components, different ways to efficiently and accurately incorporate moving structures into FDTD have been proposed in the literature. First of these methods is the quasi-stationary method in which the main idea is to update the changing material coefficients in the FDTD simulation at the end of each time step [7]. However, time and space in FDTD simulations are discretized. Consequently, even though this technique provides an approximate answer for some cases, it cannot model the continuous nature of the motion accurately and cannot provide the proper physics behind the motion-electromagnetic wave interaction.

A second possible method to more accurately model motion in FDTD simulations is the system transformation method that mainly consists of transformations between moving and stationary frames of reference [47]. Basically, the incident field in the stationary domain is transformed to the moving system domain using a Lorentz transformation. In this system frame, the moving layer is stationary and it becomes much more easier to define and solve the electromagnetic boundary conditions. The disadvantage associated with this method is the extra effort spent for transitions (transformations) between the two domains in the simulation.

A third possible method is the application of relativistic boundary conditions. In this method, the relativistic boundary conditions between the moving structure and the stationary domain surrounding it (at the surface of the moving structure) are incorporated into the FDTD simulations. If the relativistic boundary condition is applied only for the electric field in each time step, then this method is referred to as semi-relativistic boundary condition. If on the other hand the relativistic boundary conditions is applied for both electric and magnetic fields, then this method is referred to as fully-relativistic boundary condition. More information and analytical details about relativistic boundary conditions can be found in [24, 14].

Another method that is proposed to model reconfigurable MEMS/NEMS structures in optical and RF domains is variable gridding [11]. In this method, the grid structure of the main FDTD window can be different in different parts of the simulated structure. For example, at the parts of the structure where there is motion, an increased resolution can be used while at the stationary parts (where the resolution is not a very important factor for accuracy), a lower resolution in space can be implemented. This way the increase in the simulation time due to the increased resolution is kept at minimum. In this method, providing the correct interaction between different cells with different space discretization may be a complicated task. In addition, if the motion in the FDTD domain sweeps a big portion of the main grid, then using this method will be very computationally inefficient. Also, it becomes very difficult to implement arbitrary motion trajectories in this method.

These are some of the most popular methods that are used in the literature to more accurately simulate moving structures in FDTD. In the following subsection we propose another

method, "Linear Dielectric Interpolation", to incorporate the motion of MEMS/NEMS structures into the FDTD simulations in a very efficient and simple way. A conceptually similar study has been conducted by Inman [28], but we propose a more complete method and provide insight into the capabilities, limitations, and efficiency of this approach.

At this point, it is also important to note the stability issues caused by incorporating movement into the FDTD simulations. As mentioned previously, FDTD has already some limitations in terms of stability. In addition, instantaneous "pseudo" jumps in material properties as a result of moving objects in the main FDTD domain can easily lead to stability problems. In other words, with the motion included in the simulations, FDTD becomes more sensitive to the stability issues. The proposed Linear Dielectric Interpolation method significantly improves the stability limitation. The details of this issue are discussed in section 2.4.

2.3 Linear Dielectric Interpolation Method

As mentioned previously, FDTD cannot accurately model the interaction between electromagnetic waves and moving structures due to its discrete nature in space. One possible solution to this problem is to decrease the spatial grid size used in FDTD calculations so that the discretization error is reduced. However, this solution dramatically increases simulation time because the number of spatial grids to represent the same physical distance increases. Consequently, the number of FDTD calculations increases which makes the simulations longer. This negative side effect can be observed in 1D FDTD simulations in which simulation time and number of space grids are inversely and linearly proportional. The situation becomes much more dramatic when the FDTD is implemented in 2D and 3D because in these cases simulation time and number of space grids are still inversely proportional but the relation becomes quadratic. Ultimately, it can be asserted that this solution is not an efficient and effective one to solve this problem.

We propose the linear interpolation method which is a very efficient and easy method to remove these side effects without significantly increasing the simulation time. Basically, linear interpolation eliminates non-physical discrete jumps in material properties at the

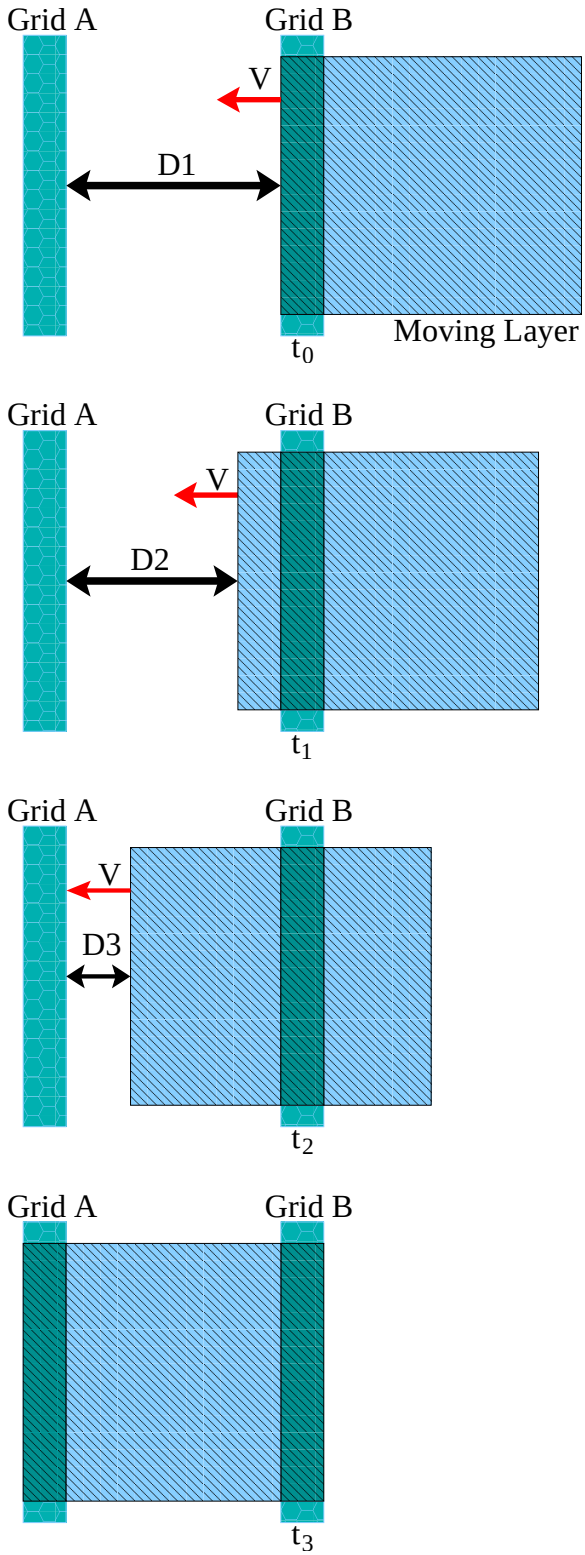

Figure 2.2: Timeline for the interpolation scheme. Two FDTD grids "Grid A" and "Grid B" are indicated at four different times t_0, t_1, t_2, and t_3 respectively. The position of the moving layer is also indicated at each time. Initially, "Grid B" has the dielectric value of the moving structure and "Grid A" represents air, for which dielectric value is one.

boundaries of moving structures by linearly changing their dielectric values. The interpolated dielectric values at the moving interface are calculated using the real continuous position of the moving structure as indicated in Fig. 2.2 and following equations. In Fig. 2.2 two FDTD grids "Grid A" and "Grid B" are indicated at four different times t_0, t_1, t_2, and t_3 respectively. The position of the moving layer is also indicated in this figure at each time. Initially, "Grid B" has the dielectric value of the moving structure and "Grid A" represents air, for which dielectric value is one.

Without interpolation, the continuous nature of the motion indicated in this figure cannot be represented accurately because the dielectric value in "Grid A" is updated to its new dielectric value at time t_3 when the moving layer actually reaches to that grid. However, this update occurs very sharply at a single time step and consequently the dielectric value of "Grid A" (ϵ_a) reaches to the dielectric value of "Grid B" (ϵ_b) at an instant. As a result, the previously mentioned non-physical frequency components occur in the simulation. If this instantaneous jump in the material properties is too large, it may even lead to stability problems in the simulation.

On the other hand, when the linear interpolation method is applied, the dielectric value of "Grid A" is updated at each time using the equations indicated below. When this single equation is applied at each time step using the distance values indicated in Fig. 2.2, the dielectric value of "Grid A" shows a linear increase from its initial value to its final value. Initially at time t_0, the distance between the moving layer and "Grid A" is one grid, which makes ϵ_a=ϵ_a using the first equation. At time t_1, the moving layer is between the two grids but close to the "Grid B". Consequently, for "Grid A" second equation leads to a dielectric value which is between the original ϵ_a and ϵ_b but much closer to ϵ_a. At time t_2, this situation is reversed so the dielectric value of "Grid A" becomes much closer to the dielectic value of the moving structure which is represented by ϵ_b. Finally, when the moving layer actually reaches to "Grid A" position, the dielectric value in this grid becomes equal to the dielectric value of the moving layer which is indicated in the equation for t_3. In this case, the continuous nature of the motion is modeled more accurately and this solves the previously mentioned stability and non-physical frequency generation problems.

$$At \quad t_0 \quad \rightarrow \quad \epsilon_b \quad = \quad D_1 \times \epsilon_a + (1 - D_1) \times \epsilon_b = \epsilon_a \tag{2.19}$$

$$At \quad t_1 \quad \rightarrow \quad \epsilon_b \quad = \quad D_2 \times \epsilon_a + (1 - D_2) \times \epsilon_b \tag{2.20}$$

$$At \quad t_2 \quad \rightarrow \quad \epsilon_b \quad = \quad D_3 \times \epsilon_a + (1 - D_3) \times \epsilon_b \tag{2.21}$$

$$At \quad t_3 \quad \rightarrow \quad \epsilon_a \quad = \quad \epsilon_b \tag{2.22}$$

Fig. 2.3 and Fig. 2.4 show the dielectric values of "Grid A" and "Grid B" for the cases indicated in Fig. 2.2. Fig. 2.3 provides the results associated with the simulation in which the suggested linear interpolation method is not used, and Fig. 2.4 gives the results for the same simulation but this time the linear interpolation mechanism is applied. Both figures include four different time steps each of which correspond to the time steps of Fig. 2.2. In both cases, the edge of the moving layer is between space grids 3 and 4. At time t_0 the moving layer is on space grid 4, which represents the "Grid B", and it will move towards the space grid 3, which represents the "Grid A" in Fig. 2.2.

As can be observed in Fig. 2.3, the dielectric constant of space grid 3 ("Grid A") is initially ϵ_a=1, which is the dielectric constant of air. At times t_1 and t_2, even though the moving layer gets closer to the space grid 3 ("Grid A") as a result of its continuous motion, the dielectric value at this grid is not updated and remains the same. In the last time step t_4 when the moving layer actually reaches to the space grid 3 ("Grid A"), the dielectric constant value of this grid is updated to the dielectric constant value of the moving layer ϵ_b=5.3. This is an instantaneous jump in the dielectric value of "Grid A". In the FDTD simulation of this case, there is air in space grid 3 ("Grid A") in time steps t_0, t_1, and t_2 and the previously mentioned FDTD field calculations are done using the material properties associated with air. However, in just one time step, the space grid 3 ("Grid A") becomes the moving layer and all its material characteristics are converted to the material properties associated with the moving layer material. Then the new FDTD field calculations are done using these new values, and this situation causes the previously mentioned accuracy and stability problems in FDTD simulations.

On the other hand, when the linear interpolation method is applied, the continuous nature of the motion is modeled more accurately as can be observed in Fig. 2.4. Initially,

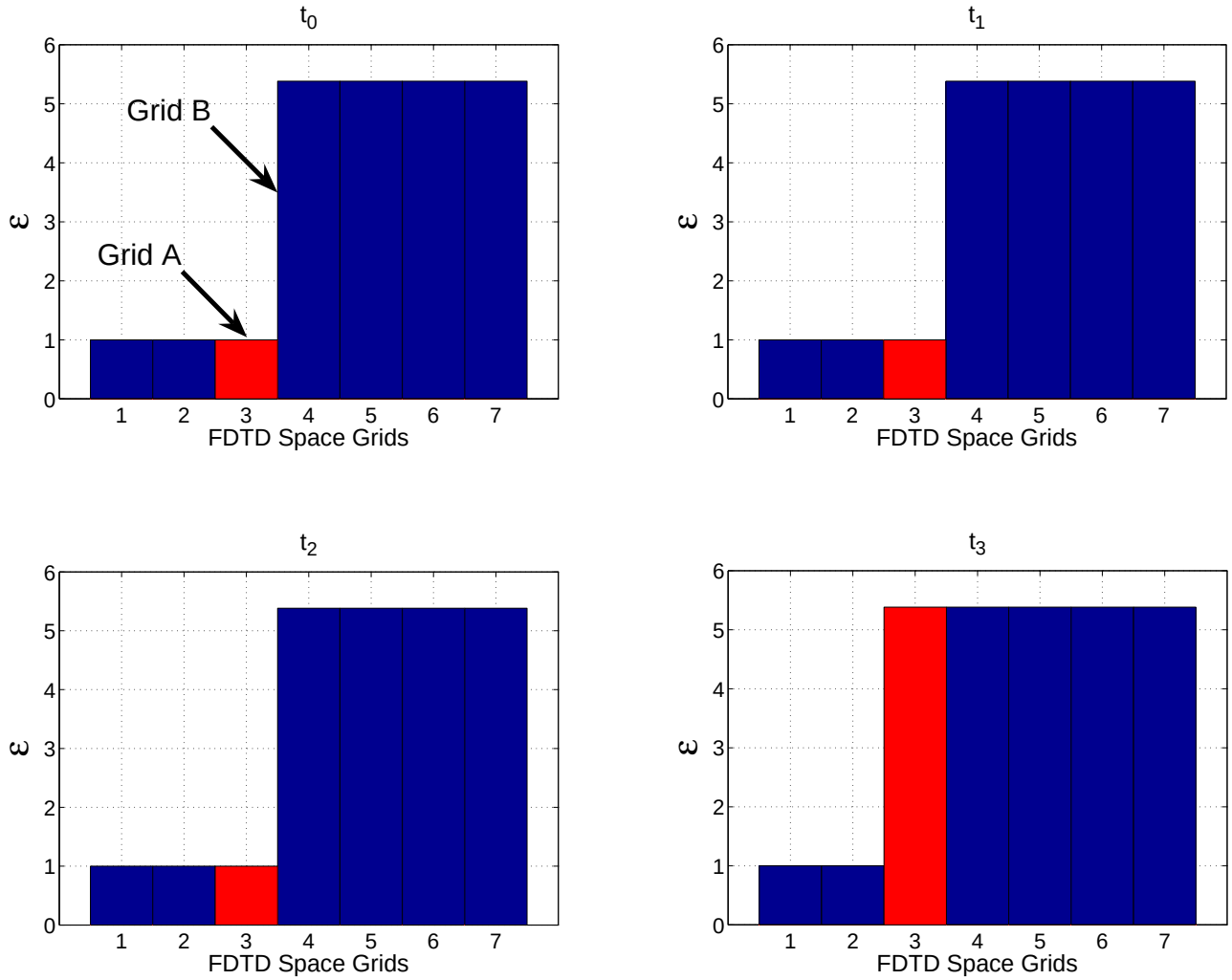

Figure 2.3: The dielectric constant of space grid 3 ("Grid A") is indicated in four different time steps. Initially at time t_0, ϵ_a=1 which is the dielectric constant of air. At times t_1 and t_2, even though the moving layer gets closer to the space grid 3 ("Grid A") as a result of its continuous motion, the dielectric value at this grid is not updated and remains the same. At time t_4 when the moving layer actually reaches to the space grid 3 ("Grid A"), the dielectric constant value of this grid is updated to the dielectric constant value of the moving layer ϵ_b=5.3.

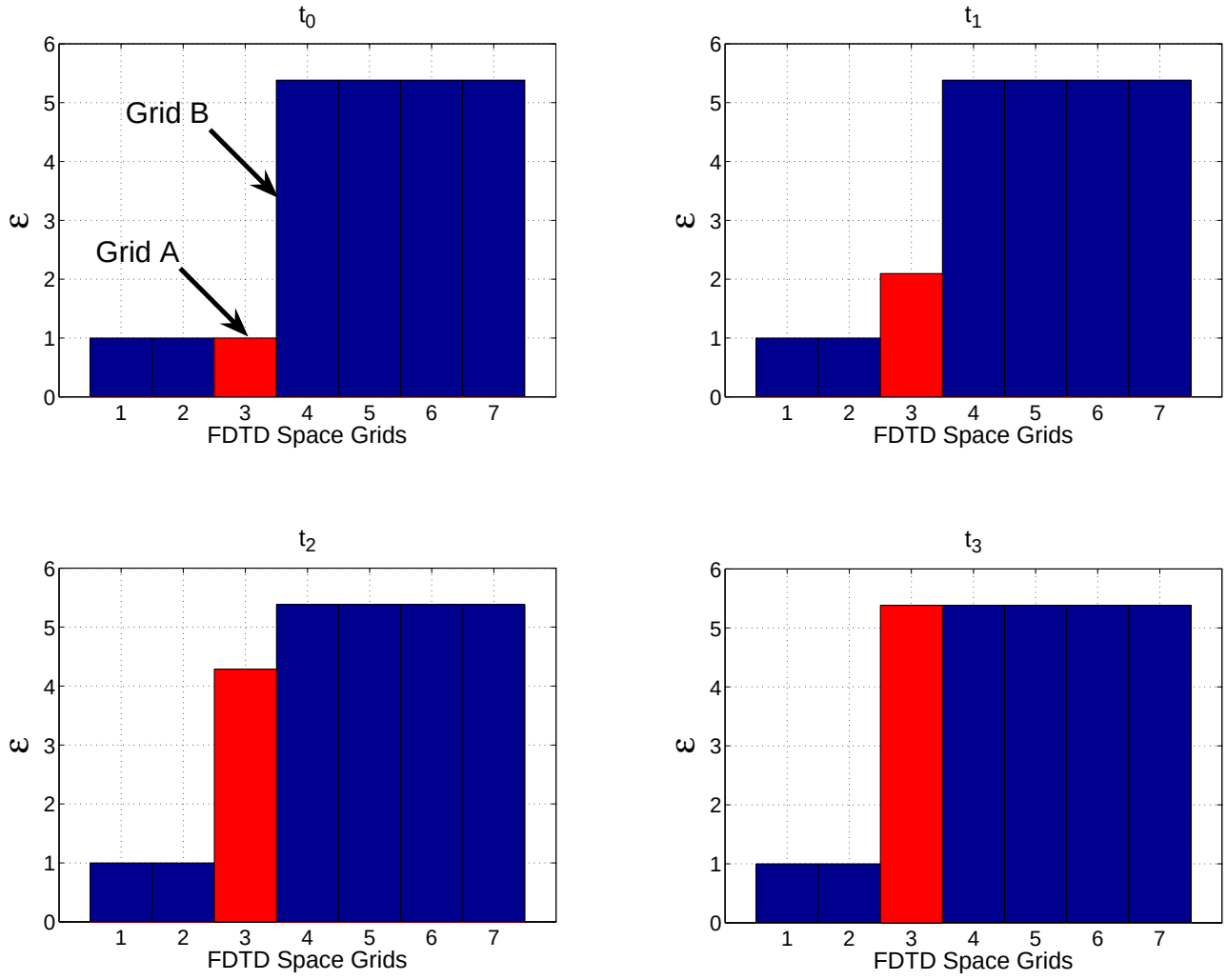

Figure 2.4: The dielectric constant of space grid 3 ("Grid A") is indicated in four different time steps. Initially at time t_0, ϵ_a=1 which is the dielectric constant of air. At times t_1 and t_2, the continuous motion of the moving layer is reflected in the dielectric value of space grid 3 ("Grid A"). The dielectric value at this grid increases linearly. At time t_4 when the moving layer actually reaches to the space grid 3 ("Grid A"), the dielectric constant value of this grid is becomes equal to the dielectric constant value of the moving layer ϵ_b=5.3.

the dielectric value of the space grid 3 ("Grid A") is ϵ_a=1, which is the dielectric constant of air. At time t_1, since the moving layer gets closer to the space grid 3 ("Grid A"), the dielectric value of this grid is linearly increased. Since the edge of the moving layer is closer to the space grid 4 ("Grid B"), the dielectric value of the space grid 3 ("Grid A") is closer to its original value as expected from the above equations. However, at time t_2, the moving layer edge is closer to the space grid 3 ("Grid A"), and consequently the dielectric constant value at this grid is closer to the dielectric value of the moving layer. Finally, at time t_3, the moving layer completely reaches to the space grid 3 ("Grid A") and the dielectric value at this grid becomes ϵ_a=5.3, which is the dielectric constant value for the moving layer. When these events are interpreted in the FDTD simulations, at each time step the material properties associated with the space grid 3 ("Grid A") are changing but this change is much smaller when compared to the no interpolation case. Consequently, in the simulation there is never an instantaneous jump in material properties and FDTD calculations can adapt to the linearly and slowly increasing material properties in a stable manner. This in turn solves the accuracy and stability problems that can be encountered in the no interpolation case.

At this point, it is important to relate the accuracy and stability of the linear interpolation method to the velocity of the moving structure. The dielectric constant value for the space grid 3 ("Grid A") of Fig. 2.3 and Fig.2.4 is plotted as a function of time in figure 2.5 for three different velocities of the moving layer of Fig. 2.2. V_1=0.01×c, V_2=0.002×c, and V_3=0.001×c where c is the speed of the light in free space. For all three cases, the dielectric values for the no interpolation cases show big jumps at 200^{th}, 600^{th}, and 1100^{th} time steps of the simulation. With interpolation case on the other hand provides a linear increase in the dielectric values, and the speed of this increase (slope of the linear line) is a function of the velocity as can be observed in this figure. As the velocity of the moving layer increases, the slope of the linear line created as a result of the linear interpolation method increases and gets closer to the no interpolation case. However, linear interpolation enhanced FDTD simulations still more accurately models the motion in the structure. Ultimately, it can be asserted that the linear interpolation method always provides a better estimate for the motion, yet its efficiency and accuracy resembles to that of no interpolation case as the

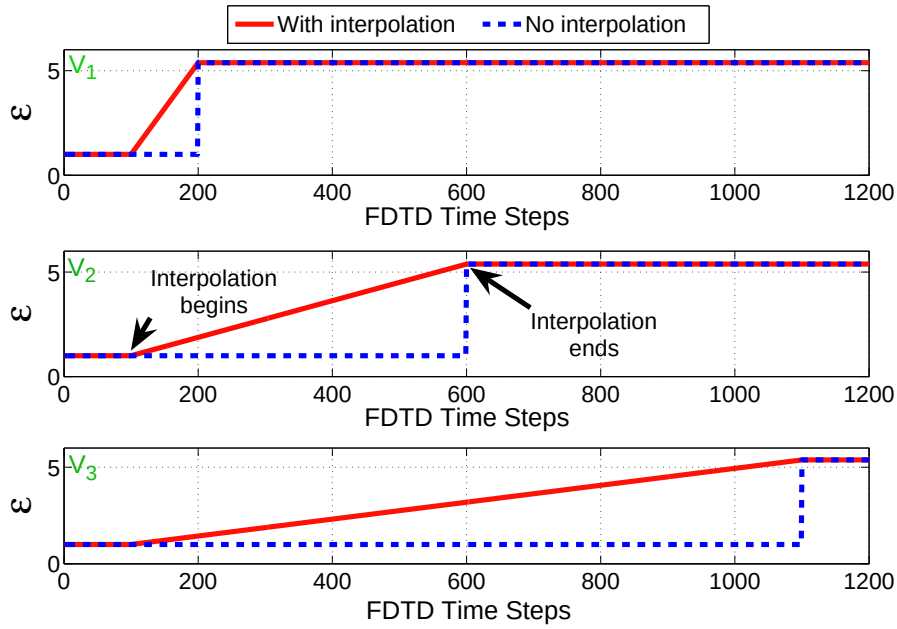

Figure 2.5: The dielectric constant value for the space grid 3 ("Grid A") of Fig. 2.3 and Fig.2.4 is plotted as a function of time. Three different velocities of the moving layer of Fig. 2.2 are used, and results are shown for with and without interpolation cases. V_1=0.01×c, V_2=0.002×c, and V_3=0.001×c where c is the speed of the light in free space.

velocity of the moving structure increases. A more detailed analysis on the velocity and simulation accuracy will be conducted in section 2.4.

Until this point, linear interpolation method is discussed from a 1D point of view. However, this method can also be easily applied for 2D cases where the motion is not only in one dimension. In addition, it is important to note that even in 2D, this method will still be very easy to implement and provide very good results without increasing the computation complexity and time. In the following, detailed information about the implementation of 2D linear interpolation will be presented.

Fig. 2.6 indicates a moving layer at two different time steps, t_0 and t_1. The dielectric constant for the moving layer is set to be ϵ_1 and the dielectric constant for the rest of the FDTD domain is set to be ϵ_0. To be able to implement the 2D interpolation, we keep track of two separate grid structures. The first one is the stationary main FDTD grid indicated in this figure by red circles, and the second one is the moving grid indicated in this figure

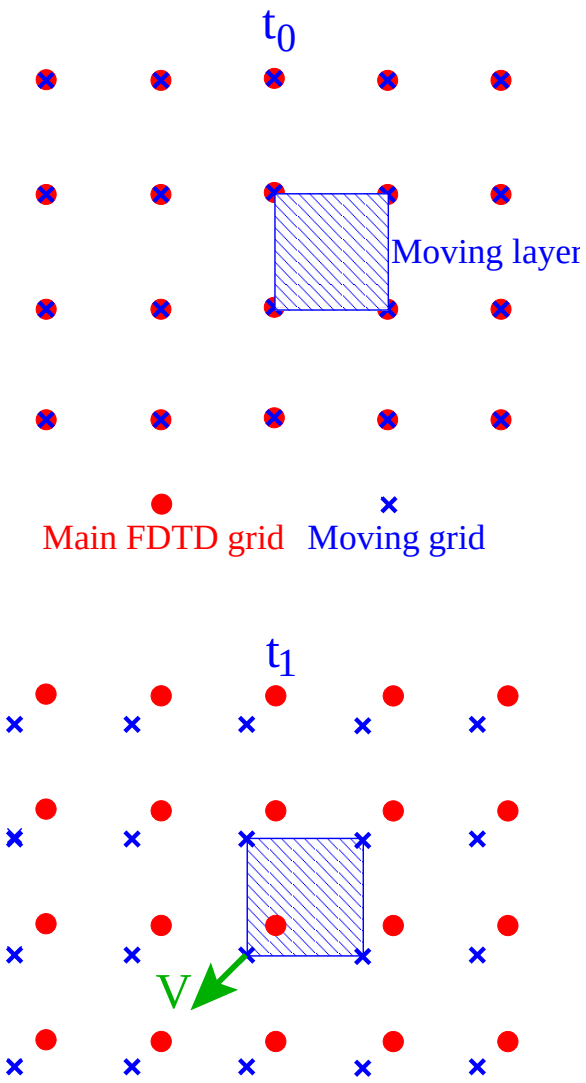

Figure 2.6: A moving layer in 2D FDTD grid is indicated at two different times, t_0 and t_1. The circles represent the stationary main FDTD grid, and the crosses represent the moving grid. The layer moves with a velocity of V in the indicated direction.

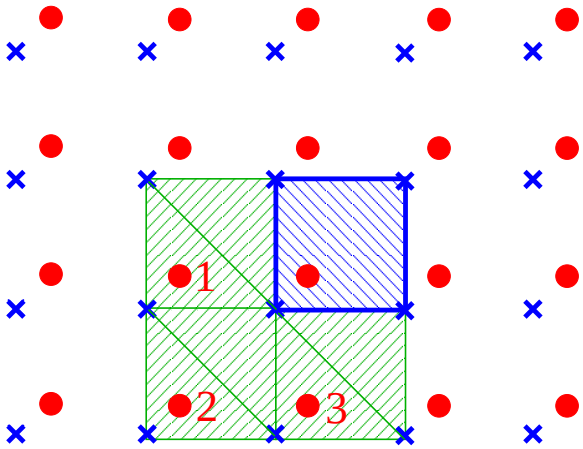

Figure 2.7: The whole grid structure is divided into squares for three different cases around the moving layer (only these three squares are shown for convenience, but in the actual algorithm the whole grid structure is divided into squares). Each of these squares include a point of the main grid, for which we want to calculate the interpolated dielectric value.

with blue crosses. The main FDTD grid is the one that is used to calculate the material properties and field values in the simulation. The moving grid on the other hand includes the moving structures and the motion of the objects is represented by moving this whole grid above the stationary main grid. In Fig. 2.6, initially at time t_0 both grids lay on top of each other. When the moving layer moves to the position indicated in time t_1, the whole moving grid structure moves with it and creates the grid structure indicated in figure.

In the next step, the whole grid structure is divided into squares as indicated in Fig. 2.7 for three different cases around the moving layer (only these three squares are shown for convenience, but in the actual algorithm the whole grid structure is divided into squares). Each of these squares include a point of the main grid, and to calculate the new dielectric values for each of these points, the following 2D linear interpolation calculation is conducted.

Fig. 2.8 briefly summarizes the 2D interpolation for a single square. First of all, the square is divided into two regions (1 and 2) as indicated. Then, depending on the position of the main grid point, three moving grid points are chosen to implement the interpolation. In this case, the main grid point for which we want to calculate the new dielectric value for is in region 1. As a result, dielectric values of points A, B, and C of the moving grid are used to do the interpolation. After the three points are chosen, a 3D linear surface

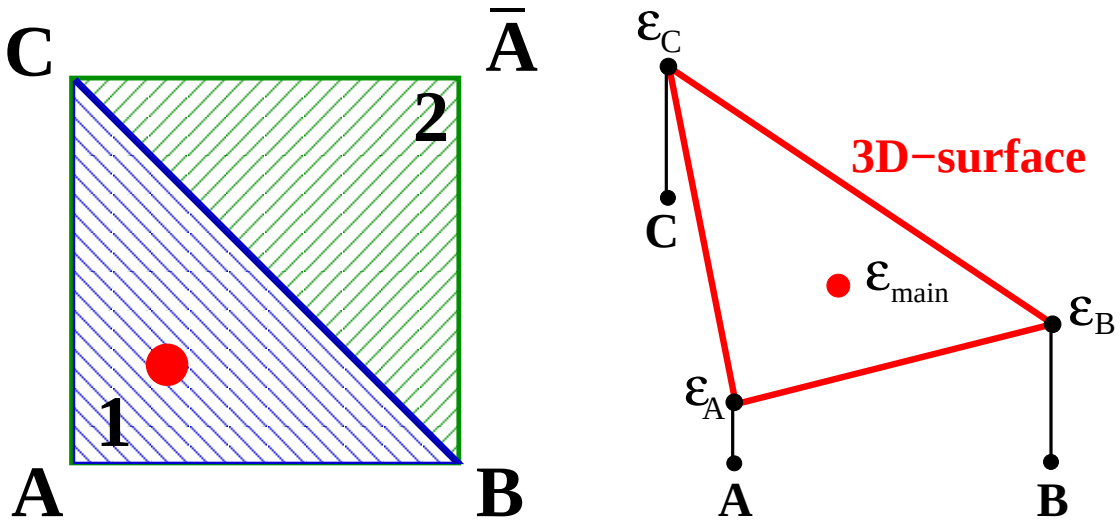

Figure 2.8: 2D linear interpolation algorithm for a single cell is explained in two steps. Each cell of Fig. 2.7 is divided into two regions (left), and a 3D surface is created using the dielectric values of the points that are at the corners of the triangle that includes the main FDTD grid (right).

passing through all these points are created, as shown in Fig. 2.8 (right). The created surface passes through points A, B and C in this case and has the values ϵ_A, ϵ_B, and ϵ_C in the third dimension. Finally, the value of the ϵ_{main} which represents the dielectric constant of the main grid point in region 1 of Fig. 2.8 (left).

Fig. 2.9 shows the 2D interpolation for cell 3 of Fig. 2.7. Since the moving layer is located above this cell as shown in Fig. 2.7, the top two dielectric constant values are ϵ_1 which is the dielectric constant value of the moving layer, and the bottom two grid points have the dielectric value of the rest of the structure which is ϵ_0. In this case, we want to calculate the interpolated dielectric constant value for the main grid point marked "3". Since this point lies in the first region of the divided square, the moving grid points located on the left triangle of Fig. 2.9 will be used to calculate the dielectric value of the main grid point "3". Using these three points and their dielectric constant values in the third dimension, a surface will be created. Finally, the dielectric value of the main grid "3" will be found using this surface as explained in the previous paragraph.

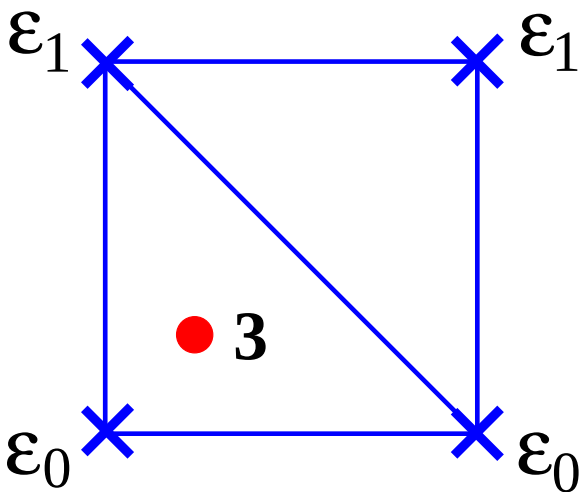

Figure 2.9: Application of the 2D linear interpolation algorithm to the cell 3 in Fig. 2.7

2.4 Test Case Performance

In this part, we will discuss the performance of the suggested "Linear Dielectric Interpolation" method. First, we will describe the test cases we used to determine the performance of the suggested method. Next, the details of setup and implementation of these cases in FDTD will be provided. Finally, results will be presented.

2.4.1 Description of test cases

In order to demonstrate the effectiveness of the linear interpolation method, we performed FDTD simulations to accurately model a moving dielectric mirror (a 1D photonic crystal). The interaction of a normal incident wave with a nine layer dielectric mirror consisting of two alternating refractive indices is tested using the following testbench in FDTD. The test case also includes a "hard source" which means that we are actually forcing a single point in the FDTD grid to have a specific field value in every time step. The locations of the source and the observation point are shown in Fig. 2.10.

Highly reflective dielectric mirror designs can be found in the literature [45]. Taking the dielectric mirror design in this reference as an example, we chose $n_H = 2.32$ and $n_L = 1.38$ for material indices. These specific values are chosen to produce a high reflection

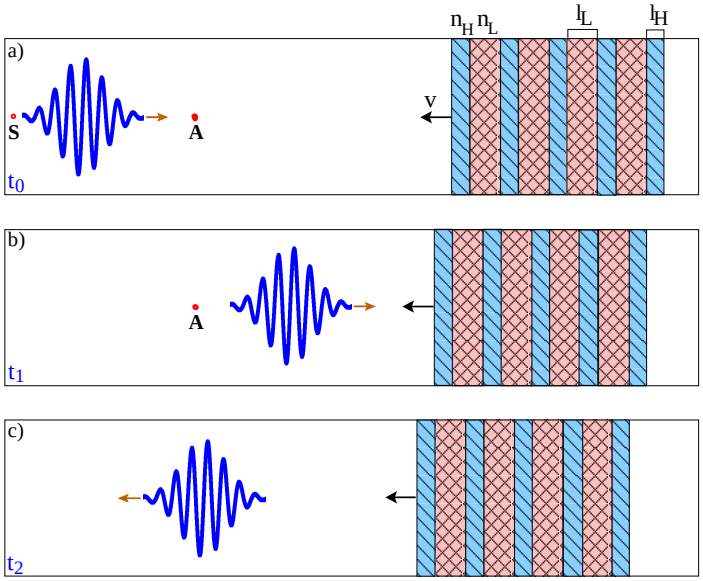

Figure 2.10: Dielectric mirror testbench showing the operation at 3 consecutive time steps. A wide Gaussian pulse is incident to a moving dielectric mirror consisting of nine layers with high and low refractive indices ($n_H = 2.32$ and $n_L = 1.38$). Layers have $l_H = 98$ nm and $l_L = 165$ nm thicknesses. The mirror is moving in the shown direction with a velocity of v. S indicates the source point and A indicates the observation point.

coefficient. Using the well-known formulas for the reflection coefficient of a dielectric mirror, we determine a reflection coefficient of

$$|\Gamma|^2 = |\frac{1 - (\frac{n_H}{n_L})^8}{1 + (\frac{n_H}{n_L})^8}|^2 = 98.84\% \tag{2.23}$$

which is a sufficient value for the analysis that is conducted in this thesis. For the thin and thick layers of the dielectric mirror, we chose $l_H = 98$ nm and $l_L = 165$ nm to make the feature sizes appropriate for the nanophotonics domain. When these values are inserted into the following formula, which provides the appropriate wavelength for each reflection from the mirror layers to constructively add up:

$$n_H l_H = n_L l_L = \lambda_0/4 \tag{2.24}$$

the operating frequency and wavelength for the stationary nine layer mirror is calculated to be $f_0 = 330$ THz and $\lambda_0 = 910$ nm. Furthermore, since we want to simulate a moving structure in order to measure the effectiveness of the linear interpolation method, the im-

plemented dielectric mirror is programmed to move towards the source with a velocity of v, as indicated in Fig. 2.10.

The source used in this analysis is a Gaussian pulse with a wavelength λ_0. A Gaussian pulse is intentionally chosen as the source wave due to its easier theoretical and experimental analysis, because the Doppler shifted reflection is also a Gaussian with a modified amplitude, frequency, and standard deviation. It is also crucial to note that the source is arranged to have a wide Gaussian pulse envelope so that in the frequency domain it will be easier to observe the Doppler shift. Another important factor is the duration of the pulse. This value is chosen such that the reflected wave from the dielectric mirror will not overlap with the source wave at the observation point so that the input and output frequencies can be observed separately. FDTD instability issue is the other effect on the chosen duration and standard deviation values of the pulse. Since the source used in this case is a hard source, it has to be stopped at a time step when the amplitude of the field emitted from it is almost zero. Consequently, after some experiments and calculations, pulse duration and standard deviation values of the source are arranged in order to minimize the instability occurring in FDTD simulations. When these values are used, the source turns off very smoothly without any instability.

At this point, it is also important to note that we specifically chose the described dielectric mirror as our test case to demonstrate the effectiveness of the linear interpolation method, because it is a good example of a moving 1D Photonic Crystal (PhC) and it has feature sizes that are of the same scale as the wavelength of light.

2.4.2 Implementation in FDTD

The test mechanism described in Fig. 2.10 is modeled using a 1D FDTD simulation. Details related to FDTD implementation of this specific test case are as follows. The time step of the simulation is $dt = dx/c_0 = 0.166$ fs, where c_0 is the speed of light in free space, and the spatial step size is implemented to be $dx = 0.05$ μm. The perfectly-matched layer (PML) boundary condition is used along the edges of the computational domain in order to eliminate the reflections from the FDTD simulation boundaries.

The first problem encountered at the FDTD implementation step is that when the layer

lengths l_L and l_H of the previously discussed dielectric mirror are discretized using this specific dx value, the structure did not behave as expected due to the insufficient sampling number. There are two solutions to this problem 1) decreasing the dx value 2) increasing the lengths l_L and l_H. Decreasing the dx value increases the resolution of the FDTD simulation sampling, so it causes a considerably longer simulation time. Consequently, the second solution − increasing the lengths l_L and l_H − is implemented using $\lambda_0/4$ length addition to the layer thicknesses of the dielectric mirror. By adding $4\lambda_0/2 = 2\lambda_0$ to each layer, the exact same reflection coefficient is obtained (theoretically and experimentally) for the dielectric mirror, and the sampling problem is solved.

When the dielectric mirror moves with a velocity of v, the center frequency for which this structure behaves as a perfect mirror shifts slightly. Consequently, the source velocity is adjusted by a factor of $(1-2v)/(1-v)$ to account for the Doppler shift [50]. So, the input frequency becomes $f = f_0(1-2v)/(1-v)$ when the dielectric mirror is moving with a velocity of v. When a Gaussian pulse with a central frequency f and a standard deviation σ is used as an incident wave to a moving dielectric mirror system with the previously calculated reflection coefficient, the amplitude, frequency and standard deviation of the reflected wave can easily be calculated theoretically. The frequency of the reflected wave becomes $f(1+v)/(1-v)$ and its standard deviation becomes $\sigma(1-v)/(1+v)$.

A reasonable method to prove the advantage and functionality of applying linear interpolation method to model moving structures in FDTD is to first calculate the FDTD numerical error associated with a case where the linear interpolation method is applied. Then to calculate the numerical error for the exact same case but without interpolation, and compare these two error values. In this paragraph, the method used to calculate this error is described. Basically, for a certain velocity v of the dielectric mirror, a Gaussian pulse is transmitted towards the dielectric mirror. The theoretically correct reflection is calculated using the previously calculated frequency and standard deviation values for this case. Then this mechanism is simulated using FDTD both with and without interpolation. The error signal is calculated as the difference between the FDTD waveform and the theoretical reflected waveform. We use the energy in the error signal as a measure of the accuracy of the simulation. The error energy is normalized by the theoretical waveform's

energy and we report the difference as a percentage error.

2.4.3 Results

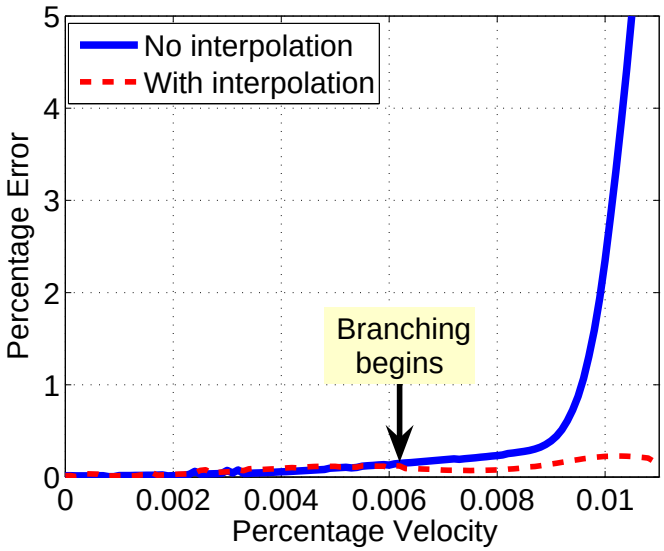

Figure 2.11: Velocities that are very close to zero are tested. $0\% - 0.011\%$ c velocity range is simulated with 0.0001% c increments, and percentage error associated with each of these velocities are plotted. The interpolation and no interpolation cases have the same percentage error value at $V = 0$, yet they make a branch around $0.006\%c$. The percentage error difference increases as a function of velocity after this point.

As mentioned above, the dielectric mirror in the testbench is moving towards the source with a velocity of v. In our analysis, we first tested velocities that are very close to zero, and the result is indicated in Fig. 2.11. In this figure, the vertical axis represents the percentage error in the reflected wave, and the horizontal axis represents the percentage velocity of the moving mirror. The reflected waveform in the simulation is compared with the theoretically calculated reflection, and the percentage error in the simulation is calculated to be the ratio of the error energy (difference between the simulation and theoretical reflections) to the total energy in the theoretical result. We theoretically expected that the interpolation and no interpolation cases would have the same percentage error value at zero velocity and with increasing velocities, they would make a branch because no interpolation case cannot model the test structure as accurately as the interpolation case. This actually is the case as seen

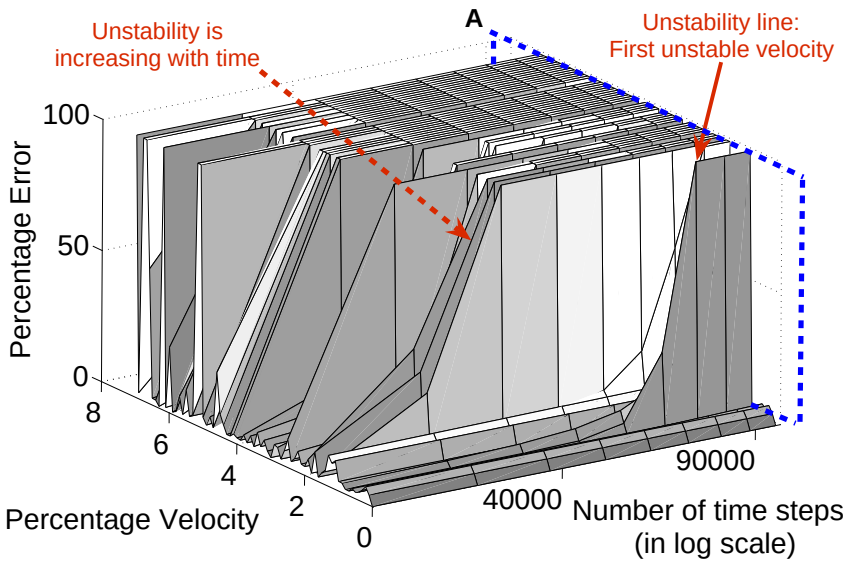

Figure 2.12: Percentage error is plotted as a function of percentage velocity and number of time steps using the no interpolation case. $0\% - 7\%$ c velocity and $18 \times 10^3 : 10^5$ time step ranges are used. Number of time steps are shown in logarithmic scale. First unstable velocity and a ramp indicating a percentage error increase as a function of time are marked.

in Fig. 2.11. After the velocity of the dielectric mirror passes the 0.006% c, percentage error associated with the no interpolation case starts increasing and reaches to 5% at $v = 0.011\%$ c. The interpolation case on the other hand, remains on the small percentage error values due to its higher accuracy.

In the next test that is conducted, our goal is to determine an instability velocity line for the no interpolation case. In other words, we aim to find a velocity value after which the no interpolation case becomes unstable and cannot model the proposed testbench structure. Consequently, we simulated the $0\% - 7\%$ c velocity range without linear interpolation. Each velocity is also simulated as a function of number of time steps, and percentage error related to each velocity at each time step is plotted in 3D as shown in Fig. 2.12. As can be observed from Fig. 2.12, at specific velocity values, percentage error value reaches to 100%, which points to an important instability condition in the simulation. For instance, around 2% c velocity, percentage error increases as a function of time, makes a ramp and reaches 100% error value. The cross section indicated by the rectangle A is plotted in Fig. 2.13 to be able to easily observe the instability border line associated with different velocities. As indicated

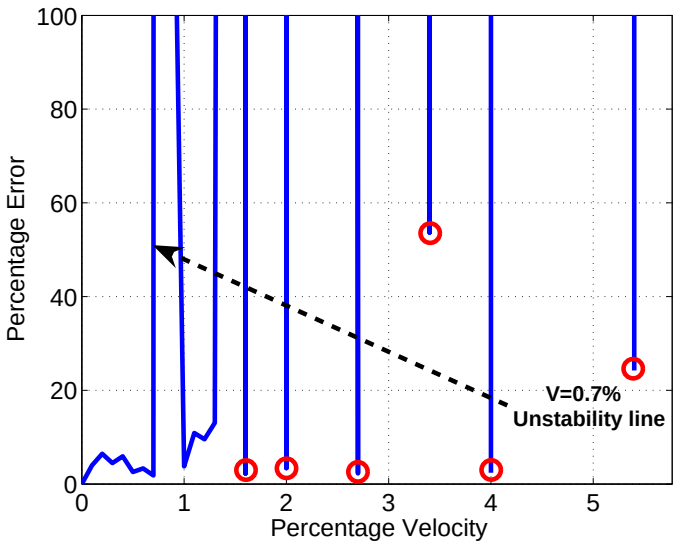

Figure 2.13: Cross section of Fig. 2.12 cut by the rectangle A is plotted. Percentage error as a function of percentage velocity is indicated. The number of time steps used is 10^5. First unstable velocity for the no interpolation case is shown to be 0.7% c. Most of the velocities after this border are unstable, so have 100% percentage error. The exceptions are indicated by small circles.

in Fig. 2.12 and Fig. 2.13, no interpolation case becomes unstable at $V = 0.7\%\ c$ value for the first time. Furthermore, no interpolation case is unstable for most of the velocities after $V = 0.7\%\ c$. There are some exceptions as shown in Fig. 2.13 by small circles, yet the number of these velocities is very low. As a result, $V = 0.7\%\ c$ velocity can be taken as the unstable velocity border for no interpolation case.

At this point, it is also important to mention the effect of motion in FDTD simulations on the Courant stability criterion. The Courant stability condition indicated in equation 2.18 defines the range and limits of the discrete time and space steps for the stationary FDTD simulations. However, when there is motion in the system, these range and limit values will be affected, and the stability condition in this case might be more restrictive than the well-known Courant condition. In the presence of motion in the system, the stability condition is expected to be a function of the maximum structure velocity in the system.

The next test is to determine how accurately the interpolation and no interpolation cases model the Doppler shift associated with the moving dielectric mirror. In Fig. 2.14,

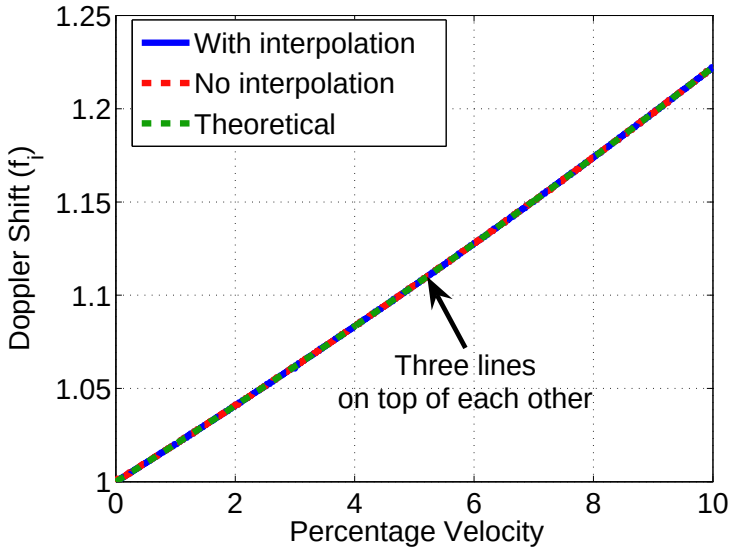

Figure 2.14: Doppler shift amount is plotted as a function of percentage velocity in $0-10\%$ c range. Theoretical, with interpolation, and with no interpolation results are shown. The values at the Doppler shift axis are scaled by frequency of the incident wave f_i. We can see that theoretically expected Doppler shift is present in both the interpolation and no intepolation cases in this velocity range.

theoretical, no interpolation and with interpolation Doppler shift amounts are plotted as a function of percentage velocity, in the velocity range $0-10\%$ c. Basically, for a specific velocity, both incident and reflected waves are Fourier transformed into the frequency domain. Then, the ratio of the frequencies corresponding to the highest magnitudes is calculated and plotted. Doppler shift amounts indicated in the graph are to be scaled by the incident light frequency. For example, 0.1 value on the Doppler shift axis indicates a Doppler shift of $(0.1 \times \ f_i)$ where f_i indicates the frequency of the incident wave. As can be observed from Fig. 2.14, theoretically expected Doppler shift is present in both the interpolation and no interpolation cases in this velocity range. This is an expected result because while plotting this figure, we filter out all the spurious frequency content, and we are only interested in seeing if the expected Doppler shift is present (or not) in the frequency spectrum of these two cases.

Although the no interpolation case indicates the same results with interpolation case in terms of approximating the Doppler shifted frequency, spectral analysis shows the advan-

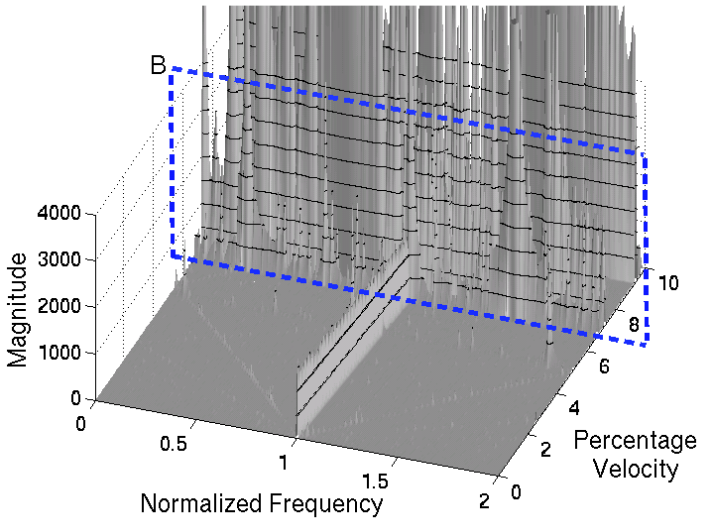

Figure 2.15: Frequency spectrum is plotted as a function of percentage velocity in $0-10\%$ c range for the no interpolation case. The frequency axis is normalized to the f_0 frequency value for which the dielectric mirror provides the highest reflection coefficient. We can see that although the Doppler shifted frequency is present in the frequency spectrum, many non-physical harmonic frequencies also exist, especially after the 6.5% c velocity value as a result of the instability effects.

tage of using the linear interpolation method. In Fig. 2.15, frequency spectrum of the no interpolation case is plotted as a function of velocity, and in Fig. 2.16 we focused to $1-1.5$ normalized frequency range for both with and no interpolation cases. As can be observed from these figures, Doppler shifted frequency exists in the frequency spectrum, which is a proof of the results indicated in Fig. 2.14. However, when these figures are examined in detail, we encounter higher (and lower) non-physical harmonic frequencies in the spectrum of no interpolation case. These frequencies emerge as a result of the instantaneous jumps in the material properties, which occur because of the space discretization. With the additional effect of instability at higher velocities, more dramatic erroneous frequency values are observed after 6.5% c velocity value. On the other hand, the interpolation case filters almost all of these spurious frequency content and provides a more accurate frequency spectrum as indicated in Fig. 2.16 (bottom).

In the next figure, Fig. 2.17, the cross section of Fig. 2.15 indicated by the rectangle B

is plotted. This figure shows the frequency spectrum associated with incident and reflected waves. Two different cases are used to plot the frequency content of the reflected wave 1) With interpolation case 2) No interpolation case. In this simulation, specific 6.8% c velocity value is used because it is the first velocity in which dramatic erroneous frequencies are present. The frequency axis is normalized to the f_0 frequency value for which the dielectric mirror provides the highest relection coefficient. The incident wave has a frequency of $f = 0.927 \times f_0$. At this velocity, the Doppler shift should be $f \times (1+0.068)/(1-0.068) = 1.063 \times f_0$. In Fig. 2.17, we can see that the interpolation case models this very accurately and it has a single frequency component at $1.063 \times f_0$. The no interpolation case has a component at the right frequency, too, which we can not see because of the instability. However, it also has many non-physical frequency components. This is a very good indication of how effective the interpolation method is. Without the use of this techniques, it becomes very hard to accurately model Doppler frequency shift.

As the last test to prove the effectiveness and benefit of the linear interpolation method, we plotted the percentage error as a function of the velocity in the $0-13\%$ c range as shown in Fig. 2.18. Percentage error is indicated for with and without interpolation cases. As can be seen from Fig. 2.18, linear interpolation provides much better results when compared to no interpolation case. First of all, until 8% c velocity, linear interpolation incurs much less percentage error. In this velocity range, no interpolation case becomes unstable many times reaching to very high error values. After this velocity, even though we see an increase associated with the percentage error of the linear interpolation method, it still continues to be a better approximation than no interpolation case. This percentage error increase is a result of the velocity, because with increasing velocity, slope of the linear change in material properties increases. In other words, rate of change of the material properties increases, which is the actual problem for the no interpolation case.

When we take the minimum percentage error envelope of the no interpolation case, linear interpolation method provides very good results. Fig. 2.19 shows the linear interpolation and minimum centered no interpolation cases in logarithmically scaled percentage error graph. As expected and shown in Fig. 2.19, linear interpolation method performs much better till 8% c velocity, and starts to look like no interpolation cases at higher velocities.

When we take the ratio of the minimum centered no interpolation error value to linear interpolation method error value, we get the result indicated in Fig. 2.20. As can be seen in this figure, in average with interpolation case provides $15 - 20$dB better results until 8% c velocity. After this velocity value, the ratio decreases due to the resemblance of the interpolation case to no interpolation case.

2.5 Future Work

Results presented in this section indicate that the linear dielectric interpolation method is a very useful, accurate and efficient enhancement for FDTD simulations that include moving structures. However, it is also possible to make some improvements to this method, to increase its capabilities and efficiency. In this subsection, possible improvements, adjustments, and extensions for this method will be presented.

First of all, for the extension of the method into two and three dimensions, the linear interpolation method is expected to perform similarly and model the effects of the velocity significantly more accurately because increasing number of possible movement dimensions decrease the accuracy of FDTD simulations. Consequently, applying linear interpolation method in these cases is expected to result in an increased level of error reduction and accuracy. In section 3 2D version of the linear interpolation method is already implemented to model the proposed structures, and it provided very good results in terms of stability and accuracy. Furthermore, this method can easily be extended to three dimensions, and we expect to see relatively higher stability and accuracy in this case. However, a 3D version of the algorithm is not implemented and tested, and this can be a useful extension of this method.

Another possible extension of the linear interpolation method is the "quadratic interpolation". In this case, a quadratic equation will be used to calculate the FDTD coefficients that represent the material properties in the main FDTD grid. For example, this method can be used when the moving structure in the simulation has a nonzero conductivity (σ). In this case, the FDTD coefficients perform a quadratic behavior, and a "quadratic interpolation" method is required in order to accurately model this behavior.

In addition, "spatial averaging" is another extension of the linear interpolation idea. In this case, the dielectric values for the whole spatial grid (in comparison to the linear interpolation method which only uses the grid points for the interpolation) is used to calculate the new dielectric value of the required spot. This is also a good estimate of the motion of the structure and is also expected to provide high accuracy and stability for modeling motion in FDTD simulations.

Finally, a more detailed analysis is required on the stability issue of the FDTD simulations that include motion. As mentioned previously, in this case, the motion in the simulation will affect the reliability and validity of the well-known Courant condition on stability, and will probably make it more restrictive. We expect the new stability criterion to be a function of velocity, which overlaps with our stability results indicated in section 2.4. In this thesis, we tried to define the new stability condition numerically (using simulation), yet analytically deriving this condition can also be listed as an important future work.

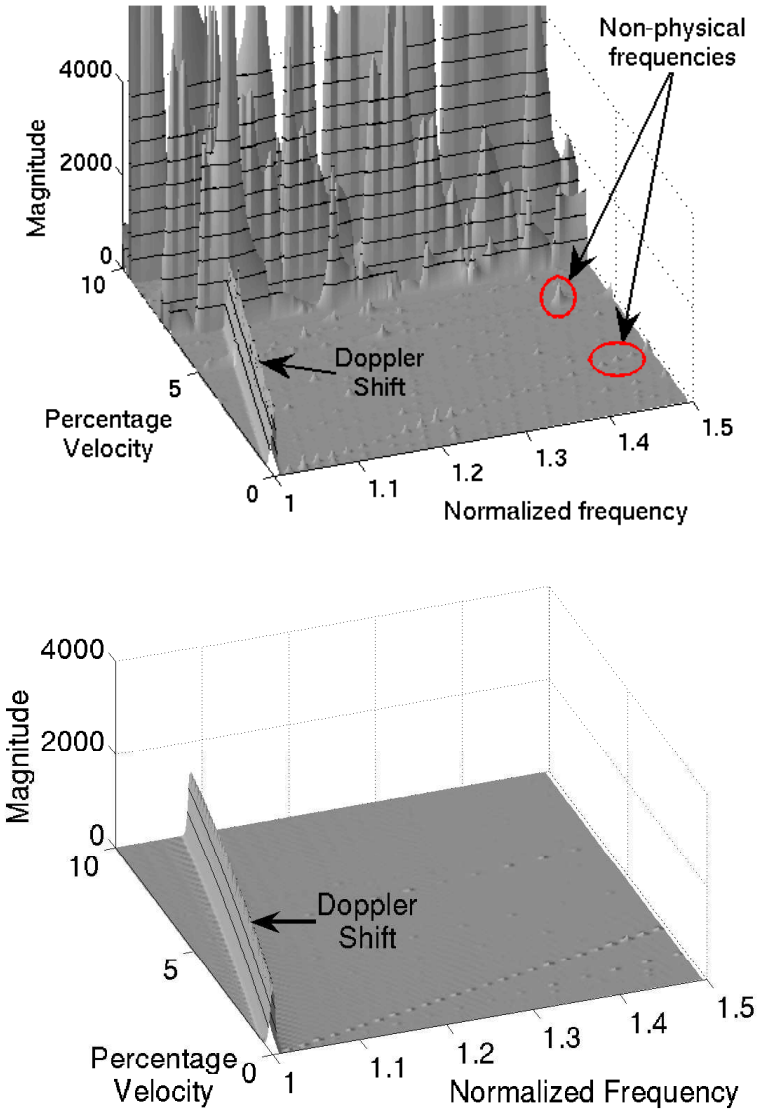

Figure 2.16: Frequency spectrum as a function of percentage velocity in $0-10\%$ c range for the with (bottom) and no (top) interpolation case when zoomed in to the $1-1.5$ normalized frequency range. The frequency axis is normalized to the f_0 frequency value for which the dielectric mirror provides the highest reflection coefficient.

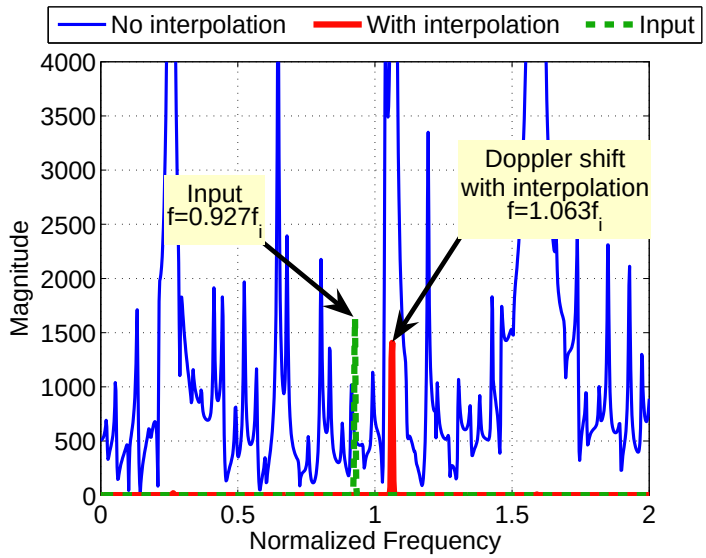

Figure 2.17: Frequency spectrum of the incident and reflected waves at 6.8% c velocity is plotted for two cases: 1- Interpolation case 2-No interpolation case. Doppler shift is very accurately modeled using the interpolation method. The no interpolation case on the other hand, has various dramatic, erroneous and nonphysical frequency components.

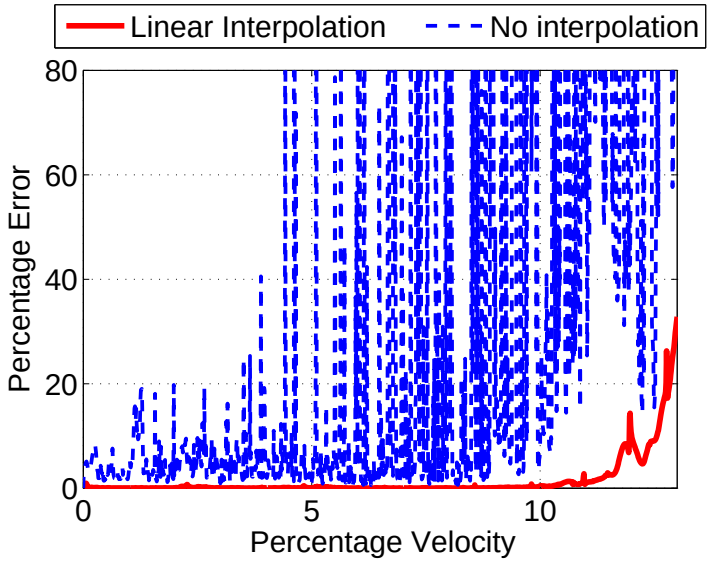

Figure 2.18: Percentage error is plotted as a function of the velocity in the $0-13\%$ c range. Percentage error is indicated for with and without interpolation cases. Until 8% c velocity value, linear interpolation method provides a much better performance. After this velocity, the linear interpolation case starts to look like no interpolation case.

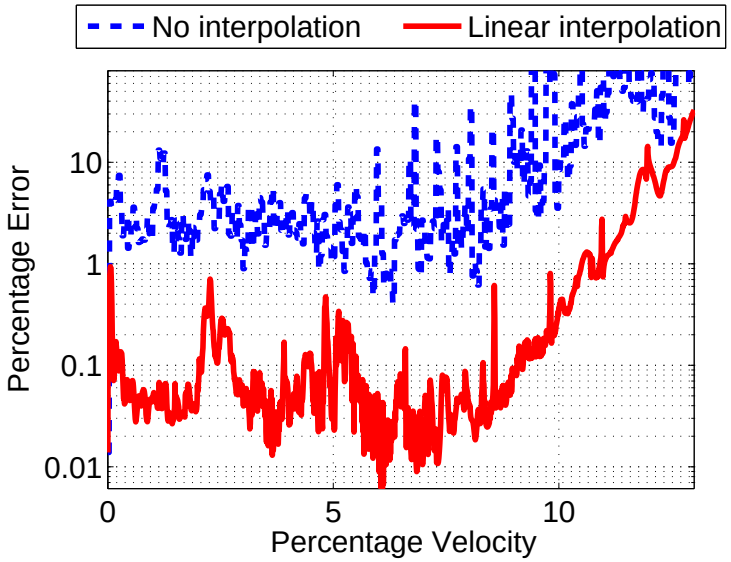

Figure 2.19: Percentage error is plotted as a function of the velocity in the $0-13\%$ c range in a logarithmic scale. Percentage error is indicated for with and without interpolation cases, but the lower envelope of the no interpolation case is taken. Until 8% c velocity value, linear interpolation method provides a much better performance when compared to the best case no interpolation error value. After this velocity, the linear interpolation case starts to look like the minimum envelope of the no interpolation case.

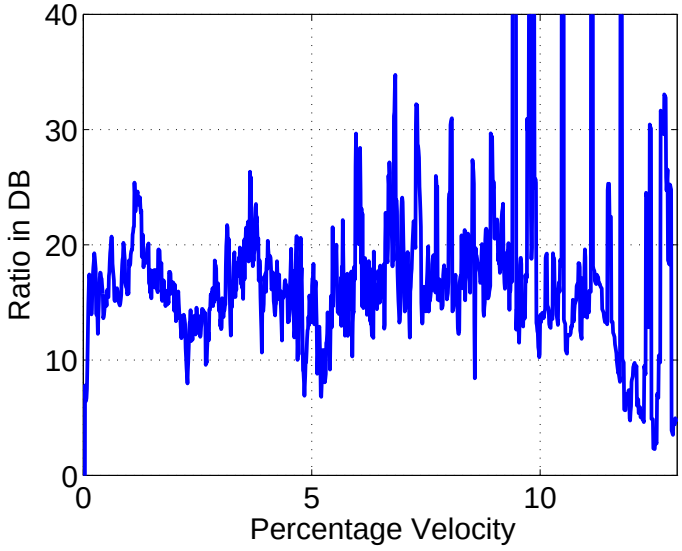

Figure 2.20: Ratio of the minimum envelop of the no interpolation error to the linear interpolation error in units of decibel(db). Until 8% c velocity value, linear interpolation method provides almost 20dB better percentage error.

Chapter 3

Wavelength Conversion Using PhC-MEMS/NEMS Structures

There is a rapid increase in the bandwidth and transfer speed requirements of optical communications technology. Public communication systems, maybe the most important example of which is the Internet, use single-mode fibers which are capable of transmitting more than 1 Tb of data per second [61]. However, this enormous bandwidth cannot be totally utilized by the most advanced commercially available telecommunication systems. This implies that very large amounts of data can be sent very fast between specific network nodes of today's optical communication systems, yet this data cannot be processed and routed to correct destinations fast enough at these nodes. The reason of this limitation will be identified and discussed in the following.

Wavelength-Division-Multiplexing (WDM) emerges to be the most popular technique applied and used in today's optical communications networks. Fig. 3.1 shows an optical cross connect associated with a WDM system. Basically, the data is transmitted on a carrier frequency in the optical fiber, and it is amplitude modulated to provide the bit stream of the data. The carrier frequency of the signal identifies the data channel. The cross connect in a WDM system is similar to a network switch, and essentially distributes specific inputs to specific outputs.

Optical-electronic-optical (OEO) transitions in these cross connects, which implies con-

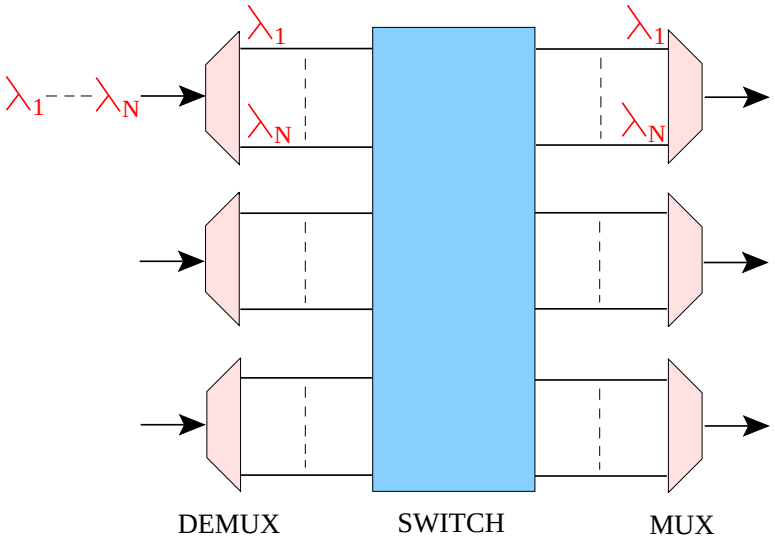

Figure 3.1: WDM Optical cross connect schematic. The schematic consists of 3 main blocks. The first one is the DEMUX (demultiplexer) array which is used to separate the incoming data channels. The switch block is responsible from the distribution and connection of the incoming data to the correct destinations. Finally, the MUX (multiplexer) block multiplexes the different data channels to a single output channel.

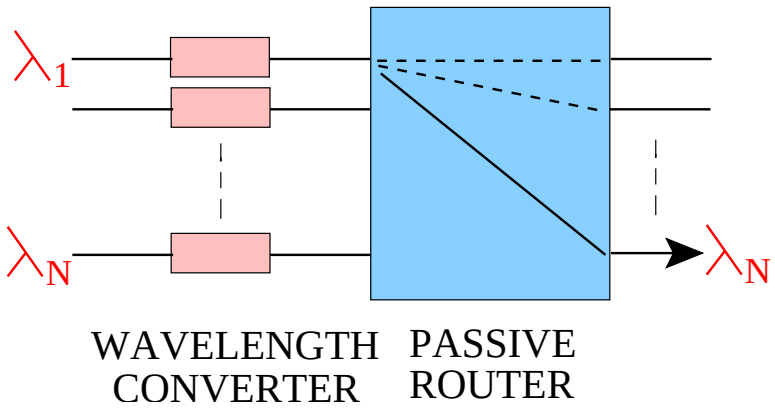

Figure 3.2: The switch block of Fig. 3.1 is indicated in more detail. There are two main blocks in this figure. The first one is the wavelength converter array. Wavelength converters are used to connect the data coming from one data channel to another one by changing the carrier frequency of the signal. Then the passive router provides the connection to the appropriate output channel.

version between optical and electronic domains, emerges to be a serious bottleneck for the satisfaction of the previously mentioned speed and capacity requirements. Transformation into the electronic domain is very costly and slow. Optical demultiplexing and multiplexing are well established parts of the cross connect block indicated in Fig. 3.1, while the switching block needs to be improved to solve the problems that occur due to OEO transitions [2, 4]. Consequently, there needs to be a way to solve this issue and increase the performance of these nodes to meet the increased bandwidth requirements of the communications industry. All-optical routing and networking seems to be the most suitable solution to this problem.

In Fig. 3.2, the switch block of this cross connect circuit is indicated in detail. There are two crucial components in this block: 1) tunable wavelength converters 2) passive router. This thesis will focus on the wavelength converter part of the switching block because this section suffers the most from the OEO transitions mentioned in the previous paragraph.

In this section of this thesis, an all-optical wavelength conversion method will be proposed and discussed as a solution to this problem. The proposed wavelength converter is composed of photonic crystals (PhC) and MEMS/NEMS structures. Both PhCs and MEMS/NEMS structures have very novel and interesting applications. However, they can be integrated to design much more novel and revolutionary structures. The proposed wavelength converter is such an example.

This section is organized as follows. In the first part, current wavelength conversion methods will be discussed. In the second and third parts, MEMS/NEMS and PhC structures will be reviewed. Next, the proposed PhC-MEMS/NEMS structures will be described in detail. Then, fabrication issues associated with the proposed structures will be analyzed. In the last part, results will be presented and discussed.

3.1 Current Wavelength Conversion Methods

Wavelength conversion is an important method that enables the connection of data from one carrier wavelength to a different carrier wavelength. In other words, it sets the destination of data from one specific data channel to another and enables wavelengths to be assigned on a link-to-link basis. Essentially, wavelength conversion is a very important

functionality in WDM systems and plays a very crucial role towards cost effective, high speed optical networks.

In this subsection, a brief analysis of the current wavelength conversion methods will be provided. Wavelength converters can be categorized in a few different ways depending on the criteria of differentiation [61]. First of all, depending on the optical signal routing mechanism, wavelength converters can be grouped into optical-electronic-optical and all-optical wavelength converters. Optical-electronic-optical (OEO) networking and routing implies conversion between optical and electronic domains. All-optical wavelength converters on the other hand provide conversion from one frequency to another using only the optical domain, do not require any conversions to electronic domain. As a result, this type of converters are much more efficient and reasonable in terms of cost and performance.

A second classification terminology could be in terms of the input-output signal characteristics. In this case, there will be three major groups: a variable-input-fixed-output converter, a variable-input-variable-output converter, and a fixed-input-variable-output converter. The keyword "variable" implies a possible range of wavelengths applicable, while the keyword "fixed" implies a specific and predefined wavelength. Even though each of these methods might have specific applications, having a variable-input-variable-output converter would be more desirable due to its flexibility.

Finally, depending on the mechanism used to create the conversion, wavelength converters can be classified into three major categories: optoelectronic, optical gating, and wavemixing. This will be the main classification this section will use in order to explain current wavelength conversion methods, and each of these methods will be analyzed in more detail in the following part.

Optoelectronic (O-E-O) wavelength conversion is the first class when the current wavelength conversion schemes are classified according to the applied mechanisms. In this case, the input optical signal is detected and converted to the electronic domain (O-E) at the input receiver end. Then, this electronic signal is retransmitted with the required frequency (E-O) at the output transmitter end. This mechanism is physically implemented using a receiver, an RF amplifier, and a laser [61]. This is a more straightforward conversion mechanism when compared to the others, and it is usually variable-input-fixed-output, unless a

tunable lasing mechanism is used.

The second category of the current wavelength conversion mechanisms is the optical gating wavelength conversion. Basically, this technique uses an optical device which changes its optical properties as a result of the input wave, and these modifications in the device are monitored and reflected to the output optical signal by means of a probe. There are many conversion methods in this category, each of which use different types of mechanisms to change the characteristics of the deployed optical device. Semiconductor optical amplifier cross-gain modulation, semiconductor optical amplifier cross-phase modulation, semiconductor lasers with saturable absorption, and nonlinear optical loop mirrors are the most crucial and popular ones [61]. This type of conversion technologies, which are also variable-input-fixed-output configuration, are less mature when compared to the optoelectronic case, and need more time to develop.

The third and last category is the wave-mixing wavelength conversion. Basically in this method, the input optical signal is modulated in a nonlinear material and this process creates an output signal with a converted wavelength. The output signal has an amplitude and phase which is a linear combination of the input and reference waves, and as a result of this, the wave-mixing wavelength conversion method preserves the phase and the amplitude information of the input signal. Since the superposition principle applies to the optical fields, there may be many simultaneous frequency conversions in these devices. Consequently, this is a variable-input-variable-output technique. This method is capable of working in very high data bit-rates, for example more than 100 Gbit/s as demonstrated in reference [61]. Four-wave-mixing in passive waveguides, four-wave-mixing in semiconductor optical amplifiers, and difference frequency generation are the three major wavelength conversion methods of this class.

When the various wavelength conversion mechanisms mentioned above are compared, all-optical wavelength converters appear to be a better choice due to their higher signal-to-noise ratio and higher conversion efficiency [61]. Also, optoelectronic wavelength conversion methods require higher power to operate, and this problem is solved in the all-optical converters. Ultimately, it can be asserted that a well designed all-optical wavelength converter will not only be more efficient and easier to integrate to the optical communication systems,

but will also provide much better performance.

Finally, at this point it is important to note that WDM makes wavelength conversion a practical necessity [25]. However, currently commercially available WDM systems use optical-electronic-optical conversions, optoelectronic wavelength conversion mechanisms. Due to the reasons mentioned above, having all-optical wavelength conversion mechanisms with variable-input-variable-output characteristics in the WDM systems of multiwavelength transport networks would be much more efficient and simple.

3.2 Micro/Nano-Electromechanical-Systems (MEMS/NEMS)

Micro-/Nano-electro-mechanical systems (MEMS or NEMS) seek to manipulate the nanoscale device structures to provide movable parts that can implement a variety of functions. These structures provide the ability of interacting with the environment not only in terms of gathering information (sensing), but also reacting against the environmental changes using special actuation mechanisms (most popular of which are electrostatic, piezoelectric, magnetic, and electrothermal) that can be controlled. Consequently, with the appropriate inputs, it is possible to program the MEMS/NEMS structures to any desired state. Common applications of these systems include inertial sensors, micro-motors and actuators, inkjet printer heads, biological and chemical delivery systems, optical switches, and "smart" sensors. As a result, MEMS/NEMS can provide a cost-effective, high-performance solution (that can also be significantly miniaturized) to various types of problems.

MEMs and NEMs are fabricated using the heavily commercialized CMOS fabrication processes. As a result, they provide the same potential benefits as large-scale electronic integrated circuits, such as low-cost high-volume automated fabrication and production. It is as a result of this fact that MEMS/NEMS have become so cost effective and so widely used in many applications. In addition to this, they have their own unique challenges due to the fact that they are also mechanical structures. There are two specific fabrication methods for MEMS/NEMS systems: Surface and Bulk micro-machining. Briefly, the main idea for surface micro-machining is to create devices by layer deposition and etching on a substrate. For bulk micro-machining on the other hand, the bulk itself is shaped to have a certain

feature using specific etching techniques such as back etching. A very essential part of the MEMS/NEMS fabrication is the sacrificial layer which is used as a temporary layer to get a certain gap in the structure. This gap is basically used for the motion capability of some parts of the device. A more complete analysis on the fabrication issues of MEMS/NEMS structures will be provided in section 3.5.

In this subsection, a brief review of MEMS/NEMS structures will be provided in three subcategories: 1) Optical MEMS/NEMS 2) RF MEMS/NEMS 3) MEMS/NEMS actuation and motion transfer methods. There are various other types of MEMS/NEMS applications but these specific categories are intentionally chosen for their relevance to this thesis.

3.2.1 Optical MEMS/NEMS

As mentioned in section 3.1, optical networks are moving towards being all-optical, where almost every function in the network are performed in the optical domain. However, optical networking today is still on a limited level due to missing high-optical low-cost optical components. Consequently, in the last years, there has been a rapid increase of interest in the silicon-based MEMS/NEMS structures for various optical networking applications. Optical switching, variable attenuators, and tunable lasers, all of which are the key elements of an optical network, are the main domains where MEMS/NEMS structures are gaining more and more importance in the optical network technologies. The main reason for this rising interest in these structures is their substantial cost and performance advantages [43].

It is already mentioned that the switching and routing signals in the electrical domain is a serious bottleneck for today's optical networks which are capable of operating with hundreds of wavelengths. Switching these wavelengths requires a large scale optical switch with many number of ports. This seems to be the most attractive area for optical MEMS/NEMS integration because optical MEMS/NEMS switches will essentially provide an all-optical solution to the switching function. A MEMS/NEMS micro-mirror array which consists of individually addressable micron-scaled mirrors is one of the possible and efficient methods to implement the switching function. Using electrical cross connects is the typical and traditional method for switching, yet the optical-electronic-optical transitions in this configuration are very costly, especially with the increasing bit rates in the network chan-

nels. An optical MEMS/NEMS solution to the switching would provide a lot of savings in terms of cost, power, and area [43].

Another popular application of MEMS/NEMS structures in the optical communications is in the area of variable optical attenuators (VOAs). One method to realize this is to use a vane that moves, and either closes or opens a hole, through which an optical beam is propagating [72]. Another method is using a MARS attenuator structure [69]. MARS attenuators use the fact that a quarter wavelength of silicon nitride, deposited on top of silicon, will create an almost perfect antireflective coating. If the same nitride layer is positioned a quarter wave above the silicon, it becomes a very good reflector. Consequently, a MEMS/NEMS membrane structure which can mechanically move this silicon nitride layer will work as an optical attenuator. The VOAs have a wide range of applications in optical networks, especially inside optical amplifiers, add/drop multiplexers, and optical cross connects and they function as the optical power controllers.

Another possible optical MEMS/NEMS application is in the area of tunable lasers and filters. One such device is designed and created by Coretek [68]. This is a tunable MEMS/NEMS optical laser with an active layer, cavity, and a supporting movable electrostatically manipulated membrane. The most effective way to create tunable lasers is physically changing the cavity length, and in this case it is done by changing the position of the dielectric mirror membrane. This particular device is tunable between 1.51-1.56 μm, which corresponds to a 50 nm wavelength span. These lasers have been tested with setups of 325 km length and gave bit error rates of less than 10^{-13} [68].

3.2.2 RF MEMS/NEMS

RF MEMS/NEMS refers to radio frequency operation which includes DC to submilimeter wavelengths, and is different from optical MEMS/NEMS which is in the infrared to ultraviolet wavelength range. In the literature, there are various types of RF components such as self assembled antennas and inductors, transmission lines, resonators, and cavities all of which are fabricated using the surface and bulk micromachining processes that are mentioned at the beginning of this section. A more detailed analysis about the current IC and MEMS/NEMS fabrication methods is conducted in subsection 3.5. However, none of these

components are reconfigurable and include actuation/motion. In other words, after they are fabricated, their structure is constant and it does not change. True RF MEMS/NEMS structures on the other hand are reconfigurable and motion in these systems is created by means of various types of actuation mechanisms.

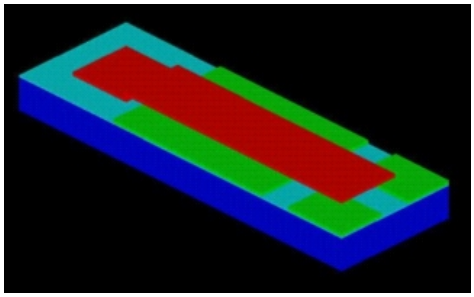

Figure 3.3: RF MEMS switch 3D view

RF MEMS/NEMS research and applications are not mature enough to replace the existing conventional solutions in RF circuits yet. Due to fabrication and packaging issues, RF MEMS/NEMS devices still need more time to develop and become commercially available, which is expected to happen soon. At the moment, the most fundamental and popular RF MEMS/NEMS components in the literature and industry are RF switches, variable capacitors, and antennas.

The most popular of these three component classes is the switches. They are mainly applied and used in attenuators, phase shifters, and filters. Back in 1995, an RF MEMS switch with a cut off frequency of $f_0 = 2$THz was reported [22]. After this, various RF MEMS switches with increasing performances are reported in the literature by different groups [53, 55, 8]. The most common method used for the actuation of RF MEMS/NEMS switches is the electrostatic actuation. Almost all of these switches consist of suspended bridges and cantilever beams. The diagram of a cantilever RF MEMS switch is indicated in Fig. 3.3 in a 3D view. This switch is electrostatically activated using the large green contact below the red cantilever beam. When the red cantilever and the green contact below it have opposite charges, the MEMS cantilever beam closes and connects the two different nodes of the RF circuits (These nodes are indicated with small green contacts at the right hand side of the view). When they have the same charge polarities, the contact pushes the MEMS

(a)

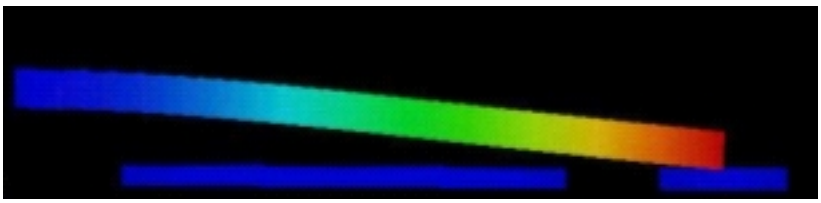

(b)

Figure 3.4: RF switch side view indicating open and closed configurations

cantilever up and the switch gets into its OFF state. The switching activity is indicated in Fig. 3.4. In (a), the switch is OFF, and in (b) the switch is ON. It is also important to note that the gap between the activation contact and the cantilever beam is created using the sacrificial layer concept of surface micromachining MEMS/NEMS technology.

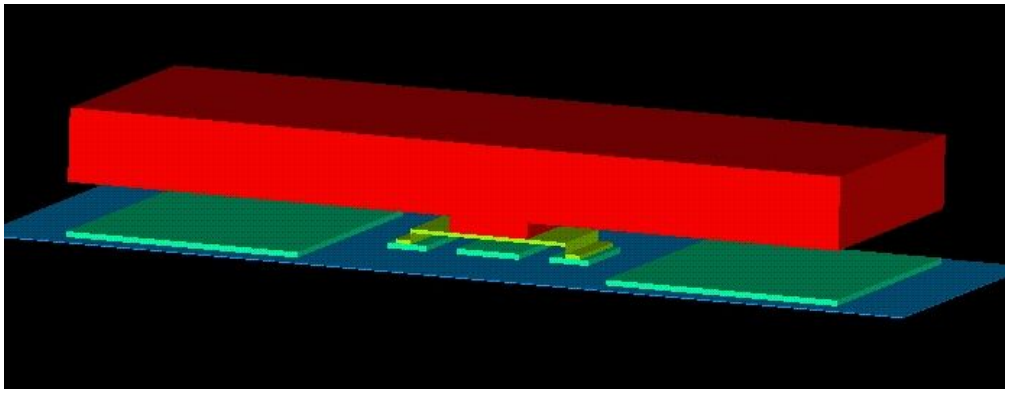

Figure 3.5: RF MEMS varactor 3D view

Another popular RF MEMS/NEMS component class is the variable capacitors, varactors in other words. Varactors are very crucial elements for RF phase shifters, filters, and antennas. Various RF MEMS/NEMS varactor designs have been reported in the literature

and industry [12, 9]. Some of these designs are created using surface micromachining and some are created using bulk micromachining. Similar to switches, the RF MEMS/NEMS varactors are also mostly electrostatically actuated. However, electro-thermally activated designs are also reported in the literature [17]. An example configuration for electrostatically actuated variable capacitors is indicated in Fig. 3.5 in a 3D view. This is a reconfigurable parallel plate RF MEMS/NEMS variable capacitor. The red layer is the top plate of the varactor, and the two large green contacts on the substrate create the bottom plate. The red beam is attached to the substrate with an electrostatically actuated suspended bridge. When the small green contact and the yellow suspended bridge have opposite charges, the bridge bends and gets closer to the substrate. As a result of this, the distance between the parallel plates of the capacitor changes. The capacitance value is consequently a function of the distance between the suspended bridge and the contact below it.

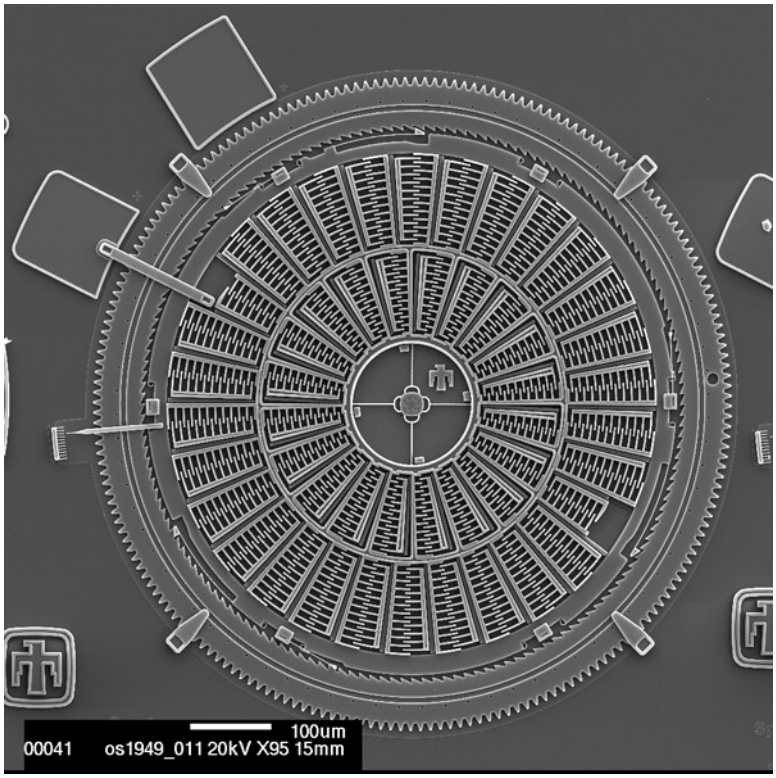

Figure 3.6: Sandia Torsional racheting actuators (TRA) [66]. Courtesy of Sandia National Laboratories, SUMMiT^{TM} Technologies, www.mems.sandia.gov

The last and the least popular RF MEMS/NEMS component class is the RF antennas.

Reconfigurable RF MEMS/NEMS antennas have been reported in the literature [13, 3]. In these proposed designs, the main idea is electrically changing the far field radiation pattern using MEMS/NEMS microactuators. One way to change the radiation pattern is changing the radiation aperture of the antenna using microactuators.

3.2.3 MEMS/NEMS actuation and motion transfer methods

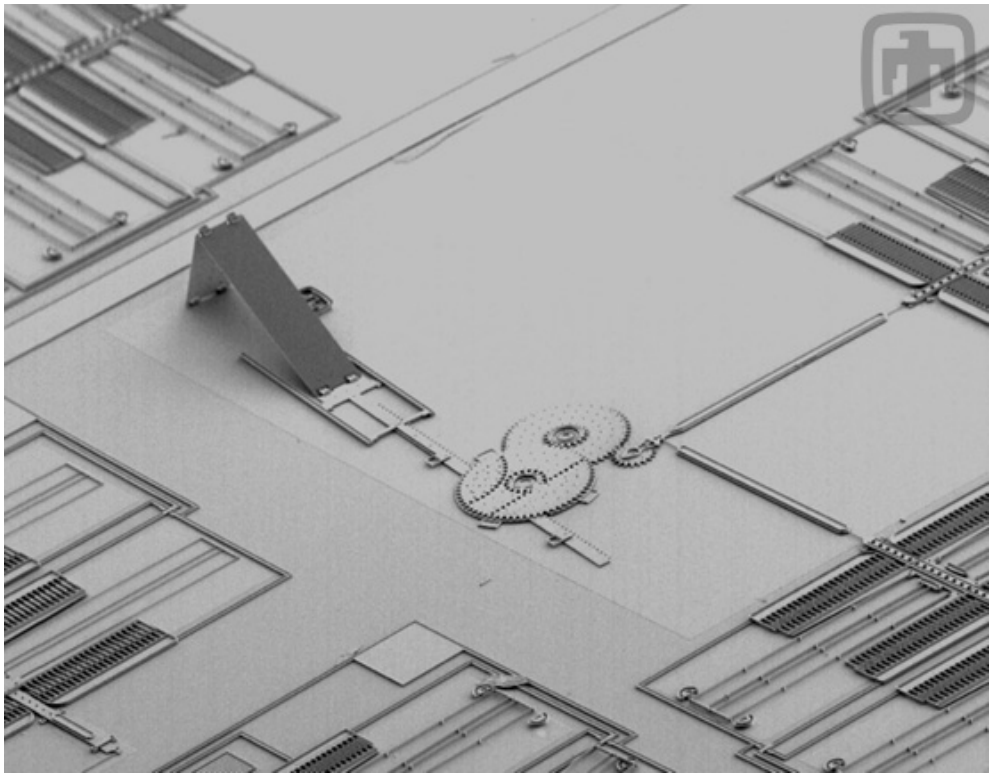

Figure 3.7: Sandia MEMS micromirror device with an electrostatically actuated parallel plate microengine [54]. Courtesy of Sandia National Laboratories, SUMMiT^{TM} Technologies, www.mems.sandia.gov

In this section, actuation mechanisms and motion transfer methods will be briefly described. We will focus on the very probable candidates in these areas that may be applied to realize the proposed structures in this thesis. Consequently, we will focus on the electrostatic actuation for motion creation, and racks and gear trains for motion transfers in the fabricated structure.

Torsional racheting actuators and microengines driven by parallel plate comb drives are

the two main electrostatic actuation mechanisms used in complex MEMS/NEMS devices [66, 54]. In the torsional racheting technique, torsional comb drives are used to generate the motion. This motion is transferred out using rachets and a small gear mechanism. Fig. 3.6 shows an example of this type of an actuator. The second method for actuation, microengine created by parallel plate comb drives is indicated in Fig. 3.7. The distance between the parallel plates of the comb drives is changed electrostatically. This motion drives and rotates the microengine arms, which then creates a rotational motion. In this figure, two of the most common motion transfer methods are also indicated: 1) gear trains 2) linear racks.

3.3 Photonic Crystals

Photonic crystals (PhCs) are periodic structures with different refractive indexed materials. Their importance and indispensability for electromagnetic applications emerge as a result of their ability to confine electromagnetic waves for a certain range of frequencies called photonic band gaps (PBG), which are analogous to forbidden electron energy gaps in semiconductor crystals [5]. At frequencies which remain in the PBG range, there are not any propagating electromagnetic solutions; consequently electromagnetic waves with frequencies in this range cannot exist in these structures. Furthermore, the periodicity and the dimensions of the structure directly affect the properties of the band gap. Ultimately, the band gap property provides PhCs with the ability to control EM-waves. At this point, it is also important to note that because the structures in the periodic lattice of PhCs are typically smaller than the wavelength of the EM wave, traditional diffraction theory fails to predict the interaction. A more rigorous theory is being developed, but for practical problems, numerical simulation using techniques like the finite-difference-time-domain (FDTD) algorithm is one of the most common ways to characterize the time response of the structure to the interrogating EM waves of interest.

Photonic crystal structures can be implemented in 1D, 2D or 3D depending on the dimensions in which a periodicity of different indexed materials is observed. In other words, the number of dimensions in which light confinement can be achieved depends on the struc-

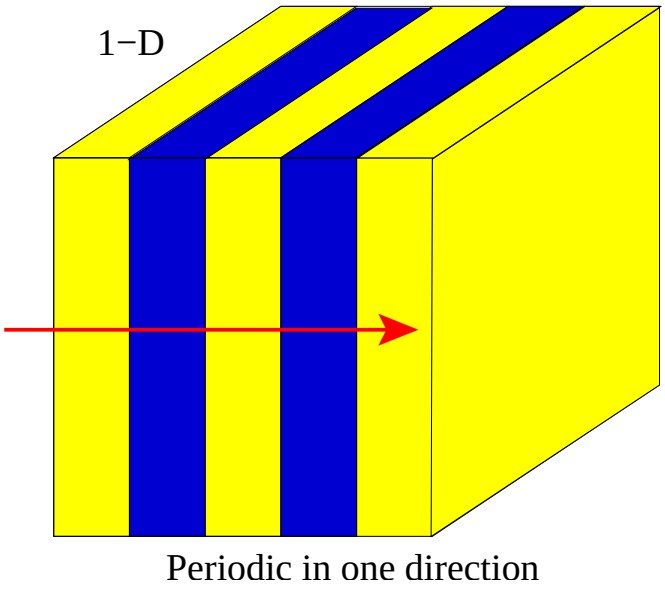

Figure 3.8: 1D PhC structure. The direction of periodicity is indicated with an arrow. Different colors show different dielectric materials with different refractive indices. This structure has the same characteristics with a a classical Bragg mirror because essentially a Bragg mirror is also a 1D PhC.

ture. If an electromagnetic wave, with a frequency in the PBG, impinges on these structures in the direction of periodicity, the structures will behave like a mirror and the light will reflect back. Fig. 3.8, Fig. 3.9, and Fig. 3.10 indicate 1D, 2D, and 3D PhCs respectively. As seen in these figures, in the 1D case, the material indices are periodic in only one direction as shown with the red arrow. In the 2D case however, there are two arrows showing the directions of periodicity, and if a light pulse whose frequency is in the band gap of this structure impinges on this structure in either of these directions, it will be reflected back. The similar case can be observed for the 3D case, with the only difference of periodicity being in three directions.

1D PhC structures are restricted to confine light in only one direction because of their geometry, which definitely decreases their possible applications. 3D PhC structures on the other hand, are very hard to fabricate using conventional fabrication methods, although there is a considerable increase in 3D PhC research. Consequently, this thesis will focus on 2D PhCs.

2D PhC structures, as shown in Fig. 3.9, are periodic in two directions and homogenous

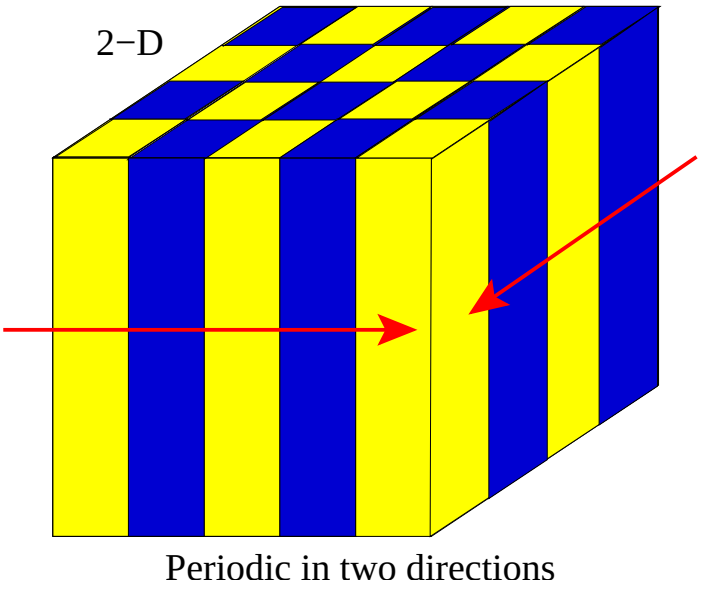

Figure 3.9: 2D PhC structure. The directions of periodicity are indicated with two arrows. Different colors show different dielectric materials with different refractive indices. This time the periodicity is observed in two perpendicular directions, which essentially creates a plane.

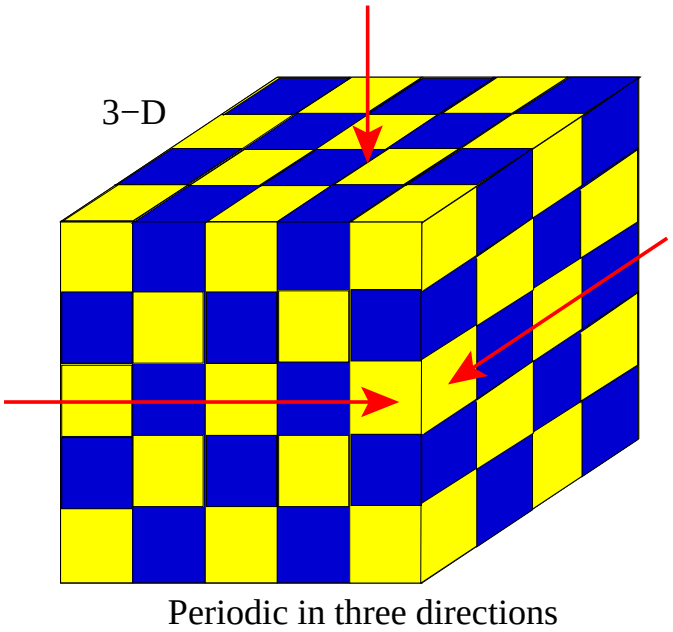

Figure 3.10: 3D PhC structure. The directions of periodicity are indicated with three arrows. Different colors show different dielectric materials with different refractive indices. This time the periodicity is observed in all three perpendicular directions.

in the third, so the photonic band gap appears in the plane of periodicity. Their fabrication process is much easier when compared to 3D PhCs. 2D PhC structures can be realized using various methods, yet the two most commonly researched are "air columns in a dielectric substrate" and "dielectric columns in air." PhCs can also be classified depending on the lattice properties of the periodicity. For example, the PhC structure can be a square lattice or a triangular lattice depending on the required band gap characteristics. The whole photonic band gap characteristics, consequently all functionality of the structure directly depends on these properties. Different dimensionality, material composition, lattice structure, and dimensions (length and width ratios) cause different responses. Following information will be useful to give some insights about these properties.

3.3.1 Air columns in a dielectric substrate in a triangular lattice structure

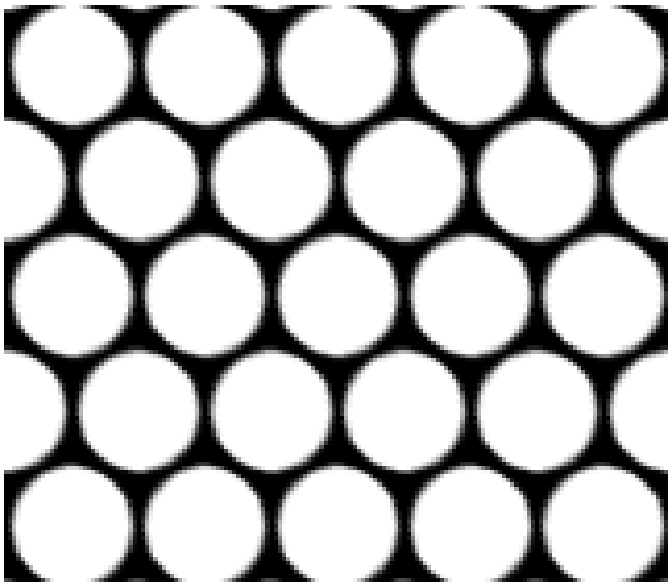

Figure 3.11: PhC configuration with air columns in a dielectric substrate. The structure is in a triangular lattice geometric shape. This figure is created using MIT's Photonic Bandgap tool (MPB), which is a frequency domain solver mostly used for periodic structures such as PhCs [30].

Using air columns in a dielectric substrate is one method that is commonly used in literature. This structure is periodic in two of its axes and homogenous in the third. For certain values of columns spacing, this crystal can have a photonic band gap in the

plane cutting all the air columns. As mentioned previously, inside this frequency range, no extended states are allowed, so the incident light in this plane (regardless of its angle) is reflected. Depending on the periodicity dimensions, there can be total band gaps (TE+TM) for this specific structure. Of course, a more detailed design analysis has to be conducted in order to overlap the band gaps of TE and TM waves. In Fig. 3.11, the top view of this type of a structure is indicated. Also, Fig. 3.12 shows a fabricated version of this PhC type.

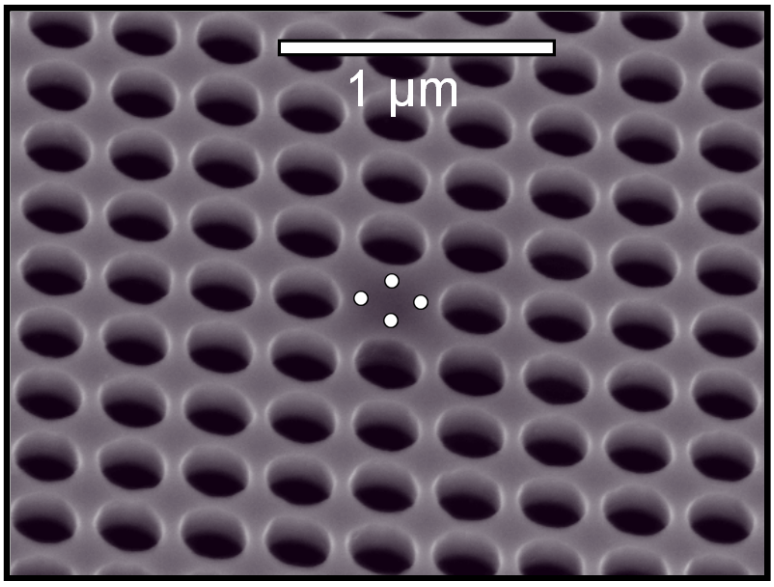

Figure 3.12: Fabricated PhC structure consisting of air columns in a dielectric substrate. In the middle of the structure, a resonant cavity is created by removing some of the air columns. This is a good example of possible applications PhCs can provide when specific defects are intentionally created in them. [26]

When these structures, indicated in Fig. 3.11 and Fig. 3.12, are analyzed in terms of their band gap characteristics and mode shapes, we reach to the following results.

First of all, Fig. 3.13 shows the TM (transverse magnetic) band diagram of this structure. There are two band gaps as indicated in the figure, a small one around $f = 0.8(c/a)$ and a wider one in $f = (0.4 - 0.45)(c/a)$ frequency range. Each line in this figure corresponds to a specific mode as a function of frequency and wave vector (k) direction in the Brillouin zone. The next figure, Fig. 3.14, indicates the TE (transverse electric) band diagram of the same structure. In this case, it is important to note the significantly wide band gap in $f = (0.4 - 0.5)(c/a)$ frequency range. In the case of PhCs consisting of air columns in

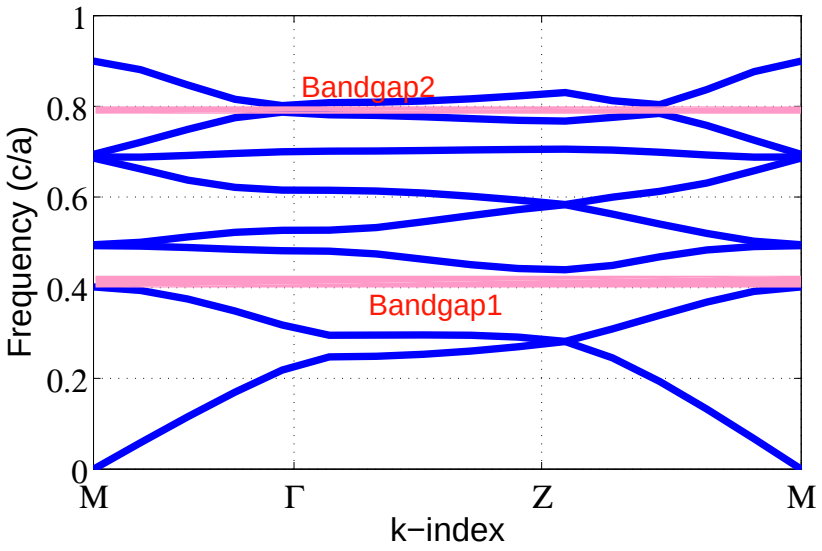

Figure 3.13: TM band diagram for the specific PhC configuration consisting of air columns in dielectric. Each line in the plot indicates a mode that can propagate in the structure, and these modes are plotted as a function of frequency and wave vector (k) direction in the Brillouin zone. There are two main band gaps: first one around $f = 0.8(c/a)$ and a second and wider one in $f = (0.4 - 0.45)(c/a)$ frequency range

a dielectric material, there is a "total band gap" in the frequency range corresponding to $f = (0.4 - 0.45)(c/a)$. "Total band gap" is defined as the frequency range whose band gap characteristics are independent from the polarization of the light pulse. In other words, in this wavelength range, there is a band gap for both TM and TE polarized electromagnetic waves.

Looking at the mode shapes for this specific type of PhC structure is also important. Fig. 3.15 shows two of the modes associated with the air columns in dielectric substrate PhC configuration, one low order and one higher order mode. By looking at these figures, it can be observed that modes try to concentrate on high dielectric regions to minimize their frequencies. At the same time, they try to be perpendicular to each other. The band gap phenomenon in PhCs can be very roughly described to be emerging as a result of this process.

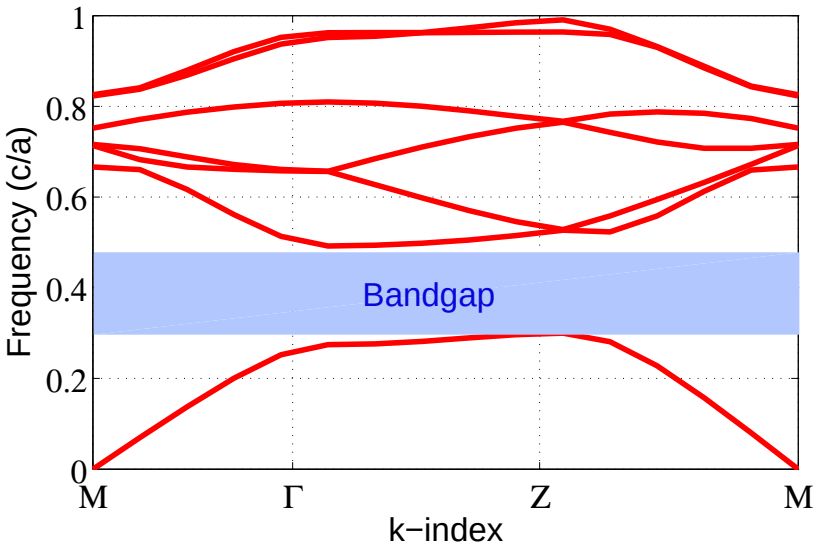

Figure 3.14: TE band diagram for the specific PhC configuration consisting of air columns in dielectric. Each line in the plot indicates a mode that can propagate in the structure, and these modes are plotted as a function of frequency and wave vector (k) direction in the Brillouin zone. The most significant band gap is in $f = (0.4 - 0.45)(c/a)$ frequency range.

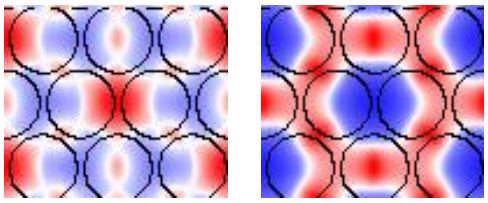

Figure 3.15: Two different mode structures associated with the air columns in dielectric substrate PhC configuration. As can be observed from these figures, modes try to concentrate on high dielectric regions to minimize their frequencies. At the same time they try to be perpendicular to each other. (left) This is one of the low order modes (right) This is a higher order mode.

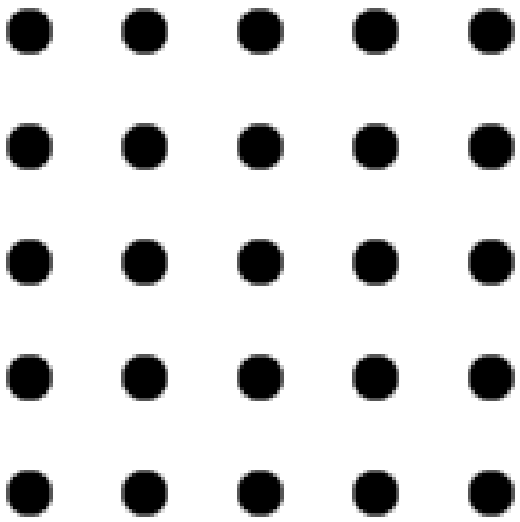

Figure 3.16: PhC configuration with dielectric columns in air. The structure is in a square lattice geometric shape. This figure is also created using MIT's Photonic Bandgap tool (MPB). [30]

3.3.2 Dielectric columns in air in a square lattice structure

Using dielectric columns in air with a square lattice structure is another common method. This structure is periodic in two of its axes and homogenous in the third. For certain values of columns spacing, this crystal can have a photonic band gap in the plane cutting all the rods. As mentioned previously, inside this frequency range, no extended states are allowed, so the incident light in this plane (regardless of its angle) is reflected. In general we see TM band gaps in this type of structures, yet TE band gap doesn't exist or exist in very small frequency ranges. In Fig. 3.16, the top view of this type of a structure is indicated. Also, Fig. 3.17 shows a fabricated version of this PhC type.

When a similar analysis that was conducted in section 3.3.1 is conducted for this type of structures, which are indicated in Fig. 3.16 and Fig. 3.17, the following results can be observed.

First of all, Fig. 3.18 shows the TE (transverse electric) band diagram of this structure. There is almost no band gap as indicated in the figure, except an insignificantly small one around $f = 0.82(c/a)$. Similar to the band diagrams that are discussed previously, each line

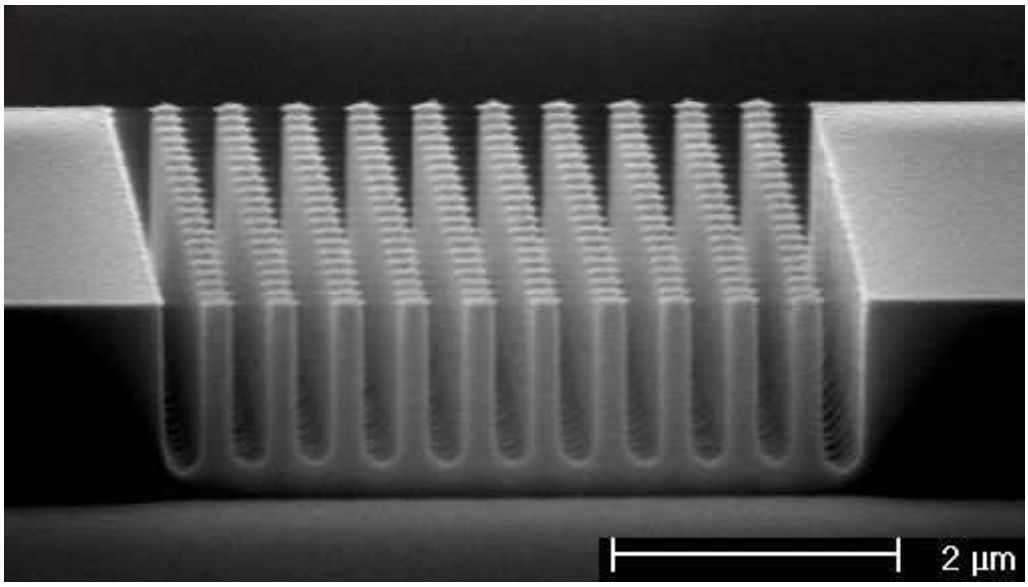

Figure 3.17: Fabricated 2D PhC structure consisting of dielectric columns in air. [15]

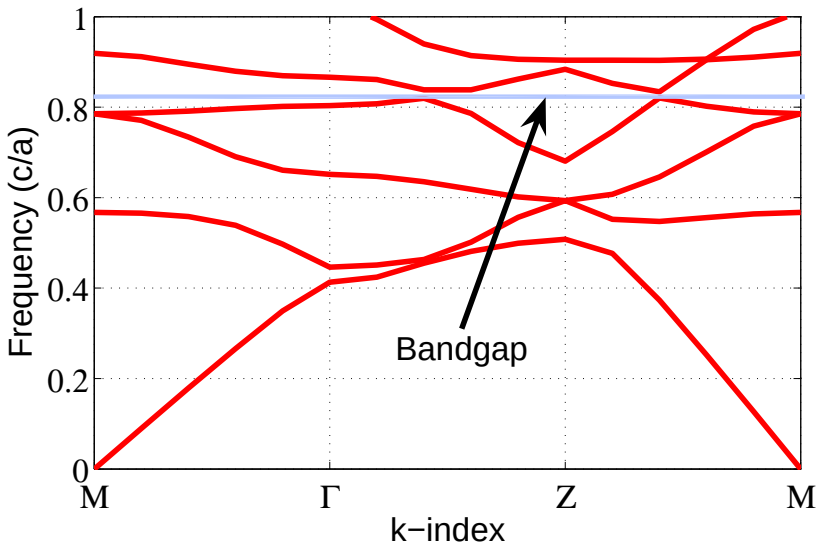

Figure 3.18: TE band diagram for the specific PhC configuration consisting of dielectric columns in air. Each line in the plot indicates a mode that can propagate in the structure, and these modes are plotted as a function of frequency and wave vector (k) direction in the Brillouin zone. There is almost no band gap for TE polarized light except an insignificantly narrow one around $f = 0.82(c/a)$

in this figure corresponds to a specific mode as a function of frequency and wave (k) vector direction in the Brillouin zone. The next figure, Fig. 3.19, indicates the TM (transverse magnetic) band diagram of the same structure. In this case, it is important to note the significantly wide band gap in $f = (0.3 - 0.4)(c/a)$ frequency range. In addition to this, there is another small band gap around $f = 0.75(c/a)$. In the case of PhCs consisting of dielectric columns in air, there is not a "total band gap" in the observed frequency spectrum. Consequently, it can be asserted that for this type of PhCs, TM polarized electromagnetic waves should be preferred in order to get an efficient and reliable band gap.

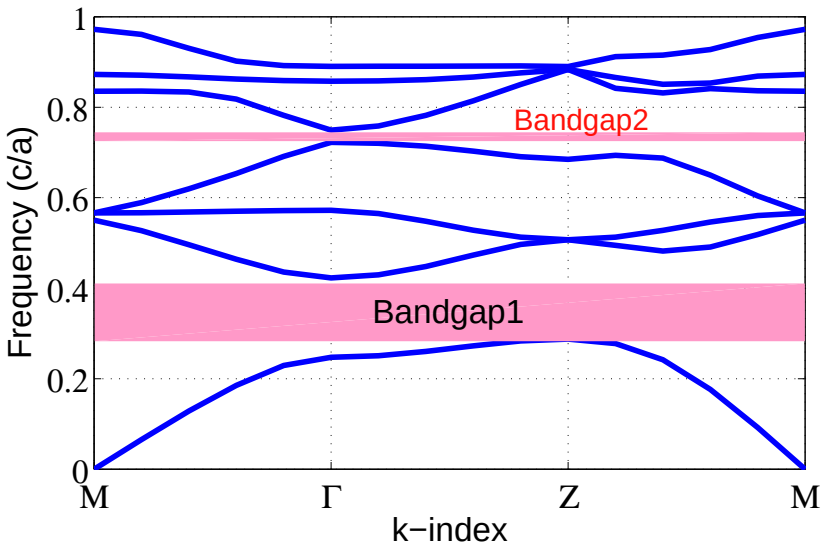

Figure 3.19: TM band diagram for the specific PhC configuration consisting of dielectric columns in air. Each line in the plot indicates a mode that can propagate in the structure, and these modes are plotted as a function of frequency and wave vector (k) direction in the Brillouin zone. There is a significantly wide band gap in $f = (0.3 - 0.4)(c/a)$ frequency range. Also, there is a smaller one around $f = 0.75(c/a)$.

Looking at the mode shapes for this specific type of PhC structure is also important. Fig. 3.20 shows two of the modes associated with the dielectric columns in air PhC configuration, one low order and one higher order mode. By looking at these figures, it is again very clear that modes try to concentrate on high dielectric regions to minimize their frequencies while trying to be perpendicular to each other. Ultimately, this leads to the band gap phenomenon in this type of PhCs, similar to the type described in section 3.3.1.

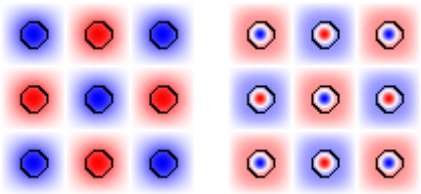

Figure 3.20: Two different mode structures associated with the air columns in dielectric substrate PhC configuration. As can be observed from these figures, modes try to concentrate on high dielectric regions to minimize their frequencies. At the same time they try to be perpendicular to each other. (left) This is one of the low order modes (right) This is a higher order mode.

3.3.3 Line defects and waveguides in 2D PhCs

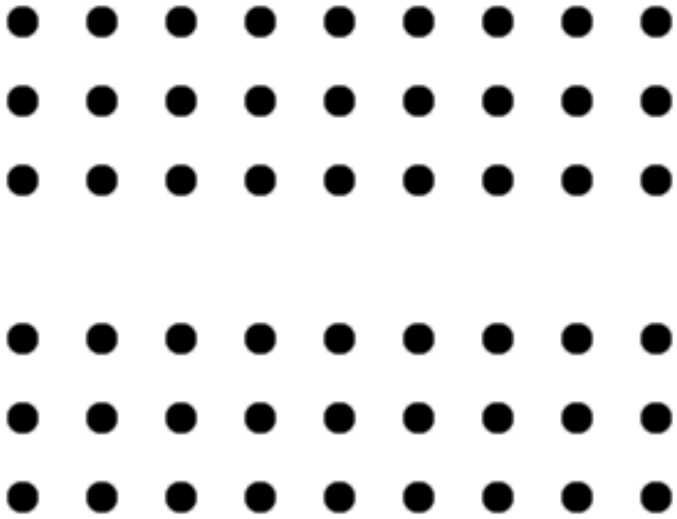

Figure 3.21: Top view of the 2D PhC with an intentionally introduced line defect. The defect is created by removing a row of dielectric rods from its original and perfect configuration, which is a 2D square lattice dielectric rods in air.

As already mentioned, an electromagnetic wave cannot propagate through a PhC if its frequency falls inside the band gap. However, it is possible to excite guided modes inside the band gap by intentionally locating defects in the perfect PhC structure [37]. In this case, propagation ability is activated for certain frequencies in the band gap. If this situation is realized by the insertion of defects along a line in the PhC, then the resulting structure is nothing but a waveguide [38]. The reason is that the light which enters this defect region

can only propagate in the defect direction and it cannot move in any other direction because of the band gap property. Two possible waveguide methodologies are shown in Fig. 3.21 and Fig. 3.22. The first waveguide is created by removing a row of dielectric rods from the perfect 2D PhC structure. Consequently, light can only propagate on this line defect, which is basically a waveguide. Similar situation holds for the second guide except it is implemented by removing a row of air holes. In both waveguides, light can only propagate in the waveguide, and cannot scatter in any other direction by means of the band gap property.

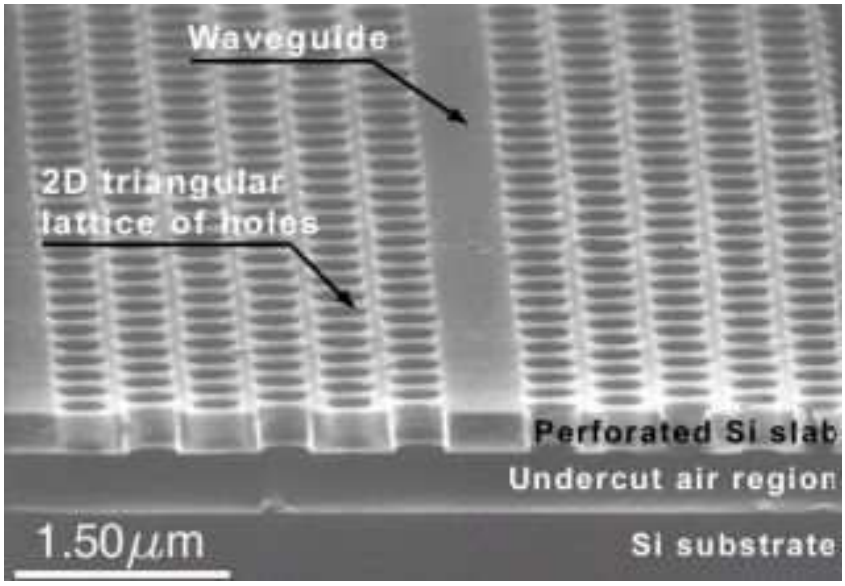

Figure 3.22: Fabricated 2D triangular lattice PhC structure with a built in waveguide. The line defect is created by removing a row of air holes from the original and perfectly periodic configuration, which is a 2D triangular lattice air columns in a dielectric substrate. [57]

Fig. 3.23 shows one of the localized defect modes for the TM polarized electromagnetic waves for the structure indicated in Fig. 3.21. In its perfect configuration (without the waveguide), this PhC structure had a band gap around $f = (0.3 - 0.4)(c/a)$ frequency range as indicated in Fig. 3.19. However, when the line defect is introduced, a localized defect mode is introduced into the band gap, which is indicated in Fig. 3.23. And this is the mode that can now propagate through the waveguide, and the shape of this mode is shown in Fig. 3.24.

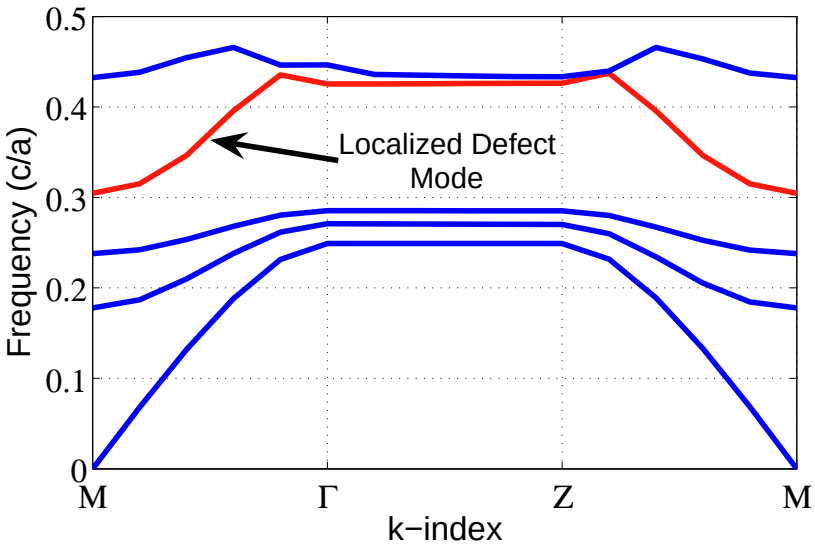

Figure 3.23: Localized defect mode for the TM polarized electromagnetic waves for the structure shown in Fig. 3.21 is indicated. In its perfect configuration, there is a band gap around $f = 0.3 - 0.4(c/a)$. However, line defect created by removing a row of dielectric columns creates a defect mode in this band gap now.

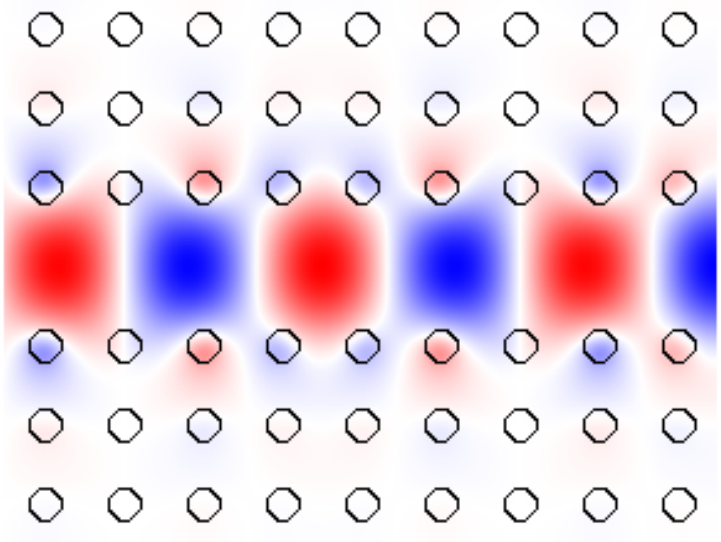

Figure 3.24: The shape of the localized mode indicated in Fig. 3.23 is shown. As can be observed from the figure, the light is only propagating in the waveguide, and does not scatter to any other direction because of the band gap property of the PhC.

By using the PBG effect of PhCs, it is possible to create a completely new class of electromagnetic waveguides [10]. First of all, by adjusting the symmetry and dimensions of the structure, it is possible to guide a large interval of frequencies, including visible light. Furthermore, when PBG effect compared to total internal reflection (TIR) is used, it is possible to create lossless sharply bended (like 90 degrees) waveguides. Lossless sharp bends and branches in PhC waveguides have been demonstrated in literature [57, 5, 35]. In other words, lossless waveguides with bend and branch curvature radiuses on the order of light wavelength are possible to be implemented using PhC waveguides without being dependent on TIR methodology [35]. An example of this type of a structure is shown in Fig. 3.25. In this figure, a sharply bending waveguide, created by removing some of the dielectric rods, is indicated.

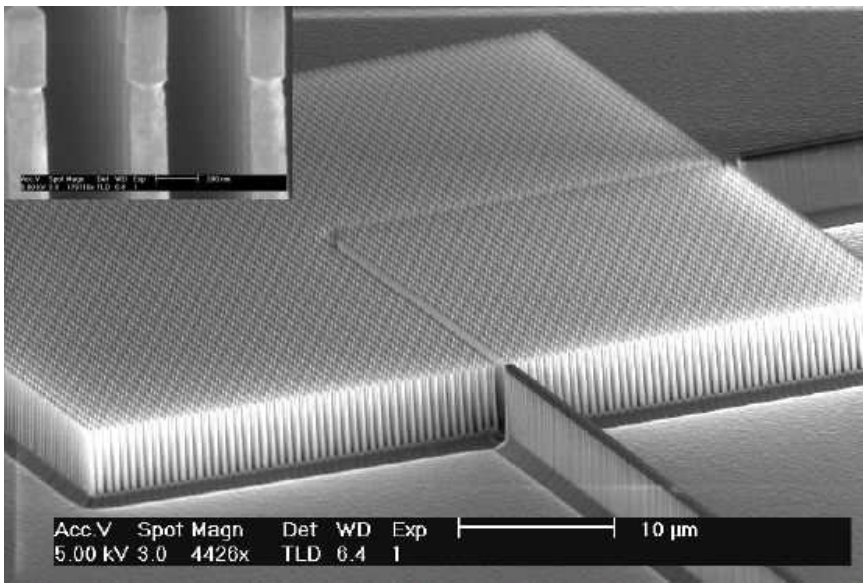

Figure 3.25: A 2D PhC waveguide with a 90 degree bend is fabricated. The line defects are created by removing a row and a column of dielectric rods from the perfectly periodic configuration. [15]

As explained in this section, PhCs have very unusual and interesting characteristics. As a result, since their recognition in 1987 by Yablonovitch[74], there has been exponentially increasing interest in photonic crystal devices. For example, devices have been demonstrated for a wide number of interesting and innovative applications such as a nearly

thresholdless micro-laser with very high modulation bandwidth[20, 39], a highly linear fiber, a highly nonlinear fiber, an optical add/drop filter appropriate for next-generation dense-wavelength-division-multiplexing (DWDM) channel spacings, and even an extremely efficient light source[19].

Fabrication difficulties emerge as one of the most crucial problems related to PhCs and PhC waveguides. Especially, large index contrasts between the constituting materials as well as a very precise material morphology with a periodicity on the scale of the optical wavelength are hard to achieve [5]. This will become more clear when we think that the band gap properties of the PhC structures is totally affected by the dimensions of the periodicity, and small unexpected distortions at the fabrication level might change the expected result completely. For instance, a frequency, which normally would fall in the band gap and would not be able to propagate, can pass through the PhC structure because of the problems at the fabrication process that distorts the periodicity in very small scales. Also, another major problem is achieving good confinement in the third dimension [10]. In order to solve this problem, 3D PhC structures are being researched and analyzed, yet it still needs more time because three-dimensional photonic crystals for visible light could have been successfully fabricated only within the past year or two [38].

3.4 Proposed PhC/NEMS Structures

As explained in the previous sections, both PhCs and MEMS/NEMS structures lead to very novel applications. However, a structure that is a composition of PhCs and MEMS/NEMS would provide much more novel and revolutionary results and applications. The main reason behind this novelty is the capability of manipulating the unusual optical characteristics of PhCs (both dispersion and band gap) using tunability of nanoscale MEMS/NEMS devices. The motion (uniform or non-uniform) provided by the MEMS/NEMS devices affect the band structure of the PhCs and cause very interesting results. Consequently, in this thesis, the main focus of discussion will be on structures which are created by integrating PhCs and MEMS/NEMS. A good deal of work is already being actively pursued internationally to improve the theory and understanding of the nanoscale

interaction between PhCs and MEMS/NEMS [21, 48, 16, 44]. However, it can be asserted that this research needs more time to become mature and create commercially available products.

Two main broad classes of devices are proposed as a result of the integration of PhCs with MEMS/NEMS structures: 1) Dynamically reconfigurable optical ICs and 2) Nonlinear optical devices, "wavelength converters" to be more specific. In the first part of this section, proposed reconfigurable optical ICs will be described and detailed information about the PhC-NEMS mechanism behind them will be given. In the second part, integrated PhC-NEMS structures capable of providing wavelength conversion will be analyzed in detail.

3.4.1 Reconfigurable Optical Integrated Circuits

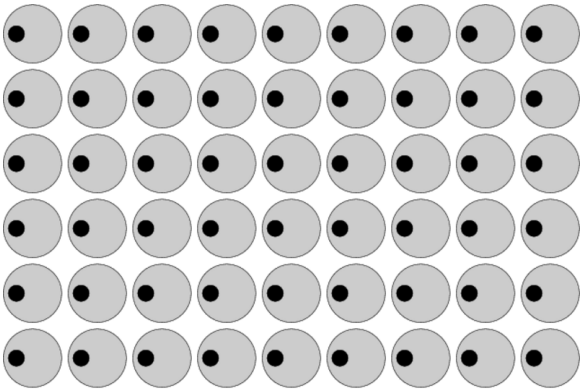

Figure 3.26: 2-D photonic crystal with integrated NEMS in default configuration with no defects. The light gray circles represent the NEMS discs that can be rotated individually.

For the realization of reconfigurable optical devices, the following architecture is suggested. The dielectric rods in a 2D square lattice PhC shown in Fig. 3.16 and Fig. 3.17 are fabricated on top of an array of NEMS structures that are capable of rotation. On each rotating disc, there is a dielectric rod etched close to the edge of the disc. The diameter of each disk is slightly smaller ($0.8a$) than the lattice constant of the PhC structure (a), so that when the disc rotates, the center of the dielectric rod on it traces out a circle with a diameter of $0.5a$. Each NEMS disk is accessible individually, and this creates an important amount of flexibility in the device structure. The geometric position of the PhC rods can be

manipulated using the NEMS rings, and as a result, PhC above the rings can be configured to be in any required, specific shape.

Fig. 3.26 shows a 6×9 array of the NEMS discs and rods in their default position. As can be observed in this figure the rod structure above the rotating NEMS rings appears to be a periodic 2D square lattice PhC, and hence has the associated forbidden band gap and dispersion properties. However, by rotating some of the NEMS rings, (and dielectric rods above them) different functionalities can be produced. Also, all of these possible functionalities can be implemented in a single chip, and this could be a revolutionary multipurpose-nanophotonic integrated circuit.

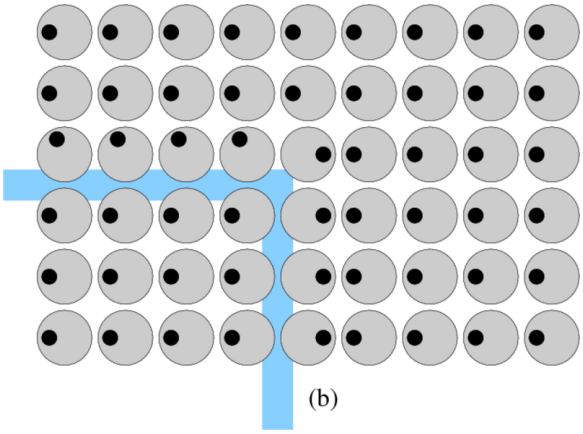

Figure 3.27: 2D PhC NEMS structure in a line defect configuration

The first possible functionality of this type of a structure is as a channel waveguide. As indicated in Fig. 3.27, by rotating some of the dielectric rods, line defects can be created in the PhC structure. As mentioned in section 3.3, this allows certain modes, with frequencies in the band gap range, to propagate in the PhC without any losses and dispersion. Since the waveguides can be created in a reconfigurable manner, any port in the chip can be connected to any other port. In addition, different connections in the chip can be done simultaneously, because each rod is individually addressible.

The second potential functionality is as the beam splitter/combiner. After some of the rods in the structure are configured to create a line defect, an optical beam can propagate in this waveguide. If the suitable arrangement of the rod positions is accomplished as shown

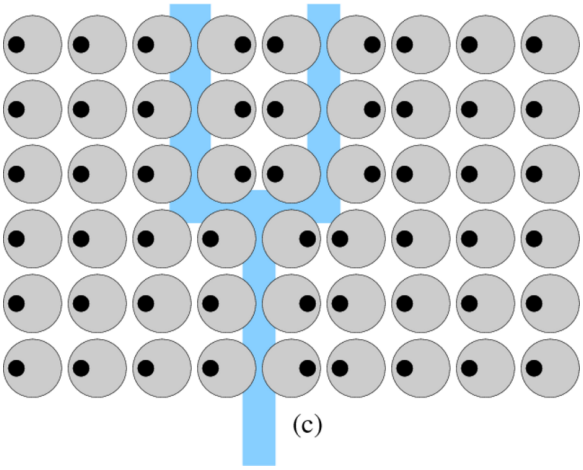

Figure 3.28: 2D PhC NEMS structure in a beam splitter configuration

in Fig. 3.28, the single beam can be split into any required amount of separate beams. If the process is reversed in a similar manner, beam combining can also be achieved in the device. Again these two opposite operations can happen at the same time at different segments of the chip which adds more to the flexibility of the proposed structure.

In addition to simple beam splitting/combining operations, more complicated tasks can easily be achieved. For example, Fig. 3.29 shows the configuration of rods in the proposed structure to realize a Mach-Zehnder interferometer. Basically, after a beam is split into two separate beams, phase in one of the branches can be modulated by small deviations in the position of the NEM cell marked "A". Depending on the amount of phase shift, the beams can interfere destructively or constructively.

3.4.2 Nonlinear Optical Devices

Another class of devices with very interesting characteristics can be created if the optical waves get into interaction with moving structures, such as NEMS. When the light interacts with static structures, the modes and interaction coefficients remain unchanged. However, when there is an interaction with moving structures, the characteristics of the optical wave become time-variant. In addition to this, very important phenomenon such as wavelength conversion as a result of the Doppler effect is possible.

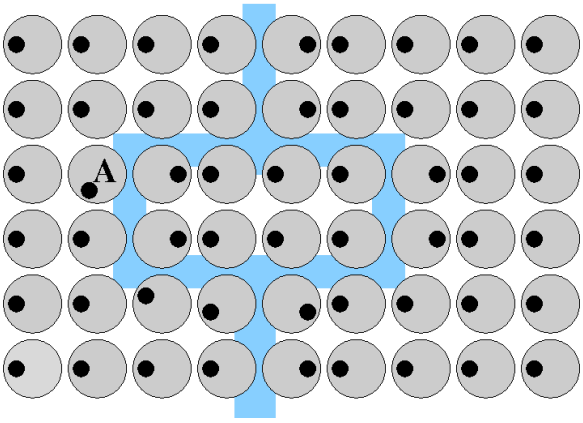

Figure 3.29: 2-D photonic crystal based Mach-Zehnder interferometer. The NEMS marked "A" can be used to modulate the path length and hence the phase of the input.

The Doppler effect can be described as a change in the frequency of a wave when the source of the wave or the observer are moving with respect to each other. From a physical point of, when the source of an optical wave with a frequency of f_0 is moving towards an observer with a speed of v, then the speed of light emitted by this source would be observed to be $c+v$, where c is the speed of light in free space, by the observer. However, from a relativistic point of view, this is not possible because the speed of light is constant at c in all frames of reference. Consequently, the effect of v is converted into a frequency increase, and the frequency of the light observed by the observer becomes $f=f_0+f'$, where f' is the Doppler shift associated with the frequency of the optical wave. f' is a function of the speed of the source. The reverse case applies if the source is moving away from the observer, and essentially observer sees the optical wave with a frequency of $f=f_0-f'$. This situation is indicated in Fig. 3.30. In this case, the source is moving towards left, and as shown in the figure, the peaks of the periodic optical wave come closer on the left hand side while the peaks on the right gets further away from each other. In other words, frequency on the left hand side is increased while the frequency on the right hand side is decreased due to the Doppler effect.

In this section, two different structures will be proposed both of which are composed of integrated PhC-NEMS structures and are capable of all optical wavelength conversion: 1) Rods on counter-rotating NEMS rings 2) Sliding rods on an "L" shaped NEMS track.

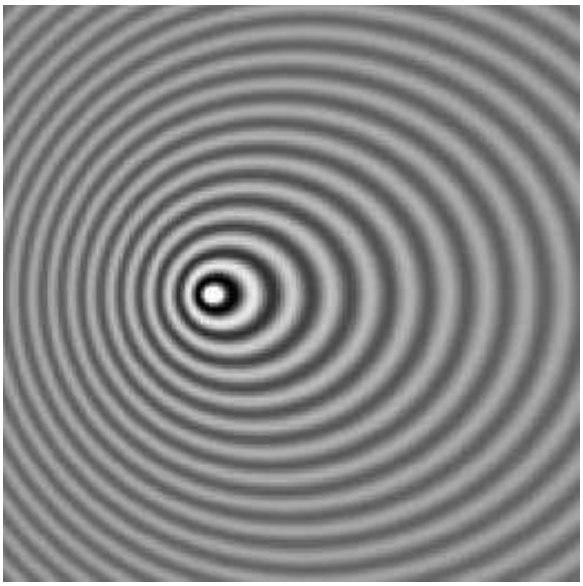

Figure 3.30: The source is moving towards left. The peaks of the periodic optical wave come closer on the left hand side while the peaks on the right gets further away from each other. In other words, frequency on the left hand side is increased while the frequency on the right hand side is decreased due to Doppler effect. [70]

In both of these structures, the input optical wave to the PhC-NEMS structure will be confined using PhC band gap property, and will gain a frequency shift as a result of the Doppler shift created by the moving NEMS structures.

The first structure consists of two main parts. The first one is a 2D square lattice PhC structure with a line defect (a waveguide) passing through it. The second part is a pair of counter-rotating NEMS rings, on top of which some dielectric rods are etched. Initially, these rotating rods align and complete the periodic 2D square lattice PhC structure above the rings as indicated in Fig. 3.31. A side view of the same structure is shown in Fig. 3.32. When the optical beam is propagating through the waveguide, the NEMS rings start to rotate in opposite directions, and when the rotating rods on these rings close the waveguide, the structure will temporarily confine light in a cavity whose dimensions are on the order of the light's wavelength. The light trapped in the cavity resonates between the collapsing (moving) rods, and gain an enormous Doppler shift. When the rings and rotating rods reopen the waveguide, the wavelength converted optical wave continues to propagate on the waveguide. The Doppler shift of moving PhC-like structures can have some very unusual

behavior. Very recently, Doppler shifts of 60 THz have been predicted due to shock waves in PhCs [51, 52]. This extraordinary amount of frequency shift is entirely due to unusual band gap properties of the PhCs.

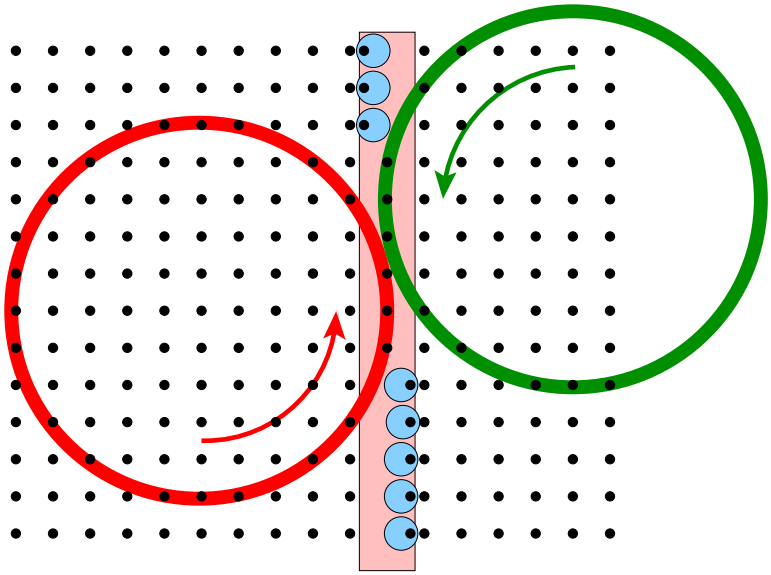

Figure 3.31: Top view of the 2-D nonlinear photonic crystal MEMS/NEMS structure based on counter-rotating rings. After the waveguide is created and the light is coupled into this waveguide, the NEMS rings start to rotate in the directions indicated in the figure. Initially, the waveguide is open, and after a while, NEMS rods on the waveguide close and trap the light in a cavity.

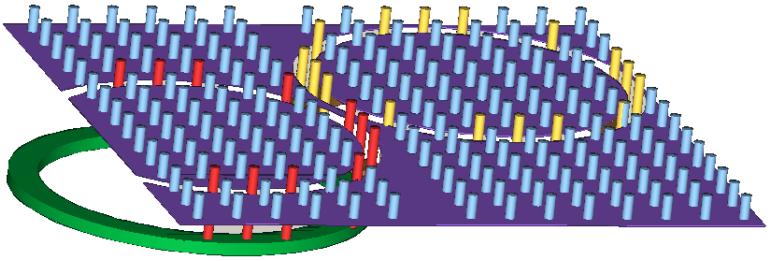

Figure 3.32: CAD view of the structure indicated in Fig. 3.31

The second structure is very similar to the first one, yet the moving rods are implemented in a different manner using a different NEMS structure. This structure also consists of two main parts. The first one, square lattice 2D PhC with a built in waveguide, is the same as the former structure. However, this time the moving rods are etched on a NEMS device

that follows an "L" shaped track. The structure is indicated in Fig. 3.33 and Fig. 3.34. The rods slide out of the periodic 2D PhC structure when the optical wave is propagating through the waveguide. As the moving rods are moved close to each other, similar to the first structure, the moving rods complete the periodic PhC structure, and light is trapped in the very small sized cavity. As the cavity collapses, the trapped light gains a huge Doppler frequency shift. When the moving rods slide out of the waveguide through the static PhC rods, the wavelength converted optical beam continues to propagate through the waveguide, but with its new frequency.

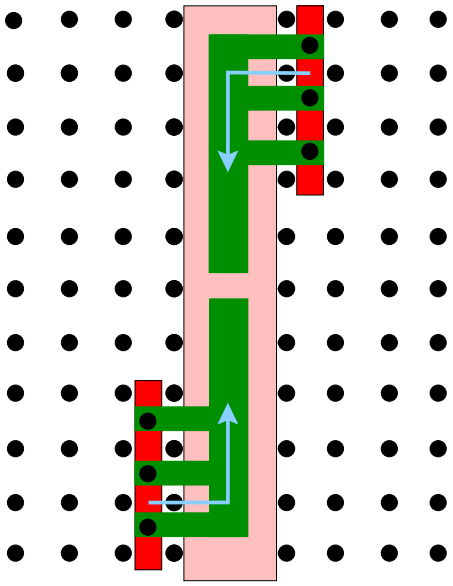

Figure 3.33: Top view of the second 2-D nonlinear photonic crystal MEMS/NEMS structure. The idea of the operation is very similar to the first one indicated in Fig. 3.31 but this time the motion is based on sliding MEMS/NEMS structures on an "L" shaped track.

At this point, it is important to note the reason of this high amount of Doppler shift occurring in both of these structures. When the light is temporarily trapped in the cavity, since it travels many magnitudes of order faster than the speed of the dielectric rods (NEMS devices), it will effectively bounce millions of times off of the two moving mirror-like PhC surfaces. Each time it will gain a small amount of Doppler shift but these frequency shifts accumulate and create an enormous Doppler shift. Also, if desired the speed of the moving rods in each case can be controlled to provide small or large frequency changes. Furthermore,

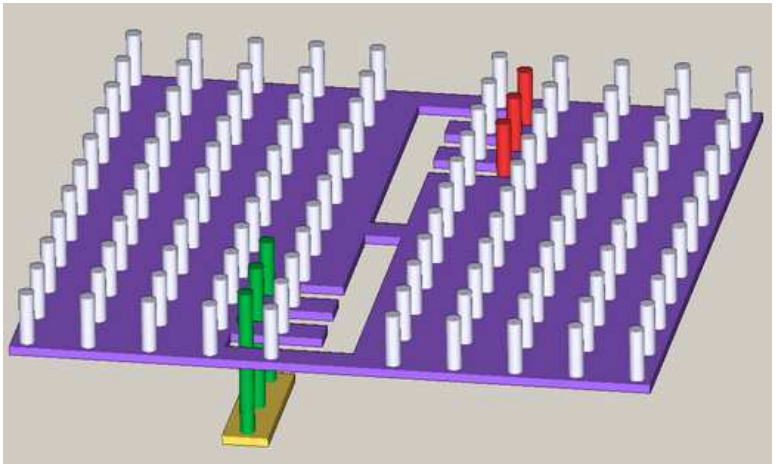

Figure 3.34: CAD view of the structure indicated in Fig. 3.33

if the direction of the movement in each case is reversed (away from each other in the cavity), the Doppler effect will result in a down conversion which is subject to similar limits as the up conversion.

The frequency conversion that occur in the collapsing cavities of these structures can also be explained using the adiabatic theorem. Adiabatic theorem in quantum theory mainly refers to the evolution of systems that have very slowly changing Hamiltonians (H). The theorem roughly asserts that "if a state is an instantaneous eigenstate of a sufficiently slowly varying H at one time then it will remain an eigenstate at later times, while its eigenenergy evolves continuously" [56]. This idea can also be applied to our case where the motion of the side walls of the created cavity cause a very slowly varying Hamiltonian in the system. Initially trapped mode in the cavity has the initial frequency. As the side walls collapse (with a velocity much smaller than the speed of light), the energy in this mode is transferred to another mode which has a different frequency. However, since the transition is very slow, the new mode can still exist in the cavity without escaping. This process explains the wavelength conversion that we expect to see in a more accurate and intiutive way.

3.5 Proposed Fabrication Schemes

In this section, the proposed structures are discussed from the perspective of possible fabrication methodologies [1]. We begin by reviewing some of the important fabrication methods used in the realization of current IC, PhC and MEMS/NEMS structures. These specifically examined fabrication methods are also related to the methods found in the contemporary literature. Then, we explain the general mechanism and operation of each proposed structure. Next, we propose a possible fabrication scheme for each structure and give details of the process steps.

3.5.1 PhCs and MEMS/NEMS Fabrication Technology Review

After an IC is designed and its correct functionality is proven using computerized simulation tools (if available), the next step is to fabricate it. The fabrication technology has a great pace of advancement and has become very mature especially in the last years. Very complicated integrated circuits with billions of transistors or MEMS/NEMS components can now be manufactured very easily and efficiently. In this subsection, current status of the fabrication technology will be provided before analyzing the proposed PhC-NEMS structures from a fabrication and realization point of view. In the first part, popular fabrication processes will be described and analyzed in detail. In the second part, MEMS/NEMS specific fabrication issues will be examined.

Pattern transfer is the first step in the fabrication process. It is mainly composed of lithography and etching. Lithography is the process of transferring an image of the structure onto the substrate. Two of the most popular lithography techniques are electron-beam (e-beam) lithography and standard photolithography.

In the e-beam lithography, the image of the designed structure is transferred onto the wafer using an electron gun. The electrons are sent to the wafer in a specific configuration which represent the shape of the proposed structure. This is a direct write technique and consequently does not use any masks, which is an indispensable requirement for standard lithography. The main advantage of the e-beam lithography is that it can reach to very high resolutions on the order of $10 - 20$ nm. The main disadvantage of this technique is

the low processing speed which is a direct result of the fact that this is a series lithography mechanism. In other words, electrons draw the image of the structure onto the wafer grid by grid. This leads to a low throughput. Ultimately, this technique is hard to become commercial, and it is usually used for research and development purposes.

The standard photolithography on the other hand is a much faster method because it works in parallel. In other words, the image of the whole structure is written onto the substrate at once. Since it has a very high throughput, this method is very highly commercialized. Standard photolithography uses masks to transfer the specific shape of the design onto the image. The main disadvantage of this technique is that the possible resolution is limited to 100 nm. Also, since masks are being used, alignment issues might occur and make the process more difficult to deal with.

Among these two lithography choices, e-beam lithography is an excellent candidate for PhC structures [23, 27]. It should also be noted that there are also some PhC structures which use a two-step hybrid method of multiple exposures (interferometric patterning) and direct write [46]. This is a lower cost and faster method. For our candidate designs we will consider standard photolithography techniques for the rotating rings, sliding plates and rotation mechanisms as discussed in reference [62].

After the image of the structure is transferred onto the substrate using lithography, the structure is actually created using etching. Two most popular etching methods are Reactive Ion Etching (RIE) and Wet (Chemical) Etching.

Reactive ion etching (RIE) is one of the most popular techniques used in the literature [73, 76]. In the RIE, ions are replaced between two oppositely charged parallel plates and are accelerated towards the surface of the wafer, which is replaced on one of the plates. When the ions hit the surface of the wafer, they actually etch the substrate and shape it in the desired manner. Etching conditions depend on parameters such as pressure and radio frequency (RF) power. This is a very anisotropic process with very perpendicular side walls, and very high aspect ratios are possible if this method is used in the etching step. Also, it is very highly selective in terms of deciding which materials need to be etched and which ones should not be etched. Another advantage of this technique is the poor surface roughness at the etched surface. Consequently, RIE emerges to be the most appropriate etching choice

for the proposed structures. The main disadvantage in this method is the residual damage which occurs because the accelerated ions are hitting the surface of the wafer with very high velocities.

Wet etching on the other hand is a chemical process. Basically, wafer is put into a suitable chemical solvent which etches away the required sections of the wafer. This is a very highly selective process similar to RIE. The main disadvantage of this technique is its isotropic characteristic at the side walls. Side walls are usually not in perpendicular shape because in this method the process control is poor and this leads to some unwanted extra parts of the substrate being etched away too. Another disadvantage of the method is the surface roughness at the side walls of the etched layer.

While the pattern transfer steps are being implemented in the fabrication of an integrated circuit, if a new layer of material is needed to be covered on the wafer, a deposition process is required. There are two main and popular deposition processes available in today's fabrication technology: Physical Vapour Deposition (PVD) and Chemical Vapour Deposition (CVD).

In the PVD, the material that we want to deposit on top of the wafer is put in a crucible and evaporated. The evaporated material will climb up and stick to the surface of the wafer that is attached to the ceiling of the system. This is mainly a physical method and chemical reactions do not occur in PVD. This technique is usually used for metal depositions and it is a lower quality deposition technique when compared to CVD. Consequently, it has a poor step coverage and the deposited layers using PVD are not as uniform as layers deposited using CVD.

CVD on the other hand is a totally chemical process. The material that will be deposited on the wafer is transformed into gas form and sent through the wafers in a closed system. As a result of the chemical reactions occurring between the wafers and this gas, deposition is realized. Since this is a chemical process, it is totally dependent on the temperature and pressure. This is a very highly uniform process when compared to PVD. It also provides a better step coverage. Consequently, CVD is mostly preferred over PVD if the uniformity is a very critical criteria in the structure that is being fabricated. Low pressure chemical vapor deposition (LPCVD) is a method of CVD which provides better uniformity on the

deposited layer than CVD. Plasma-enhanced CVD is another method in which it is possible to deposit thin films at lower temperatures. One of these methods, or maybe both of them, can be applicable for the proposed designs.

At this point it is also important to note that when the deposited layer is not uniform enough for the application the fabricated device will be used for, a separate technique is used in order to reach to higher uniformity levels. This method is name Chemical Mechanical Polishing (CMP). Basically, in CMP, the surface of the deposited layer is chemically and mechanically polished using special machines.

All of these process steps are implemented on top of a substrate. Substrate choice emerges to be another essential criteria in the performance of the fabricated device. When the optical and MEMS/NEMS devices are concerned, there are three major possibilities for the substrate: Silicon, Galium Arsenide (GaAs) and Silicon-on-insulator (SOI). Silicon substrates are more common and mature when compared to the others. It has a relatively lower cost and simpler processing. Consequently, silicon is the more appropriate choice for most of the MEMS/NEMS devices. Second possible substrate choice is the GaAs. It is usually used for high speed and high frequency applications such as satellite communications, radar systems and mobile phones. The disadvantage associated with this choice is that it is usually very expensive and has a very complicated process. The third and the last possible choice is the SOI. In some applications, SOI substrates are used for their higher quality mechanical characteristics. However, it is not very common when compared to the first two substrate choices.

PhC structures usually use Gallium Arsenide (GaAs) due to its more appropriate optical properties. GaAs has a high dielectric constant, yielding a high refractive index difference from air. References [34, 29] refer to experimental PhC structures consisting of GaAs dielectric rods on a GaAs substrate. GaAs is a more difficult and less mature process than Silicon (Si) which makes it less convenient to use for the proposed designs. Because Si processing is behind the micro-chip revolution, it has evolved relatively quickly into a much more practical, cost efficient, and well-developed technology. References [31, 67] discuss PhC structures built using Si substrates and dielectric rods. Our prototype designs will be centered around Si for the reasons just mentioned. In addition, because we integrate

rotating and sliding micro-machines into the design, we will use polysilicon surface micro-machining [62] in order to produce the composite device on a single wafer.

Another key specification of the fabrication process is the minimum feature size. While the literature search related to PhC fabrication indicates that a minimum feature size of 100 nm is possible using modern fabrication methods such as e-beam lithography [49, 46], the integration of the MEMS structure will necessitate a larger minimum feature size on the order of 1 μm.

After reviewing the most popular fabrication methods used in today's IC technology in the first part, in the second part of this subsection, MEMS/NEMS specific fabrication issues will be described and discussed. All of the methods mentioned in the first part can also be applied when fabricating MEMS/NEMS structures. However, there are two main techniques that are specific to MEMS/NEMS structures: Surface Micromachining and Bulk Micromachining.

In the surface micromachining, the MEMS/NEMS structures are built on the deposited thin film layers. Sacrificial layers, which constitute a crucial part of surface micromachining, are used temporarily in order to create suspending structures and gaps in the device. If in the surface micromachining, a very high aspect ratio is required, then a special technique named LIGA process can be used. LIGA is the german acronym for lithography-electroplating-molding. Cantilever beam RF switches and resonators, gear trains, micromirror arrays, and microengines are some of the example applications that are fabricated using surface micromachining. We will consider the use of surface micro-machining and sacrificial layers to produce the suspended and rotating structures for our candidate designs. Also, it is essential to note that to get suspending or rotating structures, a highly selective HCl/HF (depending on the sacrificial material) acid etch is used [23, 76].

The second MEMS/NEMS specific fabrication issue is the bulk micromachining. In the bulk micromachining, bulk itself is etched and shaped in order to create the MEMS/NEMS device. In other words, MEMS/NEMS structures are created in the substrate. Diaphram pressure sensors, membranes, and accelerometers are some of the applications fabricated using bulk micromachining.

For actuation of both proposed structures, rotation of the rotating disk in the first

proposed structure, and "L" shaped sliding of the NEMS plates in the second proposed structure, approaches such as electrostatic comb-drive actuators [62] or torsional ratcheting actuators [66] can be used. This motion can be transferred to the rotating disk and sliding plates using micro-gears. Rotational micro-gears are actuated by the micro-engines. In the case of the rotating rings structure, these micro-gears transfer this motion to the rotating rings using a standard gear mechanism. In the case of "L" shaped sliding plates, two racks connected between transmissions and the sliding plates will transfer the motion of the microengines to the NEMS plates of the proposed structure.

3.5.2 Fabrication issues of the proposed structures

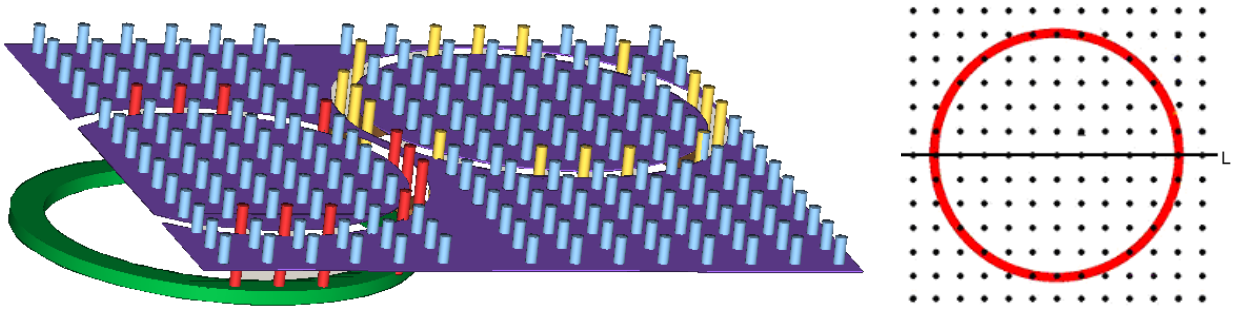

Figure 3.35: (left) Side view of ring portion of proposed prototype 2-D photonic crystal with integrated MEMS. The red and yellow rods are attached to the rotating ring underneath. The remaining rods are stationary and spaced on a square grid of edge length a. (right) Top view of ring portion of proposed structure. The photonic crystal rods that are on the circle are attached to the rotating ring fabricated below the 2D photonic crystal structure.

Fig. 3.35 (left) illustrates the proposed rotating ring structure. It is composed of two main parts. The top of the device is a two-dimensional (2D) PhC consisting of Silicon (Si) rods in air. The rods are spaced on a square lattice of edge length a. The novel feature in this design consists primarily of the bottom portion of the device which is a rotating ring that is attached to the PhC rods that lie directly above the ring. Fig. 3.35 (right) shows the top view of the ring where the rods that are part of the ring are clearly distinguished from the other stationary rods. It is also important to note the distance between the PhC layer and the substrate on which the rings are built. This parameter does not affect the theoretical device performance, but it does strongly impact the feasibility of fabrication.

This distance should be as small as possible in order to decrease the aspect ratio (which is the height over width ratio for a fabricated structure) for the longer rotating rods. As the aspect ratio increases, fabrication becomes increasingly more difficult.

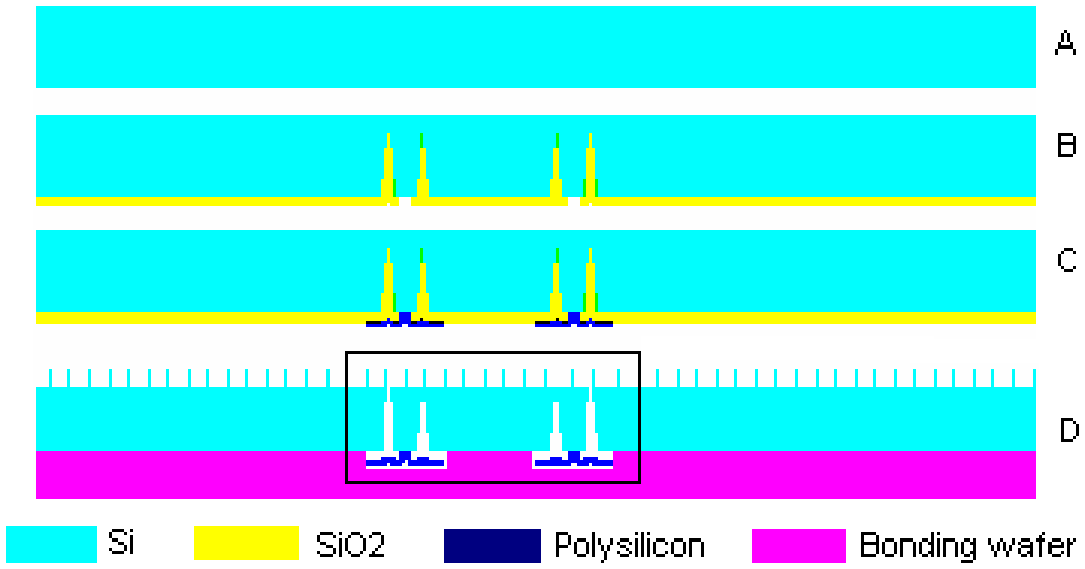

Figure 3.36: Fabrication schematic for proposed ring PhC MEMS structure. Shown is a one-dimensional slice following the line L in Fig. 3.35.

Fig. 3.36 and Fig. 3.37 show one possible fabrication scheme for the proposed structure. The schematic shows a one-dimensional slice following the line L in Fig. 3.35. It is important to note that the entire structure is fabricated on a single wafer using surface micro-machining.

The process begins with the single crystal silicon substrate (Step A). A photolithography step is used to transfer ring pattern to the substrate and the ring shape is created using RIE. The etched circular ring shape is deposited with SiO_2 using PECVD (Step B). SiO_2 is etched along the ring shape to connect the polysilicon to the substrate. Then polysilicon is deposited and is etched outside the ring shape (Step C) creating the rotational ring. The sacrificial SiO_2 is etched away using a highly selective etching method and the backside wafer is bonded to the structure. The last step is to etch the rods using RIE (Step D). The product is indicated in Fig. 3.37. This figure shows the rectangle indicated in Fig. 3.36 in

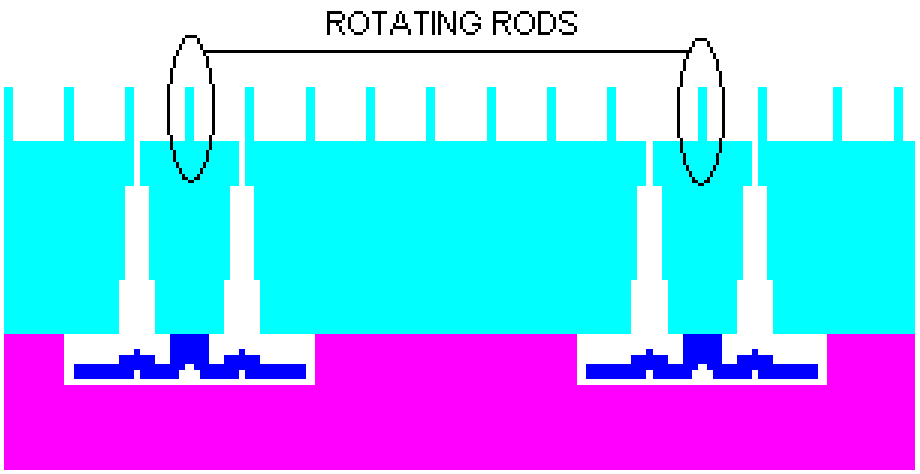

Figure 3.37: The rectangle of Fig. 3.36 is shown in more detail.

more detail. The rotation of the ring will be controlled electrostatically by use of a driver IC. Features such as rotation speed and direction can be adjusted using this external IC. It is also important to note that this is the process scheme for one rotating ring only. In the proposed design there are two counter-rotating rings and a waveguide at their intersection. The second ring will also be fabricated using same steps placed adjacent to the first ring (since they are both on the same substrate), and the waveguide can be created at the last etching step in which the PhC pillars are fabricated.

The proposed rotating rings structure has been discussed with process experts from the fabrication industry and research laboratories. The above process steps are determined by cooperation and support from the Washington Technology Center Microfabrication Facility (WTCMF), which is the largest public microfabrication facility in the Pacific Northwest. This microfabrication lab has a class 100 clean room with various process capabilities including MEMS and micro-optics.

Possible fabrication process steps and methods for the second proposed structure, the sliding plates on an "L" shaped track, are still being investigated. Since the structure composed of rotating rings was discovered before the sliding plates, a detailed analysis (even discussions with process experts from various clean rooms) about the fabrication issues for this structure could be conducted. However, since the performance of the rotating rings

case was not as expected, another topology has been investigated and the sliding plates on an "L" shaped track was discovered. Ultimately, a more profound fabrication analysis of this topology will be conducted in the following years.

3.6 Results

In this section, results associated with each of the proposed wavelength conversion structures will be presented. Both structures are simulated using an enhanced 2D FDTD simulator. This 2D simulator has the capability of accurately modeling and simulating electrodynamics of moving structures because it is enhanced with the 2D version of the linear interpolation method, which is described in detail in section 2 of this thesis. By applying previously suggested linear interpolation to simulate these two much more complicated structures, we prove that the suggested method is also applicable to more complicated cases, and it provides efficiency and accuracy even with these types of hard to model cases [32]. This section is organized as follows. In the first part, details of the FDTD implementation for both of the proposed structures will be discussed. Next, in the following two subsections, test cases and associated results for the proposed structures will be presented.

3.6.1 Implementation in FDTD

First of all, a 2D PhC structure is created in the main FDTD domain. This PhC consists of dielectric rods which are surrounded by air and has a lattice constant of a=1.5 μm. The dielectric constant associated with the dielectric rods is ϵ=12 and air is ϵ=1. Both of these materials, silicon and air, have zero conductivity, relative permeability of one, and they do not have any magnetic losses. These are important parameters that can be set to different values in our FDTD simulator. The lattice distance is divided into 10 space increments, which corresponds to a dx=0.15 μm. To stay in the stability region, the ratio between the space increment and the time step values of the FDTD simulations is set to be dx/dt=$2 \times c$ where c is the speed of light in vacuum. The diameter of the dielectric rods are $0.5a$, which is represented by $5 \times dx$ in discrete space.

The input source frequency used in the simulations is set to be in the band gap of the

2D PhC and we chose to work with the TM (Transverse magnetic) polarized light because dielectric rods in air configuration of the 2D PhCs provides a much larger bandgap with this type of polarization, as described in section 3.3. The frequency of the source is selected to be $0.3 \times c/a$, which is at the low edge of the band gap as indicated in Fig. 3.19. We specifically chose this frequency because in the conducted simulations, the main focus is on an up frequency conversion. Consequently, we wanted the frequency converted light to remain in the band gap for a considerable amount of time so that we would be able to observe the conversion in our analysis. If on the other hand, we had picked the source frequency to be close to the upper edge of the band gap, then after a short time period, the implemented PhC would lose its ability to confine the existing wave because the frequency of this wave would go above the band gap of the PhC. This situation would make the analysis very difficult. In addition, the source used in simulations creates a pulse with a constant carrier frequency and the pulse is shaped with a very wide Gaussian envelope. This specific source type is intentionally selected because of its easier to analyze frequency response. Since the amplitude of the pulse increases very slowly (due to its Gaussian envelope) and the pulse width is very large when compared to the source wavelength, only a single frequency appears when this pulse is Fourier transformed. This is a preferred situation because it is easier to analyze the Doppler shift associated with a single frequency, and also we can predict the behavior of this pulse in the 2D PhC structure more precisely because we can accurately determine where on the band diagram it is. While trying different simulations with different source structures, we encountered situations in which more than one frequency propagated in the PhC waveguide (since the source pumped more than one frequency into the structure), and this made the simulations and calculations messier and harder to comprehend. In addition, the source is specified to be a point source because in FDTD the sources created are "hard sources" which means that we are actually forcing a single point in the calculation domain to have a specific field value in every time step. This is against the nature of the FDTD calculations and causes reflections from that point as if there were a perfect mirror at that specific spot. A point source rather than a plane wave (in which case a vertical line of points in the calculation domain are forced to the source field value) is preferred to decrease the amount of reflections to negligible levels.

In each simulation, each rod in the main FDTD window is represented as a separate object, a separate entity in other words. The developed FDTD simulator is object oriented which aims to make the simulations more efficient and decrease the simulation times. In this scheme, there are two main classes: 1) Stationary objects 2) Moving objects. For the stationary objects, the geometric and electromagnetic coefficients are calculated only once and these initially calculated values are used in each time step to estimate the electric and magnetic fields in the FDTD domain. However, when there is motion in the main FDTD window, these coefficient need to be updated around the moving object. Since we have a separate class for moving objects, only the regions around moving objects are updated in the simulation, which decreases the simulation time considerably. Similarly, the 2D version of the linear interpolation method is applied only to the moving objects, and not to the stationary objects. Furthermore, each object in the moving objects class can have its specific motion function. Ultimately, each object in the simulation domain can move according to a required motion trajectory. In our test cases, we have two separate motion trajectories, which will be discussed in the following sections, but our simulator is capable of simulating many different trajectories due to its object oriented nature.

To be able to observe and analyze the parameters associated with the fields that are present in the simulation domain, monitors are used. They are analogous to the ossiloscope probes in electronic circuits, and we used these monitors to record and check the field characteristics in different parts of the structures we simulated. Also, the periphery of the main FDTD window is covered with a perfectly matched layer which behaves as an absorbent and prevents reflections from the edges of the simulation area.

3.6.2 Rotating Rings

In this section, implemented test cases and results associated with the proposed rotating rings structure will be provided and analyzed. This structure is implemented and simulated in our FDTD simulator to prove that it actually performed as expected in terms of wavelength conversion.

The details of the first test case we simulated is shown in Fig. 3.38 at three different times. In this test case, each of the rotating rings are simulated to rotate total of 10 degrees in 7

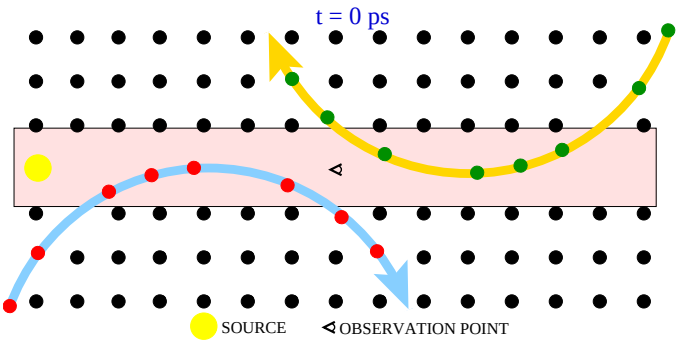

(a)

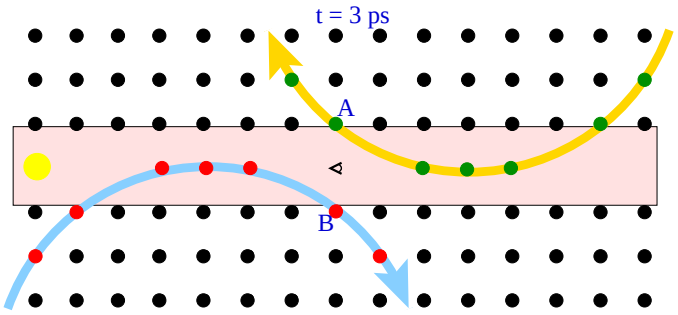

(b)

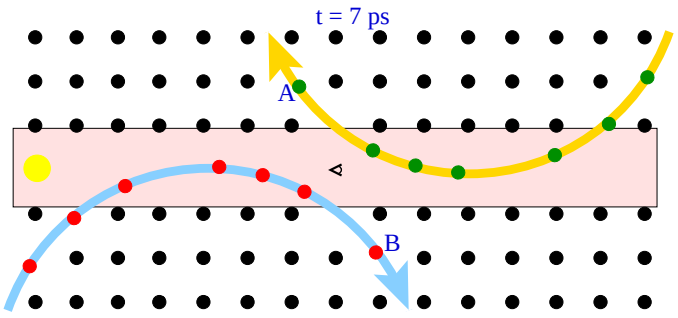

(c)

Figure 3.38: Simulated rotating rings structure is indicated at three different time steps. The PhC rods that are on the NEMS rings are indicated with different colors. The trajectories of the rings are also shown with large arrows. The angular velocity of the rotation is w=240 $\times$ 10^9 rpm=8π $\times$ 10^9 rad/s. Initially at t=0 ps, the rings are rotated -5 degrees. Around t=3 ps, the waveguide is closed and the light is trapped in the cavity which we observed using the indicated observation point. After the rings open at t=7 ps, the frequency shifted light will continue to propagate on the waveguide.

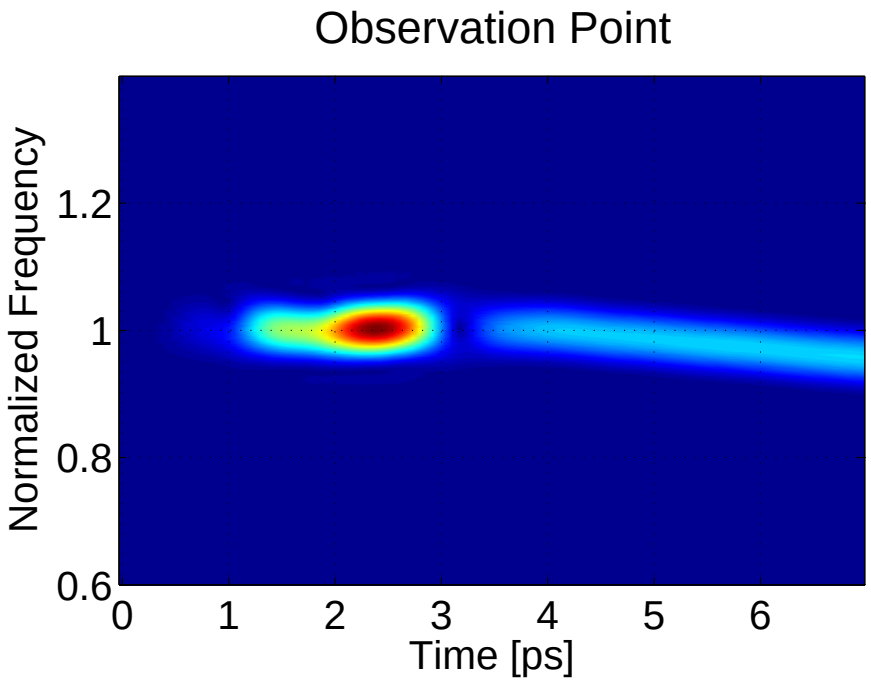

Figure 3.39: The spectogram result associated with the simulated structure indicated in Fig. 3.38

ps, and the diameters of the large rings are 10 lattice constants. The moving dielectric rods on two large NEMS rings are indicated with different colors, and their motion trajectory is indicated with two large circular arrows. The angular velocity of the rotating NEMS rings is 240×10^9 rpm, which corresponds to $8\pi \times 10^9$ rad/s. At t=0 ps each NEMS ring is rotated -5 degrees from its perfect configuration which is shown in Fig. 3.31. The source is located on the left side of the waveguide. Initially, since with the -5 degrees rotation as shown in Fig. 3.38 (a), the periodicity of 2D PhC structure is disturbed, some amount of the pulse created by the source will couple into the cavity which we will observe using the observation point located in the middle. Next, the rotation begins and the moving rods on each rotational NEMS ring moves as indicated by the large arrows. At t=3 ps, the configuration of the structure becomes as shown in Fig. 3.38 (b). In this configuration, the cavity is closed from two sides and since the moving rods are aligned with the periodic structure of the 2D PhC, the light is trapped in the cavity. After this point, as the moving rods on the waveguide get closer to each other, the trapped light is supposed to gain an

up frequency conversion. Since the speed of the trapped light is much higher than the velocity of the moving rods, the trapped light will bounce off of the moving rods millions of times gaining a small frequency shift each time. As a result, as time advances and the structure reaches to the configuration indicated in Fig. 3.38 (c), what we expect to see is a considerable amount of up frequency conversion in the frequency of the trapped light.

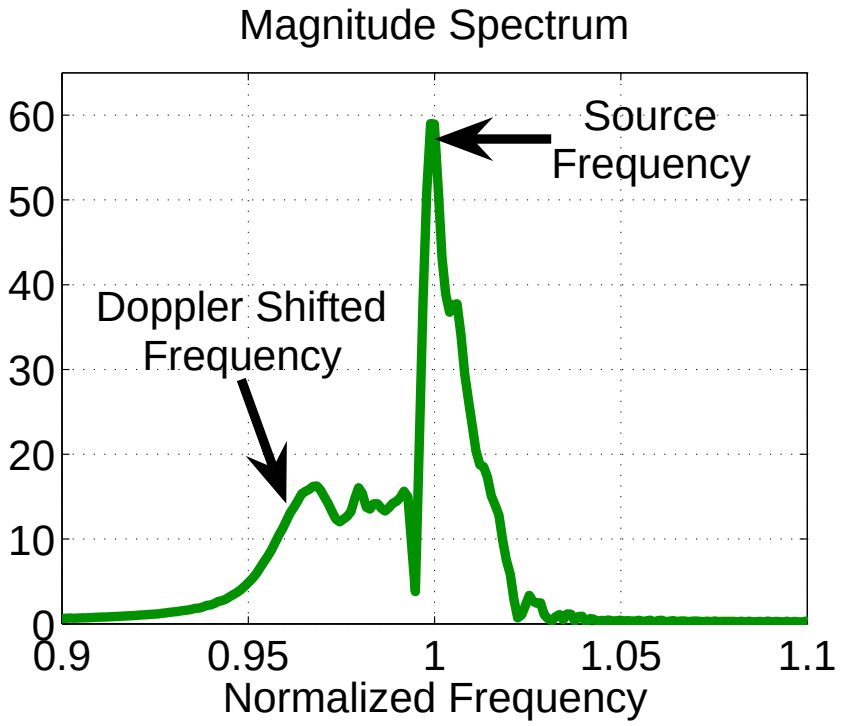

Figure 3.40: Frequency spectrum associated with the simulated structure indicated in Fig. 3.38

However, when the frequency on the observation point is analyzed in detail and a spectogram associated with it is plotted as a function of time as shown in Fig. 3.39, a very interesting result is observed. As the time advances, the frequency of the trapped light decreases by almost 5% instead of increasing as expected. The exact same result is also obtained when the time signal on the observation point is Fourier transformed into the frequency domain. This result is indicated in Fig. 3.40. The frequency axis is normalized to the input source frequency, and the magnitude spectrum is plotted as a function of normalized frequency. In this figure, the initial source frequency and the down shifted Doppler

frequency are indicated. We can observe the 5% drop in the frequency in this figure too.

After some investigation, the reason for this decrease is discovered to be emerging as a result of the moving rods marked as "A" and "B" in Fig. 3.38 (b) and (c). We had expected that as the moving rods on the waveguide got closer to each other (in other words, as the cavity along the waveguide gets compressed), the trapped light would gain an up conversion. However, as the rings rotate, another cavity in the direction of the straight line between rods "A" and "B" is created, and the size of this cavity increases as time advances. Consequently, since the moving rods marked as "A" and "B" are moving away from each other, a down frequency conversion will occur in this vertical cavity. To sum up, the trapped light can travel in two different cavities one of which is compressing (up conversion) and the other is decompressing (down conversion). At this point, an important and interesting question that can be raised is why the frequency of the trapped light decreases but not increases? The answer to this question can be found when the cavity lengths for each of these cavities are considered. Since the length of the cavity that is decompressing (opening) is smaller when compared to the length of the cavity that is compressing (closing), the number of reflections occurring in the opening cavity direction (the straight line between rods "A" and "B") is larger than the number of reflections occurring in the closing cavity direction (along the waveguide). Ultimately, there is an up frequency conversion but the down frequency conversion is larger than the up conversion so we observe a net frequency change in the down conversion direction.

To test if this was the real reason for the down frequency conversion, we created the second test case which is indicated in Fig. 3.41 for three different time steps. In this case, the only moving rods are the ones in the waveguide, and the rest of the moving rods shown in Fig. 3.38 on the large circular arrows are replaced with stationary rods which complete the 2D PhC periodicity. Initially, the moving rods are rotated by $-\theta$ degrees, and the trajectory of the motion for these rods are indicated by circular arrows in Fig. 3.41 (a). At this time step, since the periodicity of the 2D PhC structure is disturbed by the $-\theta$ degrees of rotation, some part of the pulse created by the source which is located at the left edge of the waveguide will couple into the created cavity. In 3 ps, the moving rods rotate θ degrees and creates the configuration shown in Fig. 3.41 (b). After this time step, moving rods

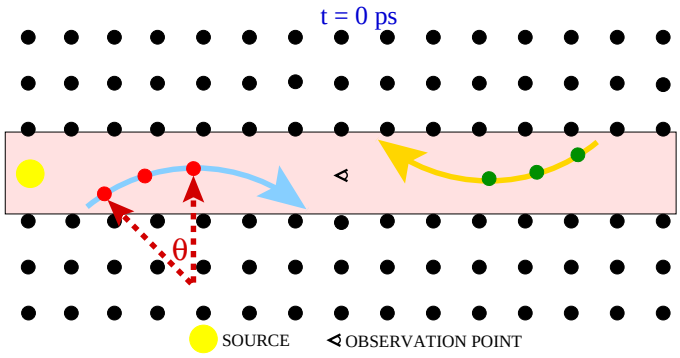

(a)

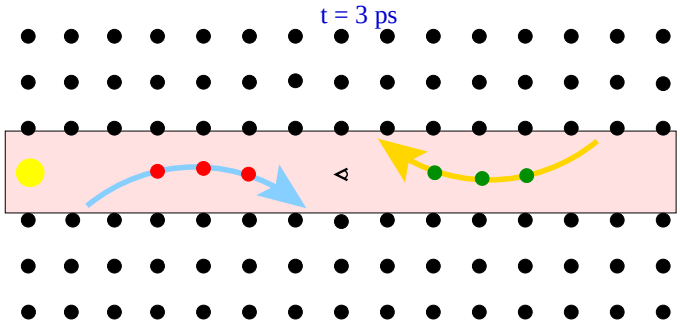

(b)

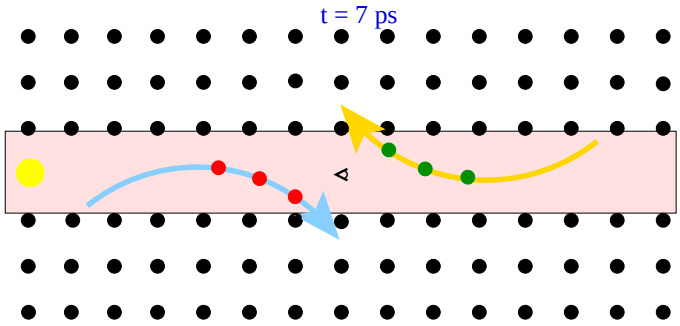

(c)

Figure 3.41: The time line for the same structure shown in Fig. 3.38, but this time the only moving rods are the ones on the waveguide. The rest of the rods are stationary.

continue to rotate in the shown direction till they reach to the indicated configuration at t=7 ps as shown in Fig. 3.41 (c). As the rods move towards each other, the trapped light will gain a Doppler shift in a similar manner discussed before in the previous test case. However, this time there is only one cavity which is compressing (closing) and its length is getting smaller as time advances. Since the moving rods on the side walls of the waveguide are replaced with stationary rods in this test case, the decompressing (opening) cavity is removed. In all three time steps of Fig. 3.41, the characteristics of the coupled and trapped light in the cavity is monitored at the observation point indicated in this figure.

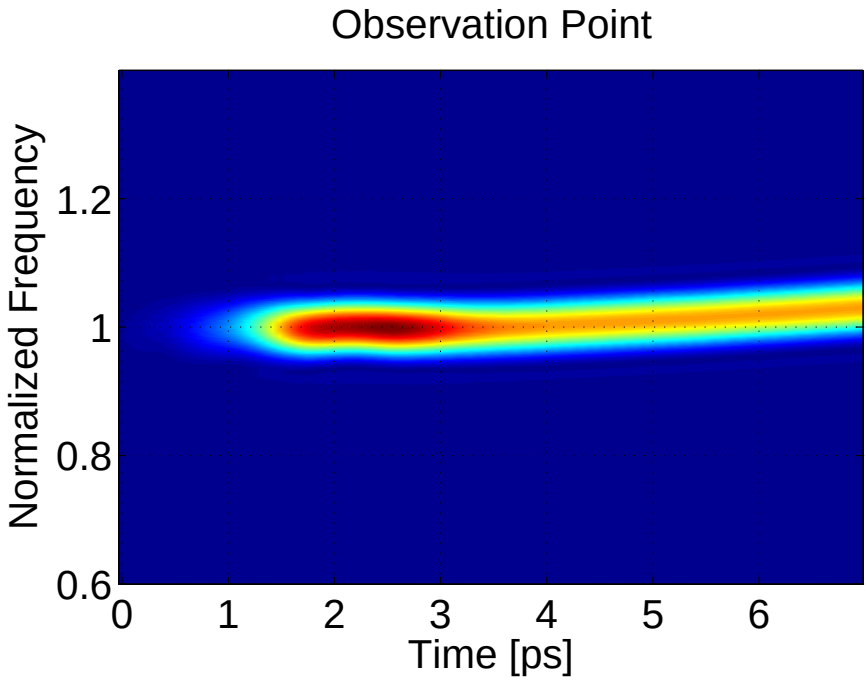

Figure 3.42: The spectogram figure associated with the simulation of the structure shown in Fig. 3.41 with θ=5 degrees. The result indicates a Doppler shift of almost 2.5 %.

When this structure is implemented and simulated for θ=5 degrees (w=240 $\times$ 10^9 rpm=8π $\times$ 10^9 rad/s), we get the spectogram result indicated in Fig. 3.42. As can be seen in this figure, there is an up frequency conversion which proves our previous reasoning about the observed down frequency conversion in the previous test case to be correct. There is approximately 2.5 % up frequency conversion in this case because there is only one cavity which is compressing along the waveguide. The decompressing cavity that was introduced

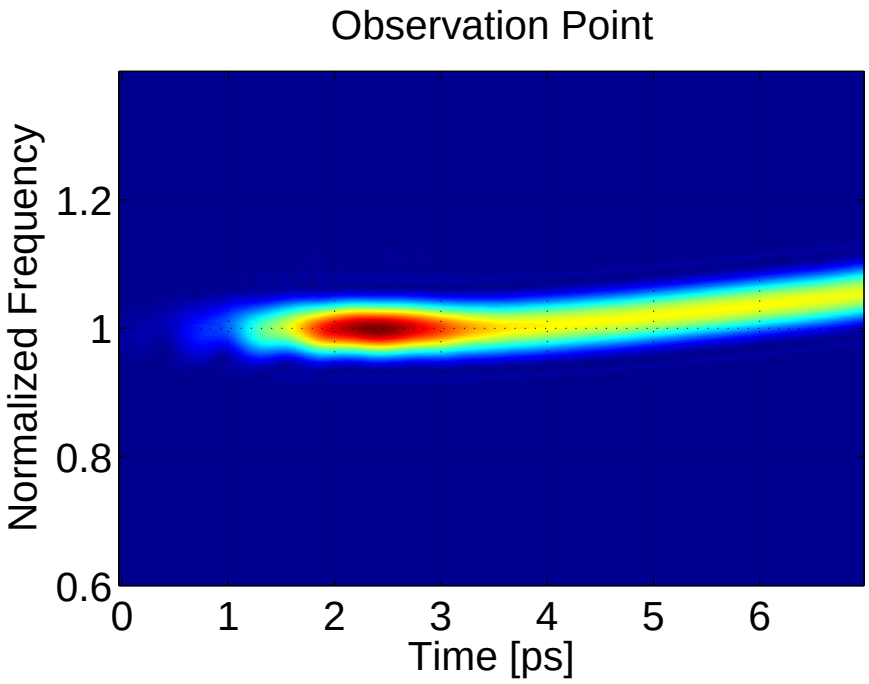

Figure 3.43: The spectogram figure associated with the simulation of the structure shown in Fig. 3.41 with θ=8 degrees. The result indicates a Doppler shift of almost 5 %.

in the previous case is removed by replacing the moving rods that cause the down frequency conversion with stationary ones.

To test the effect of NEMS velocity on the amount of accumulated Doppler shift, we simulated the same test case with a higher rotation degree: θ=8 degrees in the same amount of time. This corresponds to an angular velocity of w=378×10^9 rpm=$12.6\pi\times10^9$ rad/s. As expected this caused a higher Doppler shift as indicated in the spectogram of Fig. 3.43. For $\theta = 5$ degrees, we had a frequency conversion of 2.5 % and for $\theta = 8$ degrees, a frequency conversion of almost 5 % is achieved. In both of these spectogram figures, the normalized frequency at the observation point is plotted as a function of time.

When the time signal of the observation point is Fourier transformed for these two cases, we get the magnitude spectrum result indicated in Fig. 3.44. In this figure, the frequency spectrums associated with both θ=5 degrees and θ=8 degrees are plotted as a function of normalized frequency. The frequency axis is normalized to the input source frequency. The input frequencies and the Doppler shifted frequencies for each case is indicated in the figure.

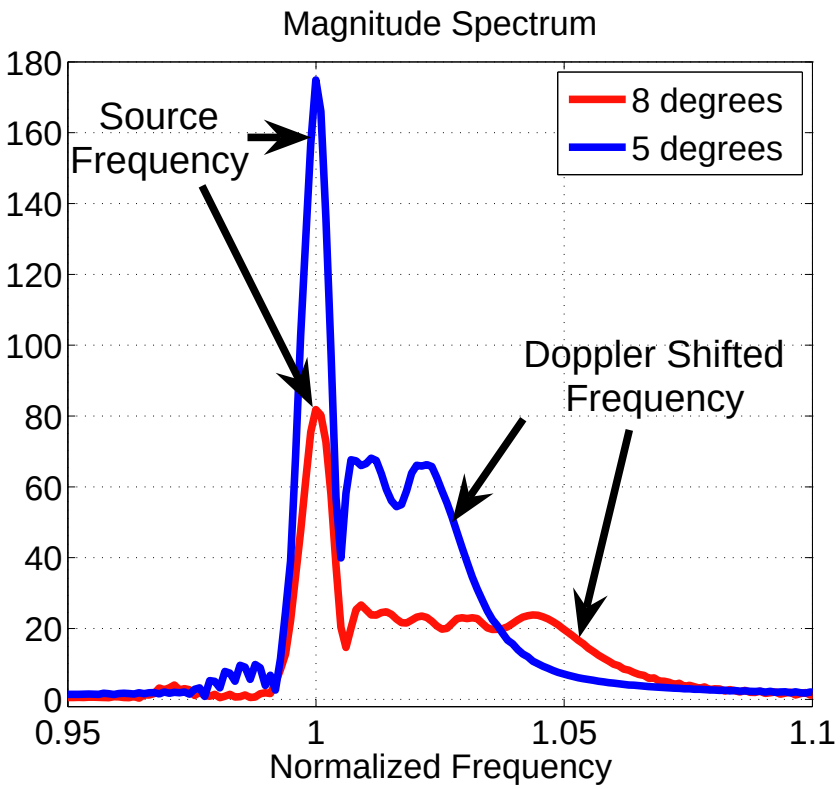

Figure 3.44: Frequency spectrum associated with the spectogram results indicated in Fig. 3.42 and Fig. 3.43. The results match with each other.

These results overlap with the results indicated in the spectogram figures for each case.

Results indicate that the proposed rotating rings structure is capable of all-optical wavelength conversion. However, at this point, we should consider some important issues regarding the performance of such a device. First of all, efficiency of this structure should be analyzed in some depth. Efficiency is the measure of how much of the input energy with the initial wavelength has been converted to the new wavelength. In the rotating rings structure, since the moving rods are near the ideal position for a very small percentage of the time, the efficiency is expected to be at very low levels. When the moving rods are in a position that disturbes the periodicity of the PhC structure, some of the trapped light will leak out of the cavity. This is the main reason behind the low efficiency of the rotating rings structure.

The velocity of the NEMS rings that is used in the conducted rotating rings simulations is another important issue that needs to be discussed. For these simulations we used w=240×10^9 rpm=$8\pi\times10^9$ rad/s (and w=378×10^9 rpm=$12.6\pi\times10^9$ rad/s). These values are not very practical because highest angular velocity achievable using today's MEMS/NEMS technology is on the order of 10^6 rpm. These angular velocity values are chosen for convenience, because the simulations would take a very long time if we had simulated the proposed structure using the practical MEMS/NEMS velocities. Also, changing the velocity of the rotation only changes the total amount of time that is required to reach to the same wavelength conversion amount. For example, if angular velocity of w=w_0 causes a % frequency conversion in t=t_0 seconds, then w=$0.5 \times w_0$ causes a % frequency conversion in t=$2 \times t_0$ seconds. The change in the velocity is reflected as a scale factor in the time axis. This makes sense because with higher velocity, the amount of Doppler shift for each reflection will be larger but the total time of conversion is small. For the small velocities on the other hand, the amount of Doppler shift for each reflection will be smaller but the total time of conversion is large.

One last issue that needs to be considered in connection to the MEMS/NEMS velocity is the pulse shape preservation. Since different amounts of the trapped light leaves the cavity at different times (depending on the position of the moving rods), the pulse shape of the input beam cannot be preserved after the wavelength conversion. In other words, the

input pulse (as a result of the interactions with the moving NEMS structure) heterogenously spreads out and loses its shape. This means that the data decoded on the input beam (by amplitude modulation) is lost after the conversion. Furthermore, a more profound analysis on the issue can be conducted if the optical data rate (data period) and the confinement time in the cavity of the proposed structure are compared. If a 100 Gb/s optical data rate is assumed in an optical network, then the received/transmitted data period will be 10 ps. This means that the rotating rings wavelength conversion mechanism will need to sample an individual data bit every 10 ps. The results indicated in Fig. 3.42 and Fig. 3.43 show a confinement time of 7 ps, in which a total wavelength conversion of 2.5 % and 5 % are achieved respectively. Even though the confinement time in these cases seem to be compatible with the optical data period of a 100 Gb/s optical network, the MEMS/NEMS velocities used in these simulation that provide the mentioned confinement time is not practical. On the other hand, if the optical data rate is assumed to be 1 Gb/s, then the optical data period will be 1 ns. A compatible confinement time in the rotating rings structure can be achieved with a MEMS/NEMS velocity on the order of w=240×10^7 rpm, which is still slightly larger then the practical (available) velocities, but definitely more reasonable.

3.6.3 Sliding plates on an "L" shaped track

In this section, implemented test cases and results associated with the sliding plates on an "L" shaped tracks structure will be provided and analyzed. This structure is implemented and simulated in our FDTD simulator to prove that it actually performed as expected in terms of wavelength conversion.

The details of the test case we simulated is shown in Fig. 3.45 at three different times. Initially at $t = 0$ ps, the moving rods are in their initial position and they are indicated with different colors than the stationary rods. The source is placed in the middle of the waveguide and next to it is an observation point (monitor). This is shown in Fig. 3.45 (a). In the first 4 ps, the moving rods slide in a perpendicular direction to the waveguide using the NEMS plates below, and at $t = 4$ ps they reach to the configuration indicated in Fig. 3.45 (b). At this time step, a cavity is created and the existing light is trapped in this

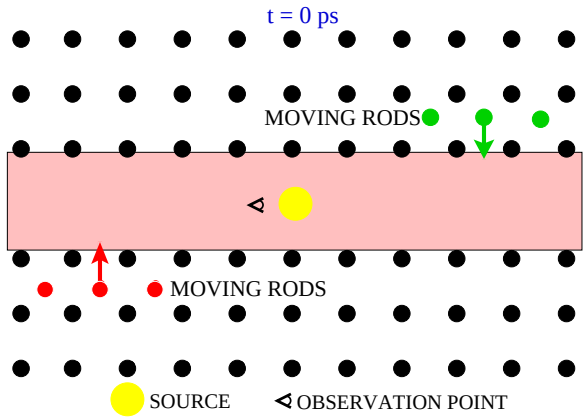

(a)

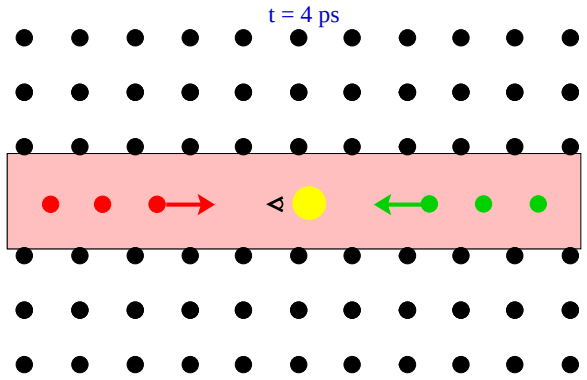

(b)

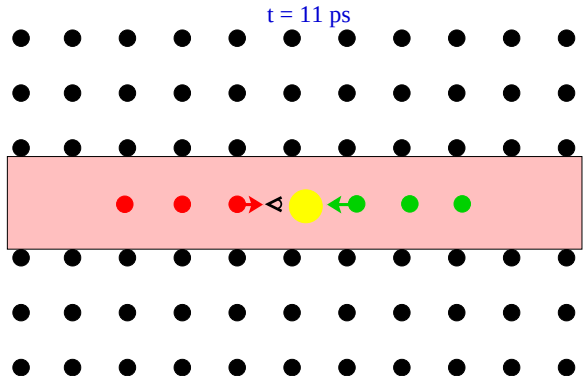

(c)

Figure 3.45: Simulated "L" shaped tracks structure is indicated at three different time steps. The PhC rods that are on the NEMS rings are indicated with different colors. The motion directions of the sliding plates at each time step are also shown with large arrows. The velocity of the sliding NEMS plates is $v_0 = 6.6 \times 10^5$ m/s. Initially at t=0 ps, the moving rods are not in the waveguide. For 4 ps, the moving NEMS plates and the moving rods above them slide towards the waveguide. At t=4 ps, they reach to the center of the waveguide and create a cavity.

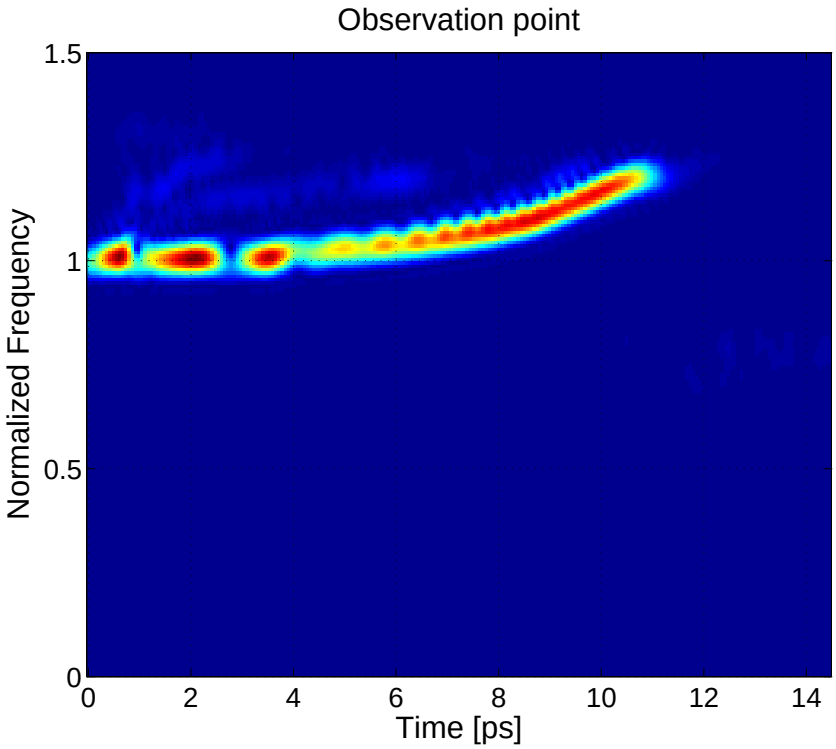

Figure 3.46: Spectogram figure associated with the simulated structure shown in Fig. 3.45. The velocity of the plates is $v{=}v_0$.

cavity. The trapped light is confined perfectly because the wavelength of this pulse is in the band gap of the 2D PhC that surrounds it. After this time step, the moving rods start to move towards each other and compress the trapped light in the cavity where cavity length is getting smaller and smaller as the rods come closer to each other. Fig. 3.45 (c) shows the structure at $t = 11$ ps where it is getting very close to full compression.

The result associated with this test case is indicated in Fig. 3.46. In this figure, frequency of the TM polarized electric field at the observation point is plotted as a function of time. The time axis is in units of *ps* and the frequency axis is normalized to the input source frequency. As can be observed from this figure, till $t = 4$ ps the only frequency present in the observation point is the source frequency. In this time period, the rods are moving in the perpendicular direction to the waveguide, consequently no Doppler shift is observed in the electromagnetic wave that can propagate in the waveguide. However, after $t = 4$ ps, since some amount of light is trapped in the created cavity and the rods start to move towards each other parallel to the waveguide, the frequency of the trapped light starts to increase. Each time the trapped light reflects from the compressing rods, it gains a small amount of Doppler shift. Yet since the speed of the trapped light is much faster than the speed of the rods, the trapped light will bounce off millions of times of the moving rods gaining a large amount of Doppler shift. This can actually be observed in this figure where in approximately 7 ps, a frequency conversion of 20% is achieved. Fig. 3.46 points to a very interesting phenomenon at $t = 11$ ps when the electromagnetic wave in the FDTD disappears. Basically, as a result of the Doppler shift the trapped light gains from the moving NEMS rods, its frequency starts to increase, and at $t = 11$ ps the wavelength of the trapped light gets out of the band gap region of the 2D PhC implemented in the structure. Consequently, the light propagates out of the structure through the perfectly matched layers (PMLs) that surround the main FDTD window.

When we take the Fourier transform of the electric field at the monitored position, we get the result indicated in Fig. 3.47. In this figure, the magnitude spectrum of the trapped light is shown in the frequency domain. The frequency axis is normalized to the source frequency and as a result, a normalized frequency value of one indicates the light with the source wavelength. There is a large frequency component at the source frequency as

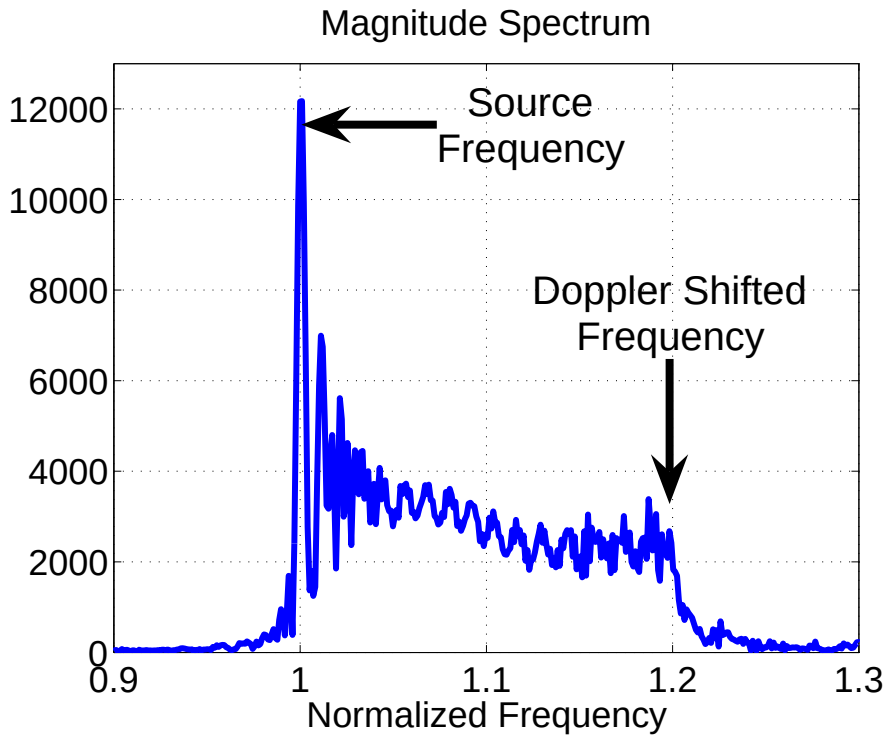

Figure 3.47: Frequency spectrum associated with the simulated structure shown in Fig. 3.45.

expected because initially when the rods are moving in a perpendicular direction to the waveguide, the only frequency present in the cavity is the source frequency. However, after the moving rods start to move towards each other and compress the cavity, new frequency components start to emerge. The generated frequency characteristics change as a function of time as the Doppler shift is accumulated and as the cavity length gets smaller. Furthermore, since the frequency conversion from the initial source wavelength to the highest Doppler shifted frequency (indicated at t=11 ps in Fig. 3.46) is continuous in time, in the frequency spectrum all the frequencies in this range exist which can be observed in Fig. 3.47.

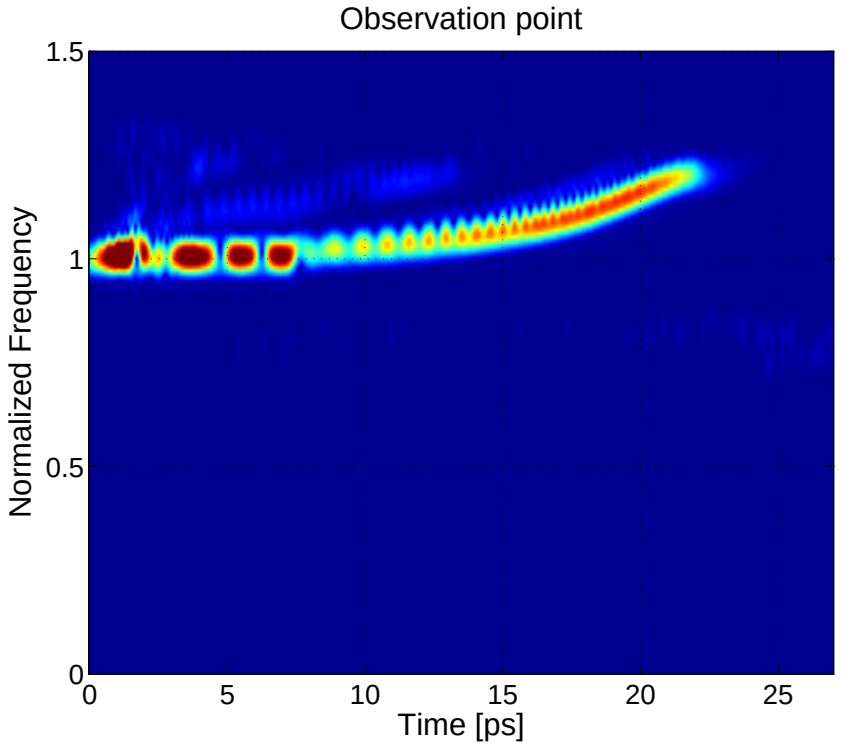

Figure 3.48: Spectogram figure associated with the simulated structure shown in Fig. 3.45. This time the velocity of the plates is v=0.5 × v_0.

The velocity of the sliding NEMS rods in this simulation is $v_0 = 6.6 \times 10^5$ m/s. Even though this velocity value is not practical, and today's MEMS/NEMS devices cannot provide velocities on this order, it is chosen for convenience. Using a slower velocity in the FDTD simulations would cause very long simulation times. Since the velocity of the moving structures has an important effect on the Doppler shift, we also wanted to check the effect

of the velocity of the NEMS rods on the spectogram results we presented in Fig. 3.46. Ultimately, we tested the same structure with the same test scenario but with the half NEMS velocity this time, where $v = 3.3 \times 10^5$ m/s $= 0.5 \times v_0$. Since the Doppler shift amount is linearly proportional to the velocity of the moving structure, we expected to see the same amount of frequency conversion in a longer time period. The resulting spectrogram for this simulation is indicated in Fig. 3.48. As expected, the same events happen but in a longer time range. In the previous case, the trapped light gets through a frequency conversion for 7 ps and disappears at $t = 11$ ps. However, in the second case where the velocity is decreased by a factor of two, the trapped light goes through a wavelength conversion for 14 ps and disappears at $t = 22$ ps. Consequently, with the practical MEMS/NEMS velocities (which are much smaller than the values used in these simulations) we would still get the same amount of Doppler shift, but it would take longer time.

Another important issue is the pulse shape preservation. As in the case of the rotating rings structure, the "L" shaped rectangular tracks structure cannot preserve the input pulse shape at this level of our research. As in the case of rotating rings structure, a similar confinement time - optical data period comparison should be conducted for this structure too. A 100 Gb/s data rate means an optical data period of 10 ps. Results in Fig. 3.46 indicate a total of 20 % wavelength conversion with a comfinement time of 11 ps. However, this confiment time is possible with a MEMS/NEMS velocity of $v_0 = 6.6 \times 10^5$ m/s, which is not practical. At this level of our research, we do not have a perfect answer for this pulse shape preservation issue. There may be two possible solutions to this problem. First one is decreasing the initial cavity length, which we think will decrease the necassary confinement time many orders. This makes sense because as the sliding plates get closer to each other, the rate of conversion increases exponentially. The second possible solution is confining a data train (many data bits) at the same time, and converting them all at once. However, this idea has not been simulated and tested in detail yet. Consequently, this issue needs more time and will be analyzed in more detail in the following years.

In addition, with this structure, another important issue emerges because the conversion amount can reach to very high levels. As mentioned before, after the wavelength convertion, the trapped light cannot be confined in the waveguide anymore because its new frequency is

out of the band gap of the PhC. Consequently, to be able to confine this new frequency, the whole "L" shaped rectangular tracks structure can be embedded in another PhC structure, whose dimension are arranged accordingly so that this new wavelength is in its band gap.

At this point, we should also analyze the "L" shaped rectangular tracks structure in terms of its efficiency. First of all, the conversion efficiency of this structure is expected to be much higher when compared to the rotating rings structure. In this structure, after the sliding NEMS plates close the waveguide and create a cavity, the trapped light will be confined much more effectively because the side walls of the cavity consists of perfectly aligned PhC rods now. As a result, the amount of leaks of light from the cavity will be much less when compared to the rotating rings structure, and this in turn provides a higher wavelength conversion efficiency.

3.7 Future Work

The presented results indicate that the proposed PhC MEMS/NEMS structures provide all-optical wavelength conversion as expected. However, there are some very important points that need to be considered in more detail for the realization of this device. In this subsection, these points will be analyzed and discussed.

First of all, efficiency of the proposed structures emerges to be a very important issue. It is important to note that due to the small percentage of the time that the moving rods are near the ideal position, very little light will undergo the frequency shift in the rotating rings case. To solve this issue and increase the efficiency of this architecture, recirculation of the output port of the waveguide into the input can be used. In this case, the unconverted light is recycled and converted in the next rounds. Narrow bandpass photonic crystal structures can be used to allow the converted light to be directly output of an exit port of the loop. Conversion efficiencies of near 100% may be possible in such an architecture. This problem is not very dramatic in the case of the second structure, sliding plates on "L" shaped tracks. In this case, after the moving rods are in the waveguide and start to close the cavity, light is confined much better in the cavity because of the periodic 2D PhC side walls which provide relatively high reflection coefficients. Consequently, the efficiency problem is not

as dramatic as in the case of rotating rings structure. A more detailed analysis on the efficiency of the sliding plates on "L" shaped tracks structure is still being conducted.

A second important issue is the pulse shape preservation. In order to be used in the WDM mechanisms of today's optical communication networks, the proposed all-optical wavelength converter also needs to preserve the pulse shape of the input. This is extremely important because the optical data is encoded using the pulse shape of the transmitted light, and losing the pulse shape information is the same as losing the data. The proposed structures are not capable of preserving the pulse shape of the input yet, and the amplitude information is lost during the wavelength conversion process. However, this issue is being investigated, and the existing structures will be improved in the following years in order to solve this problem.

Finally, a third important issue is the fabrication of the proposed structures. In the design process of the rotating rings structure, a detailed process analysis is also conducted in parallel to come up with a reasonable fabrication scheme. The results associated with this research is indicated in section 3.5.2. A similar fabrication analysis will also be conducted for the sliding plates on "L" shaped tracks structure. The fabrication issue is very complicated and difficult because we are trying to integrate two hard to fabricate structures, PhCs and NEMS. Ultimately, experts from various clean rooms and fabrication facilities will be contacted to discuss the realization of the proposed design. Depending on the feedback received from these experts, the structure will be improved.

Chapter 4

Conclusions

The recent rapid advancements in nanotechnology have affected not only various domains in academia and industry, but have also led to various applications in many different fields. Some of these products are still at the research level, while some of them have already become commercially available and popular. These advancements inevitably affected the optical communications domain too. By means of WDM and EDFAs, very high data transfer rates are reached. However, globally increasing levels of bandwidth and capacity requirements spur the optical communications industry to produce new products that are faster, more powerful, and more efficient. Especially, optical-electronic-optical (O-E-O) conversions in WDM mechanisms prevent higher data transfer speeds and create a serious bottleneck for the optical communications. Wavelength converter segments of WDMs suffer the most from these O-E-O transitions and as a result all-optical wavelength conversion methods have become extremely important.

In this thesis, we proposed two state-of-the-art, all-optical wavelength conversion mechanisms that are composed of integration of PhCs with NEMS structures. The first structure is the rotating rings, and the second one is sliding plates on "L" shaped tracks. We have observed that both of these structures performed frequency conversion, yet the conversion in rotating rings structure is not as expected due to the unpredicted cavity formations in the structure. The sliding plates on "L" shaped tracks structure on the other hand, performs much more effectively and as anticipated. A wavelength conversion of 20 % is

achieved using this structure, which is much higher when compared to the rotating rings. The efficiency associated with sliding plates on "L" shaped tracks structure is still being investigated, yet preliminary results indicate that it is considerably higher than the efficiency of the rotating rings structure. At this point, it is also important to note that none of the proposed wavelength conversion mechanisms preserve the pulse shape of the input light. In other words, the shape of the optical data is lost during the conversion process. In order to become a commercially viable technology, the proposed structures should provide all optical wavelength conversion while preserving the pulse shape of the input light. This very important issue is also still being investigated in detail, and we are looking for possible improvements to the structure to accomplish this goal. Another crucial issue is the fabrication of the proposed structures. One possible process flow for the rotating rings structure is provided as a result of a detailed research in the PhC-NEMS fabrication domain and interaction with many experts from the commercial and academic fabrication facilities. A very similar analysis will also be conducted for the second structure, sliding plates on "L" shaped tracks, which performs better than the rotating rings. The fabrication issue for these types of structures is a very serious one and needs a lot of effort and consideration.

Furthermore, the ability to more accurately model structures with wavelength scale dimensions is a very essential requirement for the nanophotonics area, especially in the presence of moving MEMS/NEMS structures which will cause a frequency shift due to the Doppler effect. One method to partially accomplish this is the finite-difference time-domain (FDTD) method, which numerically solves Maxwell's equations in discrete time and space. However, the traditional FDTD is not sufficient to accurately and efficiently model nanoscale structures that include motion, such as the proposed wavelength conversion mechanisms in this thesis. Consequently, to solve this problem and to be able to accurately simulate the proposed PhC-NEMS structures, we presented the "linear dielectric interpolation" method as part of this thesis. The basic algorithms for this method are very efficient and easy to implement as discussed in detail in section 2. Results indicate that this is a very useful method to implement when FDTD is being used to simulate structures with motion. The FDTD simulations enhanced with this method are more stable and more accurate (in terms of spurious frequency content) than the regular FDTD simulations when there is motion in

the structure. The two dimensional version of the "linear dielectric interpolation" method is also used to model the PhC-NEMS wavelength convertors that are proposed in this thesis, and it provided a good level of accuracy to the FDTD simulations.

Bibliography

[1] K. D. Akdemir and B. M. King. Analysis of fabrication processes for photonic crystal MEMs/NEMs structures. In *OSA Annual Meeting*, Tucson, Arizona, October 2005.

[2] N. Antoniades, S. J. B. Yoo, K. Bala, G. Ellinas, T. E. Stern, and L. Fellow. An architecture for a wavelength-interchanging cross-connect utilizing parametric wavelength converters. *Journal of Lightwave Technology*, 17:1113–, 1999.

[3] C. Baek, S. Song, J. Park, S. Lee, J. Kim, W. Choi, C. Cheon, Y. Kim, and Y. Kwon. A V-band micromachined 2-D beam-steering antenna driven by magnetic force with polymerbased hinges. *IEEE Trans. Microw. Theory Tech.*, 51(1):325–331, 2003.

[4] J. Bainbridge, A. Sharafi, I. White, M. Cowin, M. Stephens, M. O. R.V., and Penty. All-optical routing using a 12x12 passive InP wavelength selective router and tuneable wavelength conversion. In *IEE colloquium on multiwavelength optical networks: devices, systems and network implementations*, London, June 1998.

[5] S. Barkou, J. Broeng, and A. Bjarklev. Guidance of light along an air column in a new class of optical fibers. *DOPS-NYT*, 14(16), 1999.

[6] J. P. Berenger. A perfectly matched layer for the absorption of electromagnetic waves. *Journal of Computational Physics*, 114:185–200, 1994.

[7] J. V. Bladel. *Relativity and Engineering*. NewYork: Springer-Verlag, 1984.

[8] P. Blondy, D. Mercier, D. Cros, P. Guillon, P. Rey, P. Charvet, B. Diem, C. Zanchi, L. Lapierre, J. Sombrin, , and J. B. Quoirin. Packaged millimetre wave thermal MEMS

switch. In *Proc.31st European Microwave Conf.*, pages 283–286, London, September 2001.

[9] R. Borwick, P. Stupar, J. DeNatale, R. Anderson, and R. Erlandson. Variable MEMS capacitors implemented into RF filter systems. *IEEE Trans. Microw. Theory Tech.*, 51(1):315–319, 2003.

[10] J. Broeng, T. Sondergaard, S. Barkou, P. Barbeito, and A. Bjarklev. Waveguidance by the photonic bandgap effect in optical fibres. *J OPT A-PURE APPL OP 1*, 4:477–482, July 1999.

[11] N. Bushyager, K. Lange, M. Tentzeris, and J. Papapolymerou. Modeling and optimization of RF reconfigurable tuners with computationally efficient time-domain techniques. In *IEEE MTT-S Int. Microwave Symp.*, volume 2, pages 883–886, Seattle, WA, June 2002.

[12] J. Chiao, Y. Fu, D. Choudhury, and L. Lin. MEMS millimeter wave components. In *Proc. IEEE MTT-S Int. Microw. Symp.*, pages 463–466, Anaheim, June 1999.

[13] Y. Chiao, J.C.and Fu, I. Chio, M. Delisio, and L. Lin. MEMS reconfigurable vee antenna. In *Proc. IEEE MTT-S Int. Microw. Symp.*, pages 1515–1518, Anaheim, June 1999.

[14] R. C. Costen and D. Adamson. Three dimensional derivation of the electrodynamic jump conditions and momentum-energy laws at a moving boundary. *Proc. IEEE*, 53(9), Sept 1965.

[15] M. J. A. de Dood. *Silicon photonic crystals and spontaneous emission.* PhD thesis, Utrecht University, 2002.

[16] R. M. de Ridder and R. Stoffer. Finite-difference time-domain modelling of photonic crystal structures. In *Int. Conf. on Transparent Optical Networks*, pages 22–25, Warsaw, Poland, 2001.

[17] Z. Feng, W. Zhang, B. Su, K. F. Harsh, K. C. Gupta, V. Bright, and Y. Lee. Design and modelling of RF MEMS tunable capacitors using electro-thermal actuators. In *Proc. IEEE MTT-S Int. Microw. Symp.*, pages 1507–1515, Anaheim, June 1999.

[18] R. Feynman. There's plenty of room at the bottom: an invitation to open up a new field of physics. *Engineering and Science (California Institute of Technology)*, 23(5):22–36, 1960.

[19] J. G. Fleming, S. Y. Lin, I. El-Kady, R. Biswas, and K. M. Ho. All-metallic three-dimensional photonic crystals with a large infrared bandgap. *Nature*, 417:52–55, 2002.

[20] J. S. Foresi, P. R. Villeneuve, J. Ferrera, E. R. Thoen, G. Steinmeyree, S. Fan, J. D. Joannopoulos, L. C. Kimerling, H. I. Smith, and E. P. Ippen. Photonic-bandgap microcavities in optical waveguides. *Nature*, 390:143–145, 1997.

[21] S. Foteinopoulou and C. M. Soukoulis. Theoretical investigation of one-dimensional cavities in two-dimensional photonic crystals. *IEEE Journal of Quantum Electronics*, 38(7):844–849, July 2002.

[22] C. Goldsmith, T. H. Lin, W. R. W. B. Powers, and B. Norvell. Micromechanical membrane switches for microwave applications. In *IEEE MTT-S Int.Microw. Symp. Proc.*, pages 91–94, Orlando, FL, May 1995.

[23] T. D. Happ, M. Kamp, A. Forchel, A. V. Bazhenov, I. I. Tartakovskii, A. Gorbunov, and V. D. Kulakovskii. Coupling of point-defect microcavities in two-dimensional photonic-crystal slabs. *J. Opt. Soc. Amer. B*, 20(2):373–378, February 2003.

[24] F. Harfoush, A. Taflove, and G. A. Kriegsmann. A numerical technique for analyzing electromagnetic wave scattering from moving surfaces in one and two dimensions. *IEEE Transactions on Antennas and Propagation*, 37(1):55–63, January 1989.

[25] J. Hecht. Slow light and fast data links. *Optics and Photonics News*, 17(6):22–27, June 2006.

[26] K. Hennessy, A. Badolato, A. Tamboli, P. M. Petroff, E. Hu, M. Atature, J. Dreiser, and A. Imamoglu. Tuning photonic crystal nanocavity modes by wet chemical digital etching. *Applied Physics Letters*, 87(2), 2005.

[27] M. Imada, S. Noda, A. Chutinan, M. Mochizuki, and T. Tanaka. Channel drop filter using a single defect in a 2-D photonic crystal slab waveguide. *Journal of Lightwave Technology*, 20(5):873–878, May 2002.

[28] M. J. Inman and C. E. S. A. Z. Elsherbeni. Modeling and optimization of RF reconfigurable tuners with computationally efficient time-domain techniques. In *Radar Conference, 2003. Proceedings of the 2003 IEEE*, pages 439–445, MS, USA, May 2003.

[29] S. Iwamoto and Y. Arakawa. Photonic crystal with advanced micro/nano-structures: Quantum dots and MEMS. *IEICE TRANS. ELECTRON*, E87-C(3):343, March 2004.

[30] S. G. Johnson and J. D. Joannopoulos. Block-iterative frequency-domain methods for Maxwell's equations in a planewave basis. *Opt. Express*, 8(3):173–190, 2001.

[31] Y. Kanamori, K. Inoue, K. Horie, and K. Hane. Photonic crystal switch by inserting nano-crystal defects using MEMS actuator. *Optical MEMS, 2003 IEEE/LEOS International Conference on*, pages 107–108, August 2003.

[32] B. M. King and K. D. Akdemir. Doppler induced nonlinear photonic crystal NEMs/MEMs. In *OSA Annual Meeting*, Tucson, Arizona, October 2005.

[33] K. Li, M. A. Tassoudji, R. T. Shin, and J. A. Kong. Simulation of electromagnetic radiation and scattering using a finite difference-time domain technique. *Computer Applications in Engineering Education*, 1(1):45–62, 1992.

[34] K. Y. Lim, D. J. Ripin, G. S. Petrich, L. A. Kolodziejski, E. P. Ippen, M. Mondol, H. I. Smith, P. R. Villeneuve, S. Fan, and J. D. Joannopoulos. Photonic band-gap waveguide microcavities: Monorails and air bridges. *J. Vac. Sci. Technol. B*, 17:1171–1174, 1999.

[35] A. Mekis, J. C. Chen, I. Kurland, S. Fan, P. R. Villeneuve, and J. D. Joannopoulos. High transmission through sharp bends in photonic crystal waveguides. *Phys. Rev. Lett. 77*, pages 3787–3790, October 1996.

[36] S. Mingaleev and Y. Kivshar. Effective equations for photonic crystal waveguides and circuits. *Opt. Lett. 27*, page 231, 2002.

[37] S. Mingaleev and Y. Kivshar. Nonlinear photonic crystals toward all-optical technologies. *Opt. and Phot. News*, 13(48), 2002.

[38] S. Mingaleev, Y. Kivshar, and R. A. Sammut. Long-range interaction and nonlinear localized modes in photonic crystal waveguides. *Phys. Rev. E*, 62:5777–5782, 2000.

[39] C. Monat, C. Seassal, and X. Letartre. Photonic crystal microlasers in InP on silicon. *J. Phys. IV*, 12:267–268, June 2002.

[40] G. Moore. Cramming more components onto integrated circuits. *Electronics*, 38(8):114–117, 1965.

[41] M. A. Morgan. *Electromagnetics Research 2: Finite-Element and Finite-Difference Methods in Electromagnetic Scattering*, chapter 8. NewYork:Elsevier, 1990.

[42] G. Mur. Absorbing boundary conditions for the finite-difference approximation of the time-domain electromagnetic field equations. *Electromagnetic Compatibility, IEEE Transactions*, 23:377–382, 1981.

[43] A. Neukermans and R. Ramaswami. MEMS technology for optical networking applications. *Communications Magazine, IEEE*, 39(1):62–69, Jan 2001.

[44] M. Notomi, A. Shinya, K. Yamada, J.-I. Takahashi, C. Takahashi, and I. Yokohama. Structural tuning of guiding modes of line-defect waveguides of silicon-on-insulator photonic crystal slabs. *IEEE Journal of Quantum Electronics*, 38(7):736–742, July 2002.

[45] S. J. Orfanidis. *Electromagnetic Waves and Antennas*. June 2004.

[46] L. Pang, W. Nakagawa, and Y. Fainman. Fabrication of two-dimensional photonic crystals with controlled defects by use of multiple exposures and direct write. *APPLIED OPTICS*, 42(27):5450–5456, September 2003.

[47] W. Pauli. *Theory of Relativity.* Elmsford, NY: Pergamon, 1958.

[48] M. Qiu, B. Jaskorzynska, M. Swillo, and H. Benisty. Time-domain 2D modeling of slab-waveguide based photonic-crystal devices in the presence of radiation losses. *Microwave Opt. Tech. Lett.*, 34(5):387–393, September 2002.

[49] S. Rajic, J. Corbeil, and P. Datskos. Feasibility of tunable MEMS photonic crystal devices. *Ultramicroscopy*, 97(1-4):473–479, Oct-Nov 2003.

[50] M. Rakhmanov. Doppler-induced dynamics of fields in fabry-perot cavities with suspended mirrors. *Applied Optics*, 40(12):1942–1949, 2001.

[51] E. J. Reed, M. Soljacic, and J. D. Joannopoulos. Color of shockwaves in photonic crystals. *Phys. Rev. Lett.*, 90(20):203904–1 – 203904–4, May 2003.

[52] E. J. Reed, M. Soljacic, and J. D. Joannopoulos. Reversed doppler effect in photonic crystals. *Phys. Rev. Lett.*, 91(13):133901–1 – 133901–4, September 2003.

[53] J. Rizk, G. Tan, J. Muldavin, and G. M. Rebeiz. High isolation w-band MEMS switches. *IEEE Microw. Wirel. Compon. Lett.*, 11(1):10–12, 2001.

[54] M. S. Rogers, J. J. Sniegowski, S. L. Miller, and G. F. LaVigne. Designing and operating electrostatically driven microengines. In *Proceedings of the 44th International Instrumentation Symposium*, pages 56–65, Reno, NV, May 1998.

[55] M. Ruan, G. Tam, R. Vaitkus, C. Wheeler, and J. Shen. Micro magnetic latching RF switches. In *Proc. Wireless Design Conf.*, pages 59–66, London, May 2002.

[56] M. Sarandy, L. Wu, and D. Lidar. Consistency of the adiabatic theorem. *Quantum Information Processing*, 3:331, 2004.

[57] A. Scherer. Photonic crystals for confining, guiding, and emitting light. *IEEE Transactions on Nanotechnology*, 1(1):4–11, March 2002.

[58] J. Schneider and C. Wagner. Fdtd dispersion revisited: Faster-than-light propagation, 1998.

[59] C. T. Schröder and W. R. Scott, Jr. Three-dimensional FDTD model to study the elastic-wave interaction with buried land mines. In *IGARSS 2000. Int. Geoscience and Remote Sensing Symp.*, volume 1, pages 26–28, Honolulu, HI, July 2000.

[60] C. T. Schröder and W. R. Scott, Jr. Elastic waves interacting with buried land mines: A study using the FDTD method. *IEEE Transactions on Geoscience and Remote Sensing*, 40(6):1405–1415, June 2002.

[61] S.J.B.Yoo. Wavelength conversion technologies for wdm network applications. *Journal of Lightwave Technology*, 14(6):955–966, June 1996.

[62] J. J. Sniegowski and E. J. Garcia. Microfabricated actuators and their application to optics. In *Proc. SPIE Miniaturized Systems with Micro-Optics and Micromechanics*, pages 46–64, San Jose, CA, July-September 1995.

[63] A. Taflove. Review of the formulation and applications of the finite-difference time-domain method for numerical modeling of electromagnetic wave interactions with arbitrary structures. *Wave Motion*, 10:547–582, 1988.

[64] A. Taflove and M. E. Brodwin. Numerical solution of steady-state electromagnetic scattering problems using the time-dependent Maxwell's equations. *Microwave Theory and Techniques, IEEE Transactions on*, 23(8):623–630, 1975.

[65] A. Taflove and S. C. Hagnes. *Computational Electrodynamics: The Finite-Difference Time-Domain Method*. Artech House, Inc., 2 edition, April 2000.

[66] D. M. Tanner, J. A. Walraven, S. M. Barnes, N. F. Smith, F. Bitsie, and S. E. Swanson. Reliability of a MEMS torsional ratcheting actuator. In *Proceedings of IRPS*, pages 81–90, 2001.

[67] M. Tokushima and H. Yamada. Light propagation in a photonic-crystal-slab line-defect waveguide. *IEEE J. Quantum Electron*, 38(7):753–759, July 2002.

[68] D. Vakhshoori. 2 mW CW single-mode operation of a tunable 1550 nm vertical cavity surface emitting laser with 50 nm tuning range. *Elect. Lett.*, 35(11):1–2, May 1999.

[69] J. Walker. Fabrication of a mechanical antireflection switch for fiber-to-the-home systems. *IEEE J. Micro. Mech. Sys.*, 5(1):45–51, 1996.

[70] Wikipedia. Doppler effect — wikipedia, the free encyclopedia, 2006. [Online; accessed 1-December-2006].

[71] Wikipedia. Finite-difference time-domain method — wikipedia, the free encyclopedia, 2006. [Online; accessed 21-November-2006].

[72] R. Wood. A MEMS variable optical attenuator. In *Proc IEEE/LEOS Int'l. Conf. Opt. MEMS*, pages 121–22, Kauai, HI, August 2000.

[73] M. C. Wu, P. R. Patterson, D. Hah, M. C. Lee, S. Huang, and J.-C. Tsai. Advanced mems for photonics. In *Device Research Conference*, pages 13–16, 2002.

[74] E. Yablonovitch. Inhibited spontaneous emission in solid-state physics and electronics. *Phys. Rev. Lett.*, 58:1950, 1987.

[75] K. S. Yee. Numerical solution of initial boundary value problems involving Maxwell's equations in isotropic media. *IEEE Transactions on Antennas and Propagation*, 14(3):302–307, March 1966.

[76] J. P. Zhang. Nanofabrication of 1-D photonic bandgap structures along a photonic wire. *IEEE Photonics Technology Letters*, 8(4):491–493, April 1996.